SANDIA REPORT

SAND97-2182 • UC-722
Unlimited Release
Printed September 1997

Calculation of Shipboard Fire Conditions for Radioactive Materials Packages with the Methods of Computational Fluid Dynamics

J. A. Koski, S. D. Wix, J. K. Cole

Prepared by
Sandia National Laboratories
Albuquerque, New Mexico 87185 and Livermore, California 94550

Sandia is a multiprogram laboratory operated by Sandia Corporation, a Lockheed Martin Company, for the United States Department of Energy under Contract DE-AC04-94AL85000.

Sandia National Laboratories

Issued by Sandia National Laboratories, operated for the United States Department of Energy by Sandia Corporation.

Available to DOE and DOE contractors from
Office of Scientific and Technical Information
P.O. Box 62
Oak Ridge, TN 37831

Prices available from (615) 576-8401, FTS 626-8401

Available to the public from
National Technical Information Service
U.S. Department of Commerce
5285 Port Royal Rd
Springfield, VA 22161

NTIS price codes
Printed copy: A04
Microfiche copy: A01

Distribution
Category UC-722

SAND97-2182
Unlimited Release
Printed September 1997

Calculation of Shipboard Fire Conditions for Radioactive Materials Packages with the Methods of Computational Fluid Dynamics

J. A. Koski and S.D. Wix
Transportation Systems Department

J. K. Cole
Aerosciences and Compressible Fluid Mechanics Department
Sandia National Laboratories
P.O. Box 5800
Albuquerque, NM 87185-0717

ABSTRACT

Shipboard fires both in the same ship hold and in an adjacent hold aboard a break-bulk cargo ship are simulated with a commercial finite-volume computational fluid mechanics code. The fire models and modeling techniques are described and discussed. Temperatures and heat fluxes to a simulated materials package are calculated and compared to experimental values. The overall accuracy of the calculations is assessed.

Table of Contents

List of Figures

List of Tables

1.0 INTRODUCTION

Concerns have been raised [1] about the safety of radioactive material shipments exposed to shipboard fires. To improve the knowledge of the shipboard fire environment, a series of tests with simulated radioactive materials packages was conducted aboard an actual freighter and the results reported [2]. If computer models of these tests can be developed and proven to be accurate, then the computation methods developed can be applied with confidence to other shipboard fire geometries, sizes and durations. The computer models described in this report include all thermal transport mechanisms, and the report provides information on the success and accuracy of the models developed in predicting the experimental results from the shipboard fires.

To assure that others interested in the problem can also apply the results of this report, a commercially available computational fluid dynamics computer code, CFX, marketed by AEA Technologies has been used for the calculations. This code was selected because of its previous use in fire analyses, and its ability to treat all heat transfer mechanisms, i.e., conduction, convection and thermal radiation, in a coupled manner. In addition, an effort has been made to limit the input of experimental results into the analysis model so that analysts without access to detailed experimental data can confidently create similar models.

1.1 Problem Statement

The purpose of this report is to document successful techniques for simulating some experimental shipboard fires. The experimental fires were staged in Holds 4 and 5 of the *Mayo Lykes*, a 10700 deadweight ton World War II Liberty Class break-bulk freighter, operated for fire testing purposes by the Coast Guard Fire and Safety Test Detachment at Little Sand Island in Mobile Bay, Alabama. A general schematic of the fire arrangement is shown in Figure 1. Figure 2 shows the general location of the holds aboard the *Lykes*. The results from three tests in the experimental series were selected for analysis: Tests 5037, 5040, and 5045 (see Reference [2] for more complete details of the experiments). Tests 5037 and 5045 were two-burner and four-burner heptane spray tests with the ignited sprays impinging on the Hold 4-5 bulkhead. These tests were intended to simulate an engine-room or galley fire in an adjacent compartment. These fires were located in Hold 4, the major purpose of these tests was to determine the effect the fires had on simulated haz-

ardous cargo in Hold 5. Test 5040, a wood crib fire in Hold 4, was intended to simulate burning cargo in the same hold as the hazardous cargo. For this test, emphasis was on simulating the conditions in Hold 4. Test 5043, a duplicate of wood-crib-fire Test 5040, could also be used for comparison to the computer simulations.

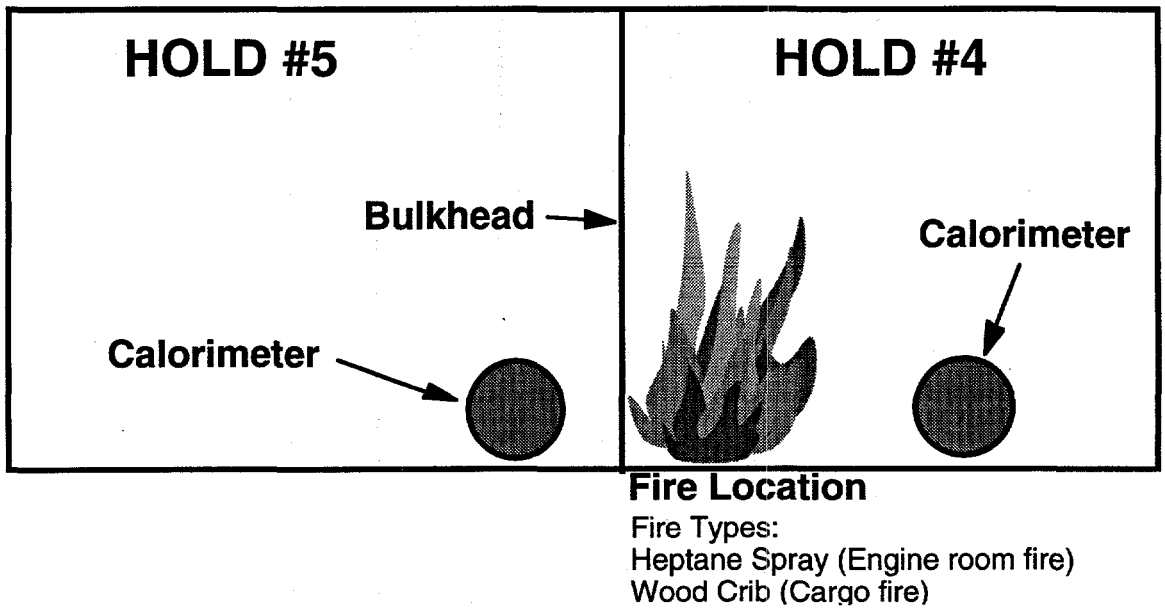

Figure 1. Schematic of the Fire test arrangement.

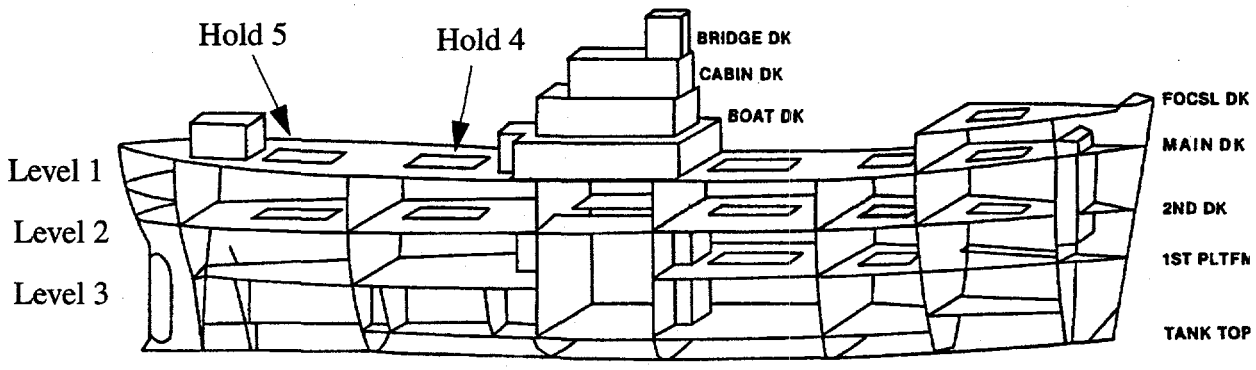

Figure 2. Hold arrangement of the Mayo Lykes.

1.2 Description of Problem Geometry

The general layouts of Level 1 of Holds 4 and 5 are shown in Figures 3 and 4. These holds are located just below the weather deck of the ship. Main features in Hold 4 are the Engine Room mock-up which is a sheet metal structure used for fire-suppression testing, and the King post cen-

tered in the Hold 4-5 bulkhead. The King post, a large circular steel structure, supports a cargo crane located on the weather deck of the *Mayo Lykes*. Hold 5 contains a large furnace intended for other fire experiments aboard the *Lykes*. Height of the holds varied, but was close to 3.7 m. Ventilator ducts in Holds 4 and 5 (see Figures 3 and 4) were removed before the fire experiments to simplify the problem geometry and remove obstacles to heat transfer between the holds.

Ventilation was provided to Hold 4 to prevent accumulation of explosive gas mixtures in the holds. For the heptane-spray fires, the port and starboard openings in the hull were open, as were the openings at the forward end of the engine-room mock-up (see Figure 3). Two 2 m x 3 m roofing panel openings vent gases from the engine-room mock-up overhead. For the wood crib fires, the openings at the forward end of the engine-room mock-up were closed. For all tests, openings in Hold 5 were closed to simulate at-sea conditions for cargo.

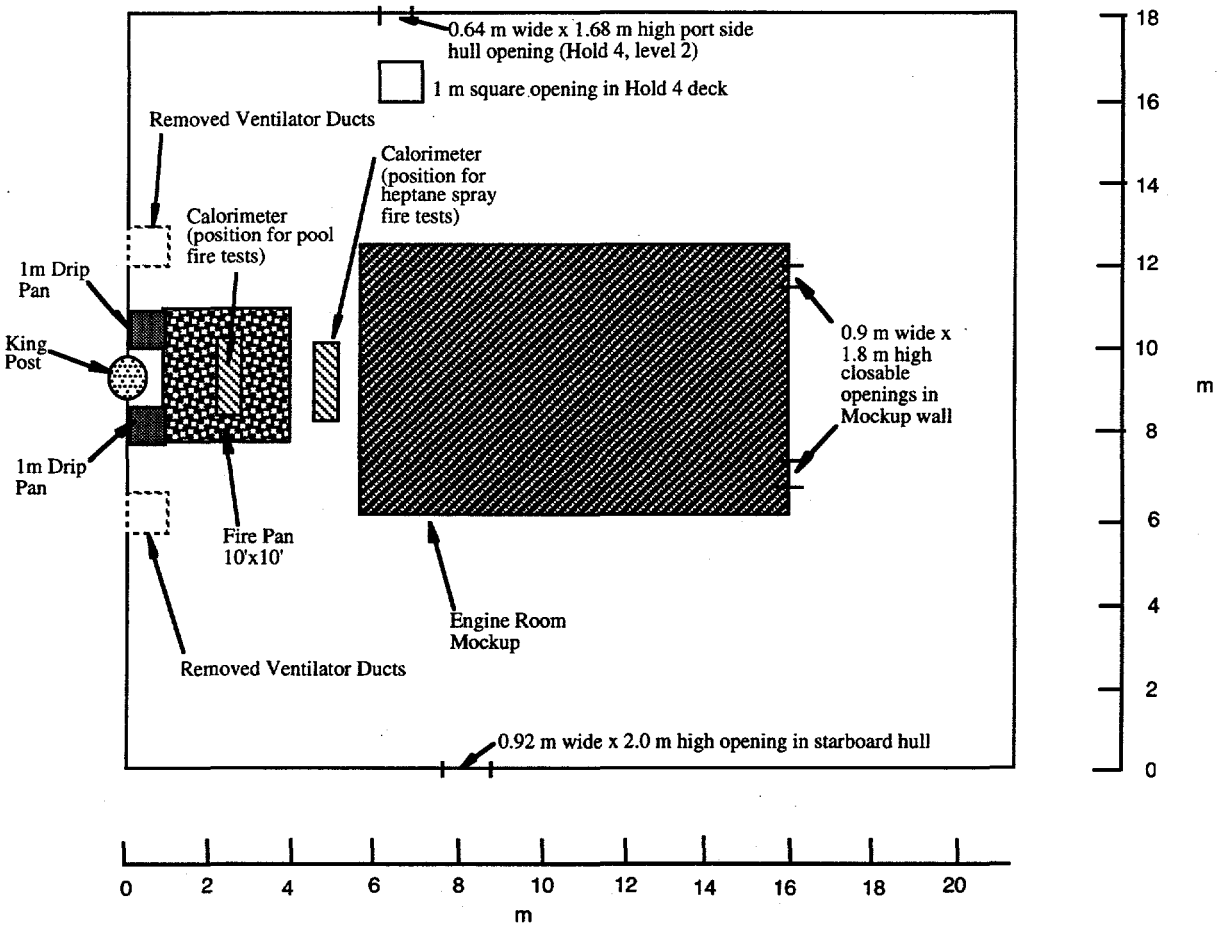

Figure 3. Hold 4 arrangement.

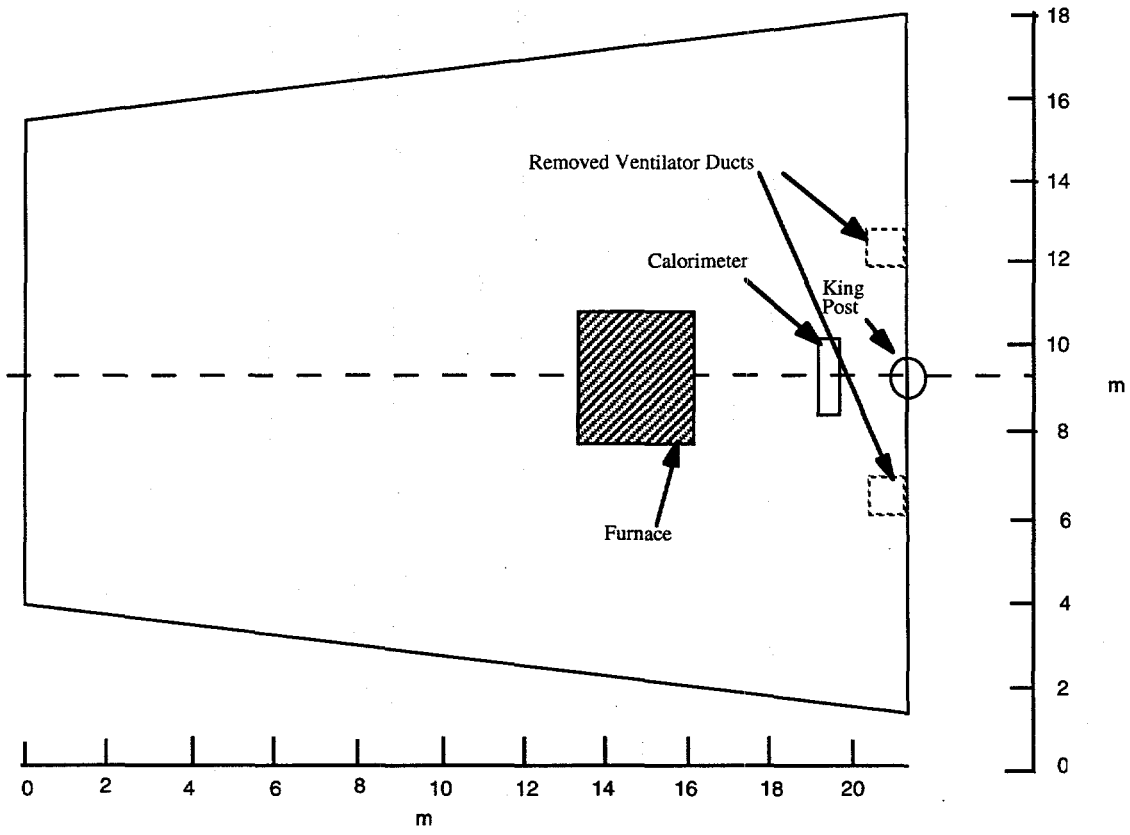

Figure 4. Hold 5 arrangement.

1.3 Description of the Computational Fluid Dynamics Code and Basic Assumptions

The CFX computer code [3], formerly known as CFDS-FLOW3D, chosen for these simulations is a finite volume, multi-block computational fluid dynamics code that can solve coupled energy and fluid transport problems. Conduction and radiation are treated simultaneously with flow solutions. Cartesian or cylindrical coordinates may be used to construct full three-dimensional models of solids and fluid-filled volumes. For the fire simulations, a standard k-ε flow turbulence model [3] was used, with the SIMPLE [4] algorithm applied for numerical solutions.

Thermal radiation solutions in CFX were achieved via a Shah model [3]. No attempt was made to model the chemical reactions in the combustion processes of the heptane sprays or wood cribs. Instead, total fire energy outputs estimated in [2] were used in surface and volumetric models of the bulkhead and wood cribs as described in further detail in later sections. In addition, for most cases, air was taken as the working medium with no attempt made to model the gaseous combustion products. Where described, grey-gas participating-medium radiative-heat-transfer models were used to determine the possible effects of smoke in Hold 4.

For numerical convergence, enthalpy of the air was selected as the most important parameter. Implicit time stepping was used for all solutions, and the correctness of the size of the time step was confirmed through checks against results from solutions with smaller time steps.

2.0 DESCRIPTION OF HOLD AND FIRE MODELS

2.1 Hold 4 Model Description

2.1.1 Hold Model

Hold 4 of the Mayo Lykes is located one level below the weather deck, aft of the superstructure, and immediately forward of Hold 5. The arrangement of the hold is symmetrical with respect to the ship's longitudinal axis. During the fire tests, this symmetry was maintained by positioning the centerlines of the fire and the calorimeter on the ship's centerline. No asymmetric thermal or flow processes that violate this symmetry were included in the model.

Figure 5 shows the starboard (right) half of Hold 4 which was modeled in the CFX code. Note that symmetrical flow conditions were also assumed for the CFX calculations for Hold 5 discussed in Section 2.2, but the port (left) side was modeled in that case. This difference is not important so long as information being transferred between these models is reflected properly about the plane of symmetry. Figure 6 is an expanded view of the region of Hold 4 in which the fire was located.

The orthogonal coordinate system used to describe the model has its origin at the lower rear inside corner of the hold where the plane of symmetry intersects the rear bulkhead and the deck. The X-axis is defined as parallel to the ship's longitudinal axis and positive toward the bow. The Y-axis is positive upward and the Z-axis, positive toward the starboard side. Figure 7 shows plan and elevation views of Hold 4 with dimensions in meters. The thicknesses of the bulkheads, deck and overhead are exaggerated to make their dimensions easy to identify.

The bulkheads (walls) were 0.0082 m thick, the deck and overhead, 0.0107 m thick and the hull, 0.0181 m thick. These were all modeled as conducting solids, made of mild steel with the properties:

Density	=	7837 kg/m^3
Specific heat	=	460 J/(kg K)
Conductivity	=	45 W/(m K)

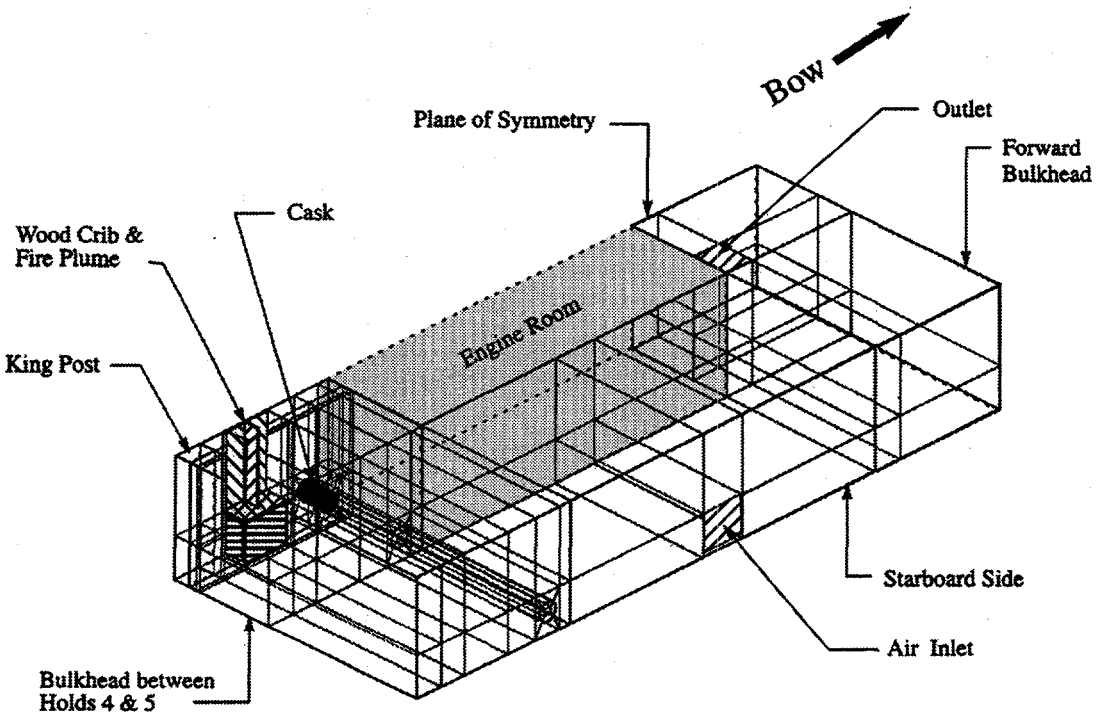

Figure 5. Starboard half of Hold 4 in the *Mayo Lykes*.

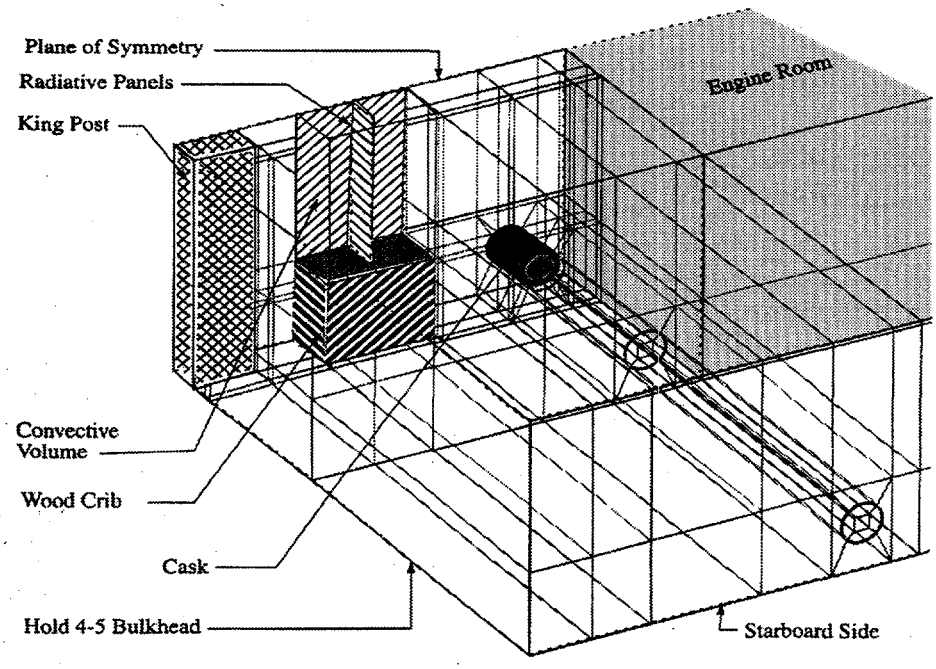

Figure 6. Expanded view of wood crib and calorimeter.

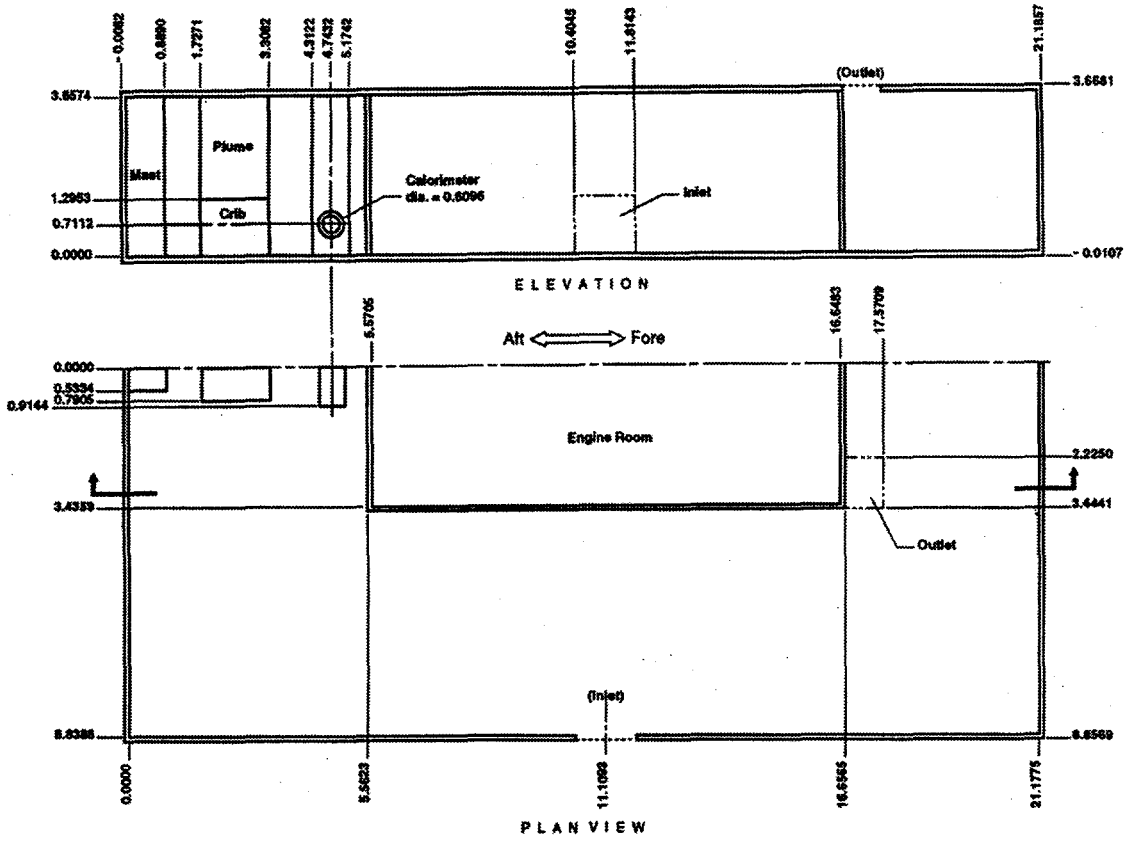

Figure 7. Plan and elevation views of Hold 4 with dimension in meters.

The outer surfaces of all of the bulkheads, deck and overhead that define the boundaries of Hold 4 were subjected to convective and radiative heat transfer assuming a constant atmospheric temperature of 303 K. The radiative emissivity was 0.8 for all of these outer surfaces. The convective heat-transfer coefficients were varied depending upon the orientation of each surface. The values used were:

Vertical surface of bulkhead or hull	=	1.58 W/(m^2 K)
Lower surface of deck	=	1.05 W/(m^2 K)
Upper surface of overhead	=	2.00 W/(m^2 K).

Shear stresses at the inner surfaces of the bulkheads, deck and overhead were left unspecified so that the CFX code could force the fluid velocity to zero at each of these surfaces. The plane of symmetry was also treated as a wall except for the shear stresses being set to zero. This permitted the fluid velocity components parallel to be plane of symmetry to be non-zero.

A King post (mast) is integrated with the bulkhead separating Holds 4 and 5 so that approximately half of it extends into each hold. The portion in Hold 4 was reinforced with large trapezoidal, steel, plates welded to both sides of the King post. The resulting shape approximates a rectangular object more closely than a half cylinder. The actual King post is hollow, but to simplify the CFX model, the King post in the simulation was assumed to be a conducting, rectangular solid. To give

the model King post the same thermal mass and thermal diffusivity as the real one, its thermal properties were modified to be:

Density	=	520 kg/m^3
Specific heat	=	460 J/(kg K)
Conductivity	=	3.06 W/(m K)

2.1.2 Wood Crib Fire Model

The model of the burning wood crib included both radiative and convective parts, see Figure 8. The radiative parts were the lateral and top faces of the wood crib, the plume wall radiator in the plane of symmetry and the plume center radiator that extended from the top of the crib to the overhead. The convective part was the air volume between the top of the wood crib and the overhead. The crib was assumed to maintain its original shape through the entire burn.

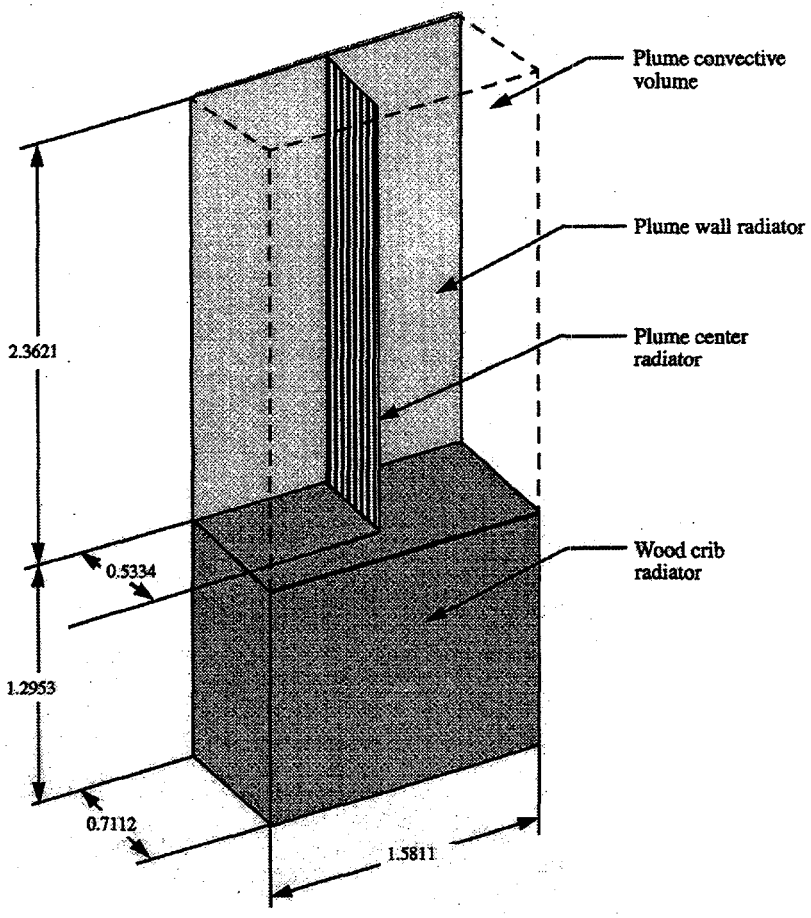

Figure 8. Thermal model for wood crib fire.

The wood crib was constructed of nominal 2 x 4 inch, 0.04 m x 0.09 m, Douglas fir boards, 1.58 m (62.25 inches) long. These were laid in alternating layers with the lengths of the boards in each layer being at right angles to those in the adjacent layers. The wood was assumed to reach a steady burn 30 seconds after ignition and to burn at a constant rate for 1170 seconds. The crib then burned out in 300 seconds. A heptane accelerant was used at the beginning of the wood fire. The accelerant was also assumed to reach a steady burn within 30 seconds, to burn steadily for 270 seconds, and to burn out within 30 seconds. The maximum rate of thermal energy released by the wood and the accelerant was calculated to be 2.37 MW and 1.73 MW, respectively. These whole fire values were halved for the simulation of the starboard half of the hold.

In the first attempt to model the fire, the lateral and upper surfaces of the crib were assumed to remain at a constant temperature of 473 K from ignition until burnout, while the plume radiated most of the energy to the surroundings. Temperatures calculated for the calorimeter using this fire model were much lower than the experimental data.

In the second attempt to model the fire, the crib was assumed to contribute substantially in releasing energy as a radiant heat source. The calculated maximum heat released from the wood crib and the heptane accelerant during the first 300 seconds of the burn was divided about equally between convective and radiant heat transfer. The radiant heat release of the wood crib was then held at this same level until burnout commenced at 1200 seconds. This approach gave better results than the first attempt, and those results are reported here.

The outer surfaces of the wood crib were assigned an emissivity of 0.5 and the plume surfaces, 0.9. To release the radiant heat flux during the period of steady burn, required a maximum fire temperature of 1190 K. At this temperature during the steady burn, the wood crib radiated at 56.9 kW/m^2 and the plume surfaces at 102.3 kW/m^2.

The surfaces of the plume wall radiator and the plume center radiator were assigned zero shear stresses. This permitted air near these surfaces to flow parallel to, but not through, them.

The large transient due to the heptane accelerant was assigned almost entirely to the convective heat release. The convective energy was deposited directly into the air volume between the top of the crib and the overhead. This enhanced the transfer of heat to the air and encouraged the formation of convection. This energy deposition decreased from about 354 to 66 kW/m^3 as the accelerant burned out at 300 seconds. Figure 9 shows the heat flux versus time for the total energy released as well as the energy partitioning between radiation and convection that was used in the model. All of the transients in energy release were modeled with half-cycle cosine functions.

2.1.3 Simulation of Smoke Effects

In the wood crib fire experiments on the *Mayo Lykes*, considerable smoke was generated. To approximate the decreased transparency of the air caused by this smoke, the absorptivity of the air was made a function of air temperature. Geophysical data [5] indicated that clear air had an absorptivity around 6×10^{-5} m^{-1} and light fog, an absorptivity around 6×10^{-3} m^{-1}. If one assumes that the smoke was associated with the hotter air, an S-shaped function can be defined that varies

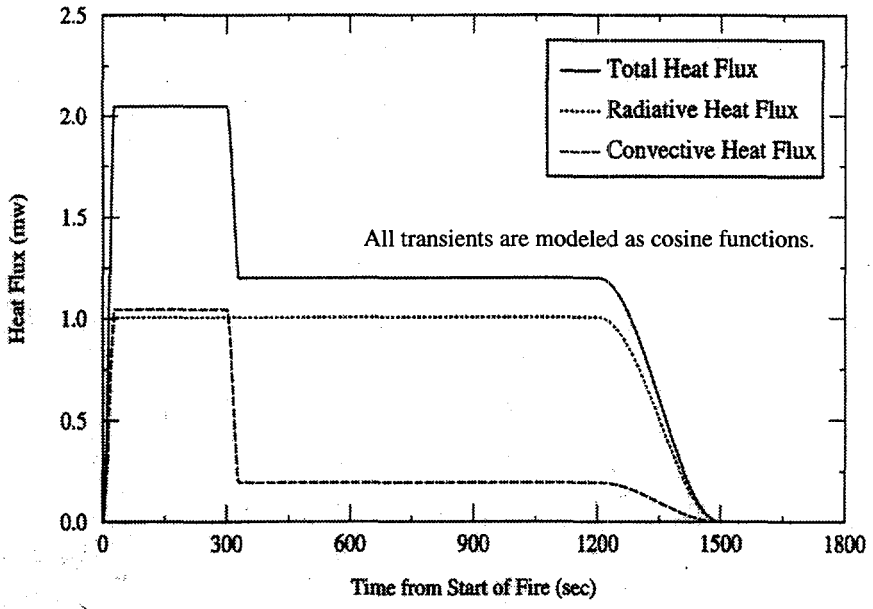

Figure 9. Heat flux temporal model for crib fire.

the air absorptivity between zero absorptivity at 300 K and an absorptivity of 10 m^{-1}at 1200 K in approximate agreement with the geophysical data. This function is shown in Figure 10. At 300 K, the optical depth is essentially infinite and at 1200 K it is decreased to 0.1 m. Fire solutions were calculated with the smoke model and with air that was essentially transparent with an absorptivity of 1 x 10^{-3} m^{-1}.

2.1.4 Calorimeter Model

The experimental calorimeter was made from a steel pipe with a wall thickness of 0.025 m, an outside diameter of 0.61 m and a length of 1.5 m. Its ends were covered by steel disks, 0.025 m thick and its interior was filled with insulation. In the CFX simulation, the right half of this calorimeter was modeled as a steel cylinder of the proper dimensions with an insulated interior. An end cover was not included in the model since it has little influence on the temperatures of the steel cylinder in the side-on orientation to the fire used in the tests.

The calorimeters were instrumented with thermocouples to permit determination of temperatures and heat transfer to the calorimeters. Designs for the calorimeters in Holds 4 and 5 are identical, and most thermocouples were located on the side facing the hot bulkhead between the holds. To analyze the data from the experiments, the SODDIT [6] computer code was used to calculate the heat flux to the surface of the calorimeter based on the temperatures obtained from the thermocouples. Material properties for carbon steel are necessary for estimation of heat fluxes from temperature data. For the analysis, the interior surface of the calorimeter was assumed to be insulated.The calorimeters were filled with insulation to avoid the necessity of performing complicated radiative-heat-transfer calculations of the interior pipe cavity.

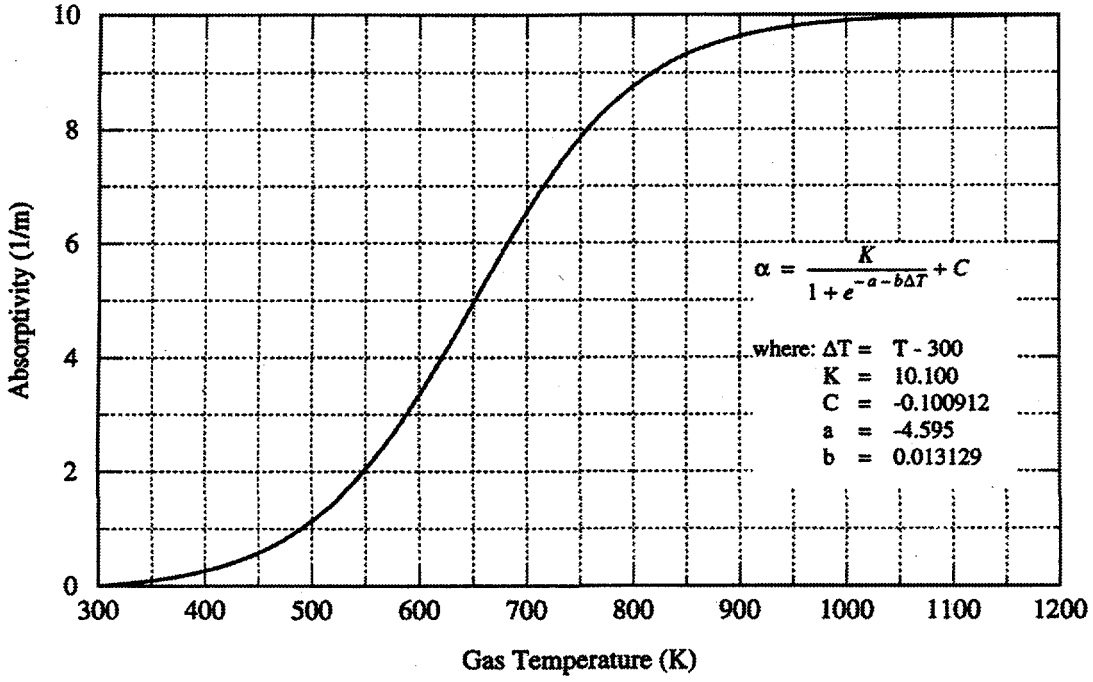

Figure 10. Function used to model absorbing gas.

For consistency in comparison of the analytical results to the experimental heat fluxes, the SOD-DIT code was also used to estimate the heat fluxes to the calorimeter from temperatures calculated with the CFX code.

2.1.5 Modeling of Openings

In the starboard half of Hold 4, a single inlet is located near deck level and a single outlet is located near the top of the forward bulkhead of the engine room. The lower edge of the inlet penetrates the hull about 0.5 m below the deck and several steps are required to reach deck level. The indentation in the deck created by the enclosed stairwell was not explicitly modeled. Instead, an opening the upper edge of which was located at the same height above the deck as that of the actual entrance was modeled. To provide the same flow area as the actual inlet, the model inlet was made wider. In the model, this inlet was centered longitudinally in the hold.

The outlet was modeled with the same area and proportions as the actual outlet, but was placed in the overhead rather than at the top of the bulkhead. Figures 5 and 7 show the locations of the inlet and outlet. Initial CFX calculations assumed both inlet and outlet were open to flow and were characterized as constant-pressure boundaries. This resulted in cool outside air coming into the hold through the inlet and the heated air exiting through the outlet.

For the heptane fire tests, the inlet and outlet were open to prevent a build up of explosive gas. However, the outlet in the overhead was closed for the wood-crib fire tests. Flow solutions were

calculated for a wood-crib fire with the outlet open as well as closed. When the outlet was closed, air flowed into the hold through the lower part of the inlet and out through the upper part.

2.1.6 Radiation Model

The CFX code offers two methods for calculating the radiative heat transfer between surfaces, a Monte Carlo simulation and a discrete transfer method by Shah. The problem considered here has a fixed, rather simple geometry and assumes grey-body radiation. The radiation field was expected to be reasonably homogeneous. Shah's method is the more the two under these conditions and, therefore, was used in this simulation.

Table 1 lists the radiative properties for the various surfaces in the hold. Note that as the roughness parameter for surface increases from 0.0 to 1.0, its spectral reflection decreases linearly from 100 to 0 percent and its diffuse reflection increases linearly from 0 to 100 percent. Albedo indicates the reflectivity of a surface; a value of 0.2 indicates that 20 percent of the incident radiant energy is reflected and the rest absorbed.

TABLE 1. Radiative Properties

Surface	Albedo	Roughness
Bulkheads, Deck & Overhead	0.2	1.0
Plume & Crib	0.1	1.0
Symmetry Surface	0.0	0.0

2.2 Hold 5 Model Description

The computational fluid dynamics (CFD) model of Hold 5, a three-dimensional symmetric model, contains 64,352 cells. Each cell is a volumetric representation of a portion of the model. An axis of symmetry at the ship centerline was used to reduce the overall size of the mode. Conducting solids were used to model features such as the hold bulkheads, deck and overhead, the calorimeter and the king post. The code performs the simultaneous modeling of conduction heat transfer in the conducting solids and heat transfer in the fluid. The model uses the k-ε turbulent flow formulation. Buoyancy was included in the model since any flow will be induced by natural convection. A weakly compressible buoyancy model, which means only density is a function of temperature, was used. Figure 11 presents the overall Hold 5 CFD model and a detail of Hold 5.

A radiation model of Hold 5 was also constructed to run simultaneously with the flow solver. The CFD model and the radiation model are coupled automatically to produce the interaction between convective, conductive and radiative heat transfer. The CFD model transfers either temperatures or heat fluxes to the radiation model, depending on the type of wall boundary condition. The radiation model then solves the radiation problem by tracking photons through a set of zones that form the calculation domain, i.e., the radiation model, and returns either heat fluxes or temperatures to the CFD model. As with Hold 4, the Shah method was chosen for the radiative-heat-transfer calculations. The radiative emissivity of the bulkheads, deck, and overhead was assumed to be

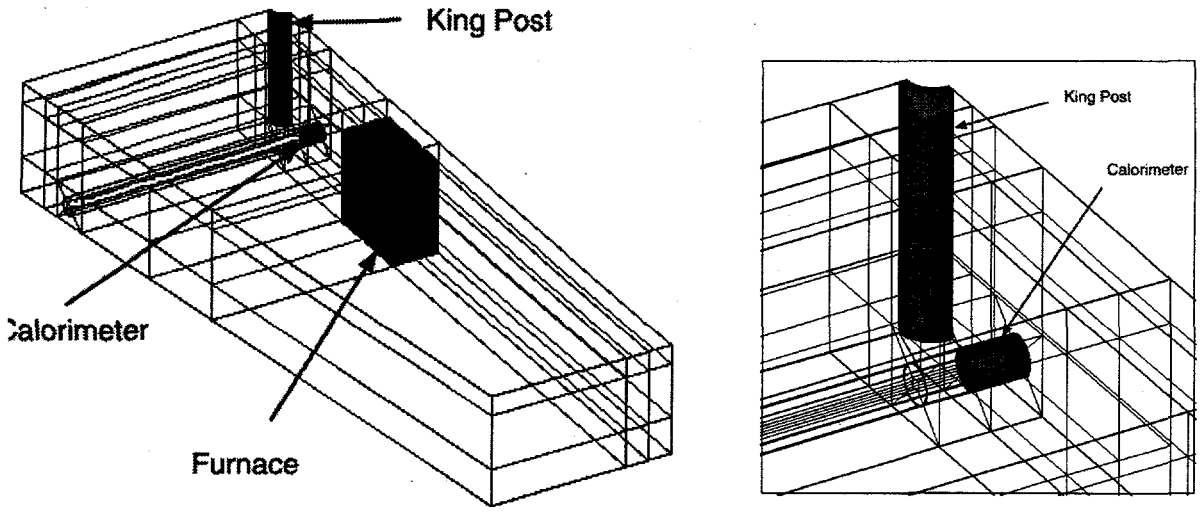

Figure 11. Overall model and detail of Hold 5 model.

0.75 and the radiative emissivity of the calorimeter was 0.8. All surfaces except the axis of symmetry wall, had a surface roughness of 1.0. The surface roughness is the fraction of reflection which is diffuse, the remainder is assumed to be specular. So, all the surfaces in the radiation model, except the axis-of-symmetry wall were diffuse walls. For the axis-of-symmetry wall, the albedo was 1.0 which means that the axis-of-symmetry wall was assumed to be a perfect reflective surface. A grey-body assumption was used in the model and the media within the model was non-participating.

The bulkheads of the Mayo Lykes are 0.008 m thick, the deck and overhead are 0.011 m thick, and the hull is 0.018 m thick. The bulkheads, overhead, deck and hull were modeled using conducting solids in order to include capacitance effects. A King post was present in the hold and was also modeled as a conducting solid. A furnace was also present in Hold 5 when the tests were performed. The furnace was assumed to be a thin sheet of metal covering a low capacitive, low thermal conductivity material such as fire brick. Based on the composition of the furnace, the walls of the furnace were assumed to be adiabatic and were modeled as non-conducting walls.

Consistent with the experimental program, the materials modeled for this analysis are air and mild steel. The thermal properties of air are temperature-dependent. The thermal properties of mild steel were assumed to be constant, with the values of thermal conductivity, density and specific heat taken as 45 W/m-°C, 7849.8 kg/m3, and 460 J/kg-°C, respectively.

2.2.1 Calorimeter Model

A calorimeter of the same shape and size described in Section 2.1.4 was included in the Hold 5 location shown in Figure 11.

2.2.2 Boundary Conditions

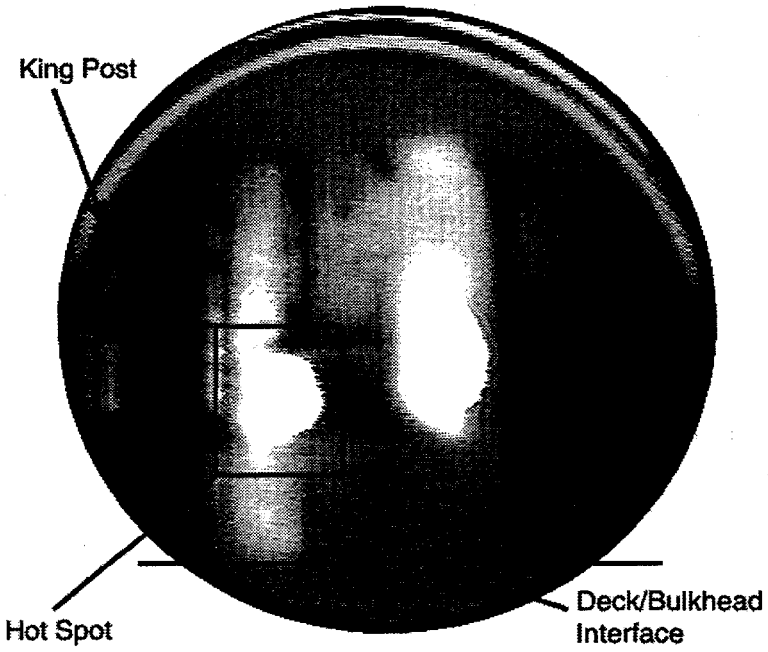

Figure 12. IR image of Hold 5 hot spot.

This analysis is a simulation of an engine-room fire in an adjacent hold. An underlying assumption of this analysis is that the flame of the engine-room fire is in contact with the hold bulkhead and creates a localized hot spot on the bulkhead. The size and shape of the hot spot used in the analysis was taken from the experimental results from the *Lykes* experiments. Infrared images of the bulkhead were taken during the experimental heptane spray tests and the size of the hot spot was scaled from the infrared image shown in Figure 12. The features visible in the IR image are the King post, the hot spot, and the intersection of the hold bulkhead and deck. Since the King post diameter and the deck/bulkhead intersection are known, the approximate size and location of the hot spot on the bulkhead can also be determined. The hot spot was connected via radiation and convection to a boundary condition node set at 900°C, which is in the expected range of flame temperatures. A flame emissivity of 0.9 and a convection coefficient of 10 W/m^2-°C were used.

A symmetry plane was used to model the axis of symmetry in the hold. The symmetry plane had a shear stress of zero to reflect the axis of symmetry in the flow field. With a shear stress of zero at the axis of symmetry, the no-slip wall boundary condition was avoided and the flow was not influenced by the symmetry plane.

Natural-convection boundary conditions were assumed on the exterior of the hold. The convection coefficients depend upon surface orientation. For the bulkheads, the convection coefficient was 4.63 W/m^2. For the deck and overhead, the convective coefficients were 0.775 W/m^2 and 5.67 W/m^2, respectively. The ambient temperature for the two-nozzle calculation was 35°C. For the four-nozzle calculation, the ambient temperature was 15°C. The ambient temperature values were taken from the experimental data.

3.0 RESULTS

3.1 Hold 4 Model Results

3.1.1 Convergence and Sensitivity

For the simulation of the wood crib fire, different size time steps were used for different parts of the burn. Smaller time steps were used when calculating through large transients in the fire's thermal output than during periods of constant thermal output. Table 2 lists the time steps. The calculation of a solution from 0 to 1500 seconds took over 80 hours on an HP755 computer.

TABLE 2. Time steps used.

Time from start of fire (seconds)	Computational time step (seconds)
0 - 60	1.0
60 - 300	5.0
300 - 330	1.0
330 - 1200	5.0
1200 - 1500	1.0

To evaluate the sensitivity of the simulation to the choice of time step, a solution was made with time steps that were half as large as the time intervals shown in Table 2. A comparison of the surface temperatures on the cask at the 90-degree position, which looks directly at the burning wood crib showed essentially no differences in results for the full and half time steps. A comparison of the air temperatures at three heights on a pole located in the hold over 6 m from the fire was also made, and is shown in Figure 13. This location exhibited an increased sensitivity to the time step parameter. At this location, little difference at the lowest position, 0.91 m above the deck was detected, but differences up to 5°C at the highest position, 2.13 m above the desk were calculated. Since the calorimeter results were well converged, and the 5°C difference was well within accept-

able limits for air temperatures, the times steps in Table 3.1.1 were considered sufficiently accurate for the current solution

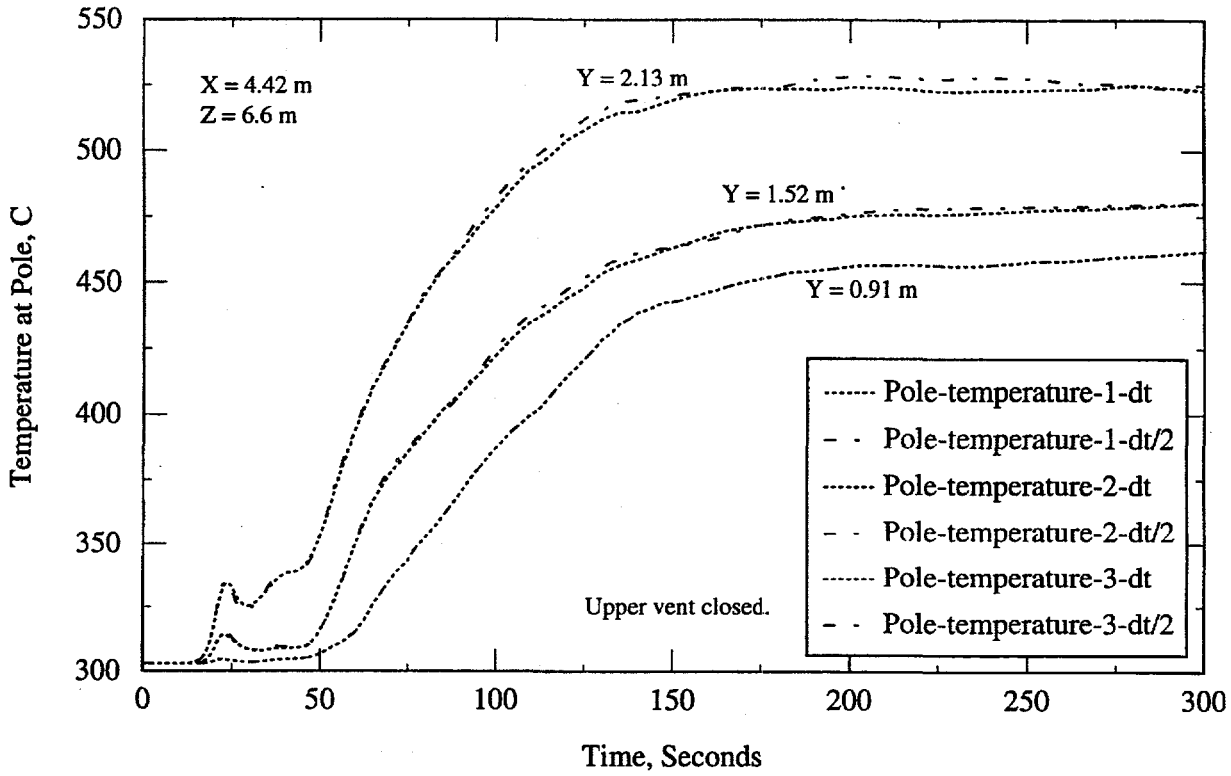

Figure 13. Comparison of air temperatures with two different time steps.

3.1.2 Calorimeter and Hold Temperatures

Figure 14 shows an end view of the calorimeter with the angular locations for the thermocouples and for the calculated temperatures. The 0-degree location is at the very top of the calorimeter, while the 90-degree location is pointed in the negative X-direction which is toward the fire.

Temperatures were calculated for the center of each finite volume, but because of the choice in gridding for the model, the angular locations of the centers were not aligned with the locations of the thermocouples. Thus, the measured values at an angular location must be compared with the nearest calculated values. These angular groupings are listed in Table 2. A complete set of plots comparing the measured and calculated temperatures and heating rates are presented in Appendix A. In this section, only a few are shown and discussed.

Figure 15 is a comparison plot of measured and calculated temperatures at the 90-degree location on the calorimeter (simulated cask). Both calculated transparent (no smoke) and absorbing (smoky) gas results are shown with the measured values. The measured data have been shifted by 390 seconds in each plot to better synchronize the time for actual fire ignition with the calculated value. Note that all of the surface temperatures shown were obtained by processing the measured

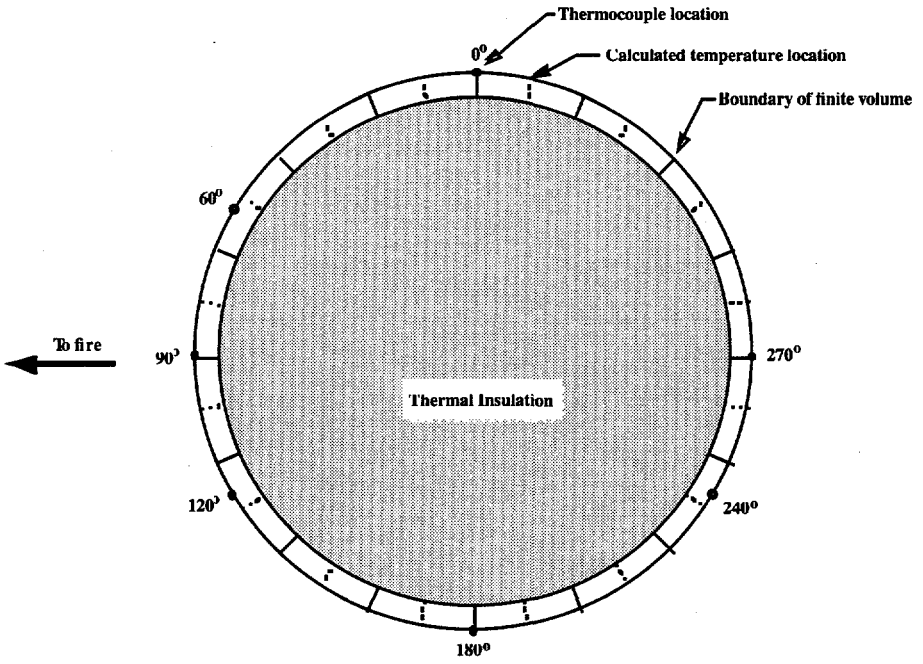

Figure 14. End view of calorimeter and positions of calculated and measured temperatures.

and calculated temperature data through the SODDIT[6] inverse heat transfer code. This procedure produced the most accurate estimates of temperatures at the surface of the calorimeter.

TABLE 3. Angular positions of measured and calculated values.

Location of Measured Values	**Nearest Locations for Calculated Values**	
(degrees)	**(degrees)**	**(degrees)**
0	11.25	348.75
60	56.25	---
90	78.75	101.25
120	123.75	---
180	168.75	191.25
240	236.25	---
270	258.75	281.25

In Figure 15, note that the absorbing-gas calculations result in lower surface temperature predictions than do those for the transparent gas. This is true for the all of the surface temperature comparisons. At the 90-degree location, the calculated temperature increases are greater than the measured increases. At the 60 and 270 degree angular positions, however, the calculated values agree well with the measured values.

The angular distributions of temperature and heat flux around the calorimeter were examined at 9 and 18 minutes after fire ignition. These times were chosen so as to sample near the beginning and toward the end of the fire's duration. Figures 16 and 17 are plots of the surface temperature distri-

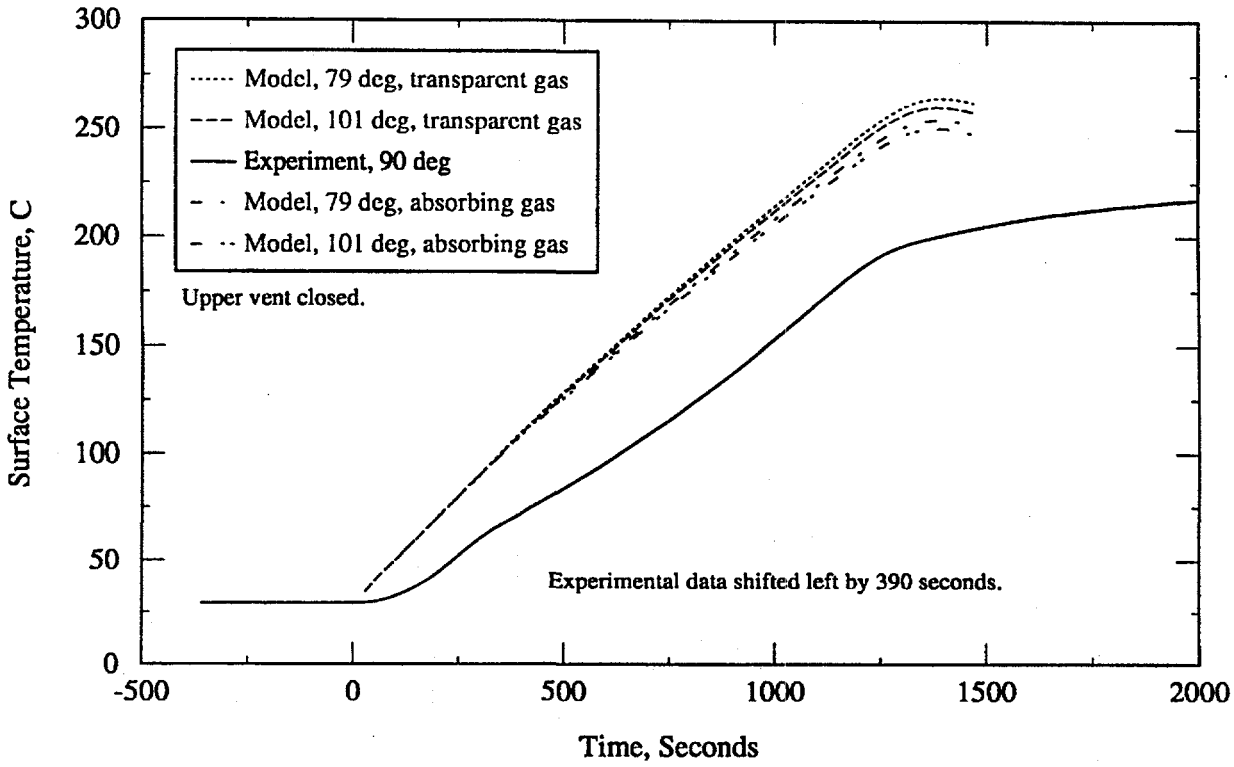

Figure 15. Cask surface temperatures for model and experiment near 90 degrees from top.

bution around the calorimeter at 9 and 18 minutes, respectively. At both times the measured temperatures are significantly less than the calculated temperatures in the region mainly between 90 and 120 degrees from vertical.

Figure 18 compares air temperatures over time at a point about 6 m horizontally from the fire and 2.13 m vertically above the deck. In this case the absorbing-gas solution predicts air temperatures greater than the transparent-gas solution and in better agreement with the measured values. With the hold vents open, the maximum calculated air temperatures at 2.13 m above the deck were about 25°C lower than the closed-vent values shown in Figure 18.

3.1.3 Calorimeter Heat Fluxes

Figure 19 is a comparison plot of the heating rates at 90 degrees, derived from processing the calculated and measured temperature histories through the SODDIT [6] code. On average, the calculated heat fluxes compare reasonably with the measured values for all locations.

The distribution of heat flux around the calorimeter at 9 and 18 minutes are shown in Figure 20 and Figure 21. At 9 minutes, the heat fluxes at 90 and 120 degrees are about 2/3 the measured. However, at 18 minutes, they compare very well with the measured values.

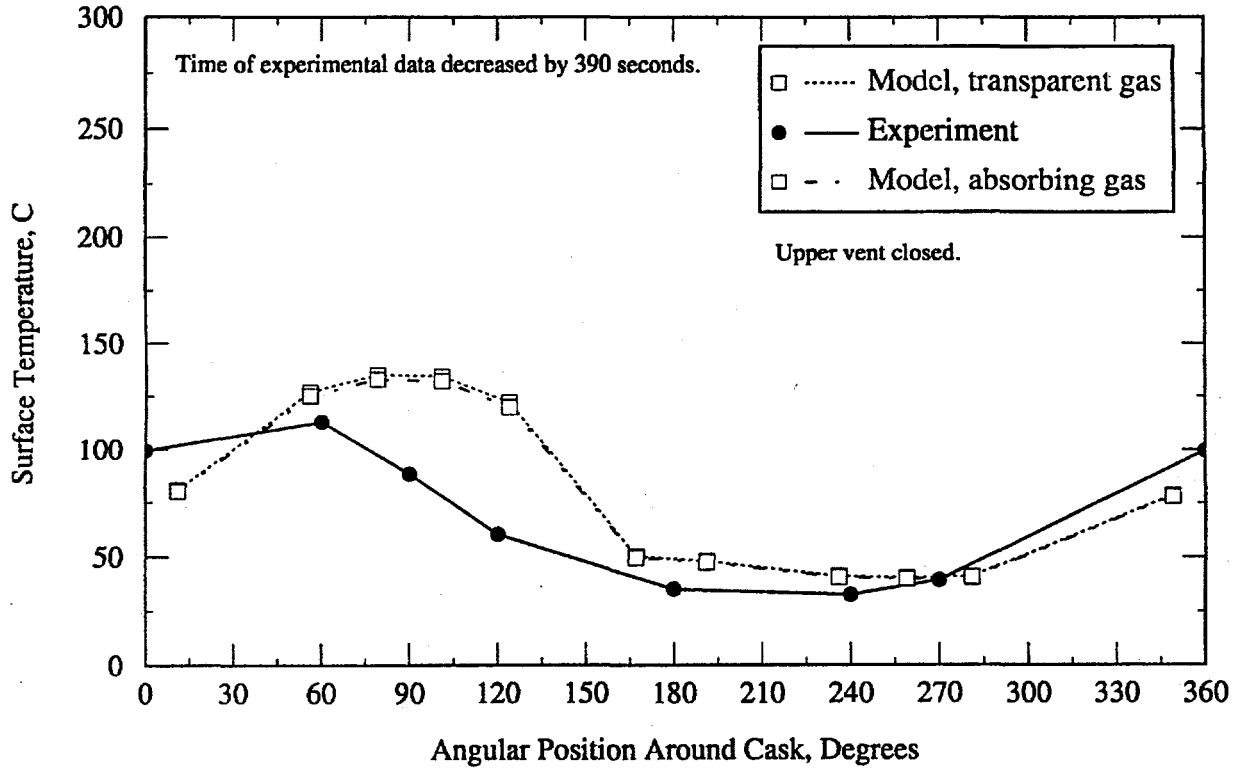

Figure 16. Model and experimental surface temperatures around cask at 9 minutes.

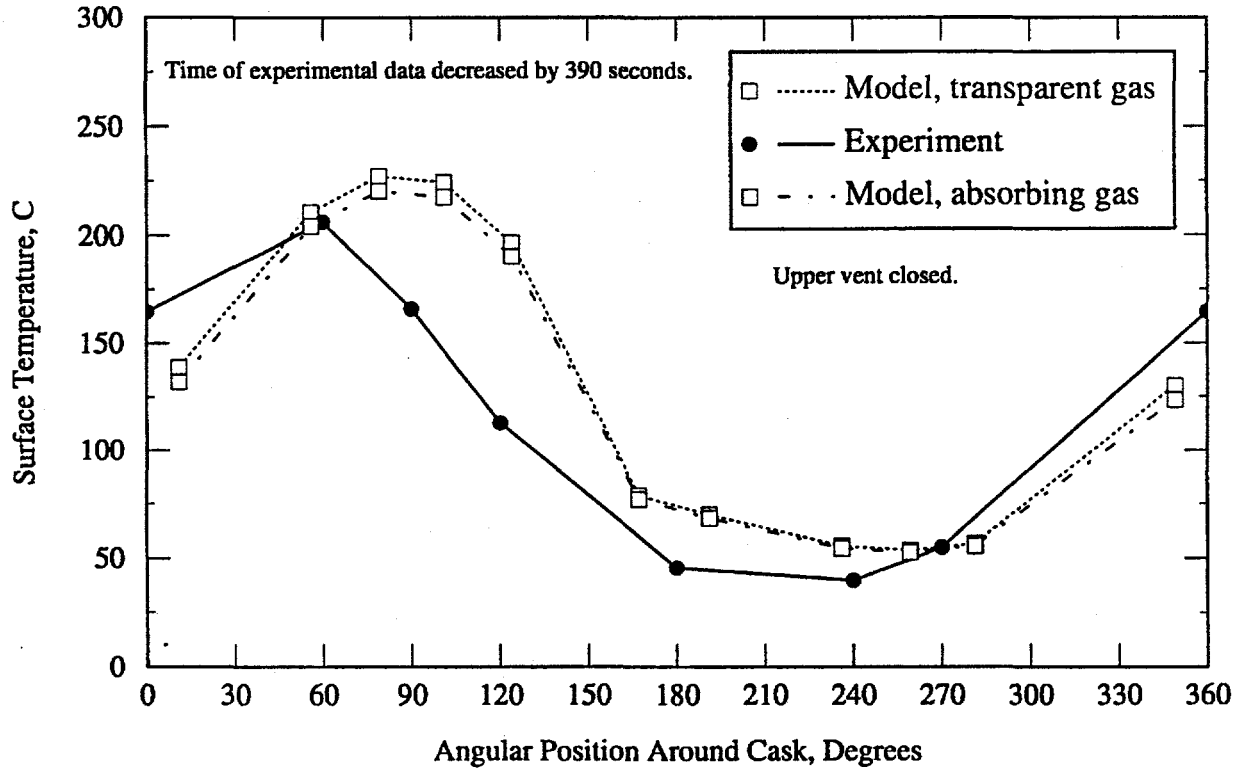

Figure 17. Model and experimental temperatures around cask at 18 minutes.

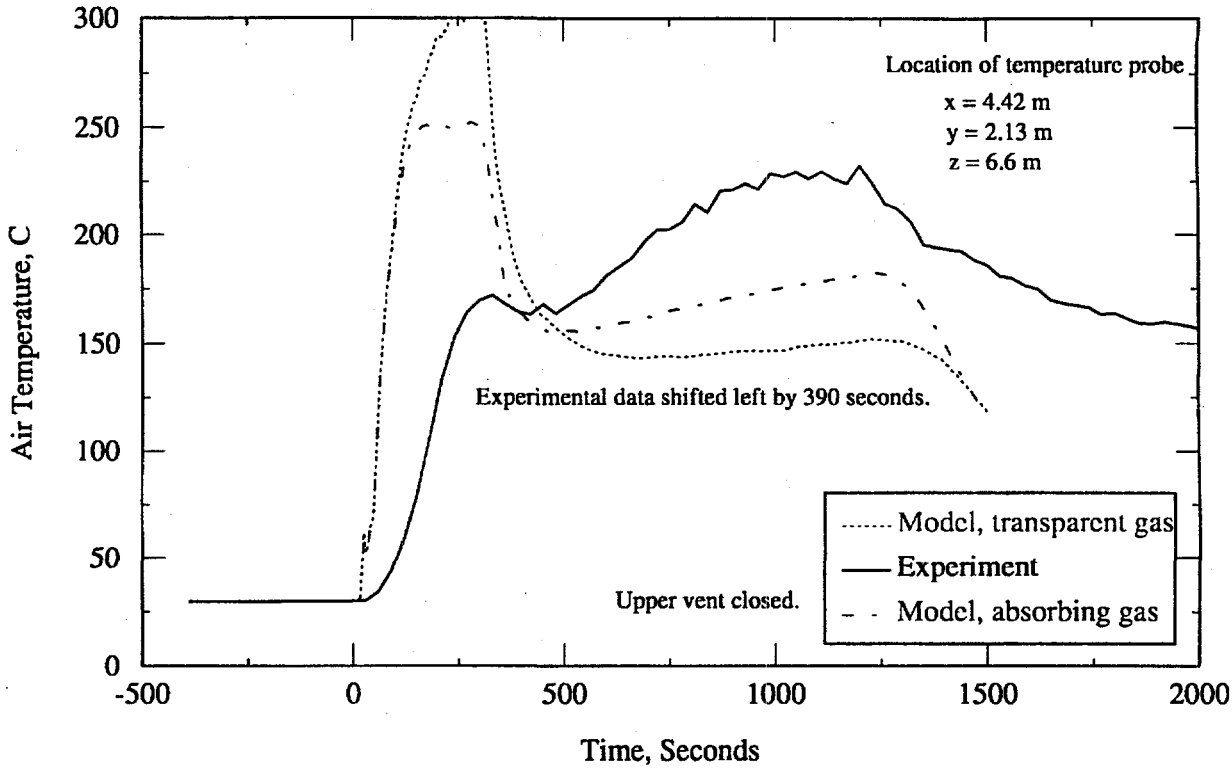

Figure 18. Model and experiment air temperatures at 2.13 m above deck of Hold 4.

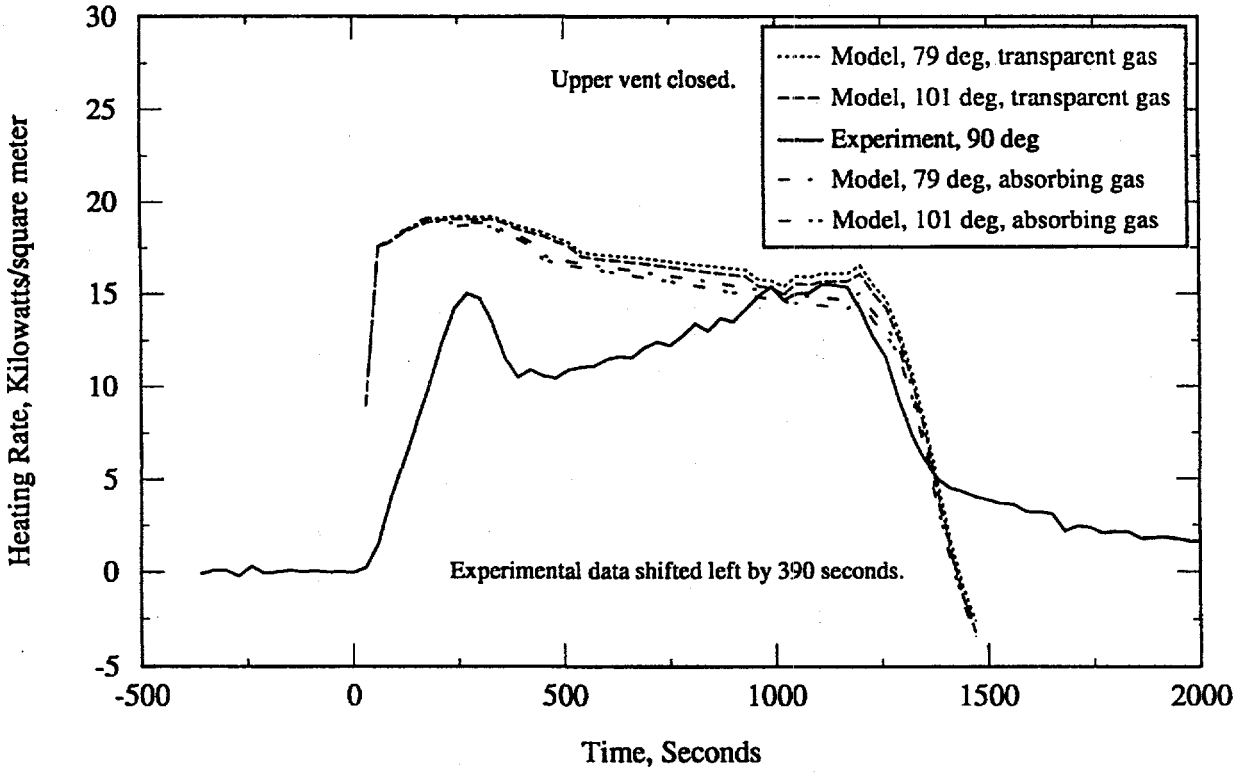

Figure 19. Calorimeter heat flux for model and experiment near 90 degrees.

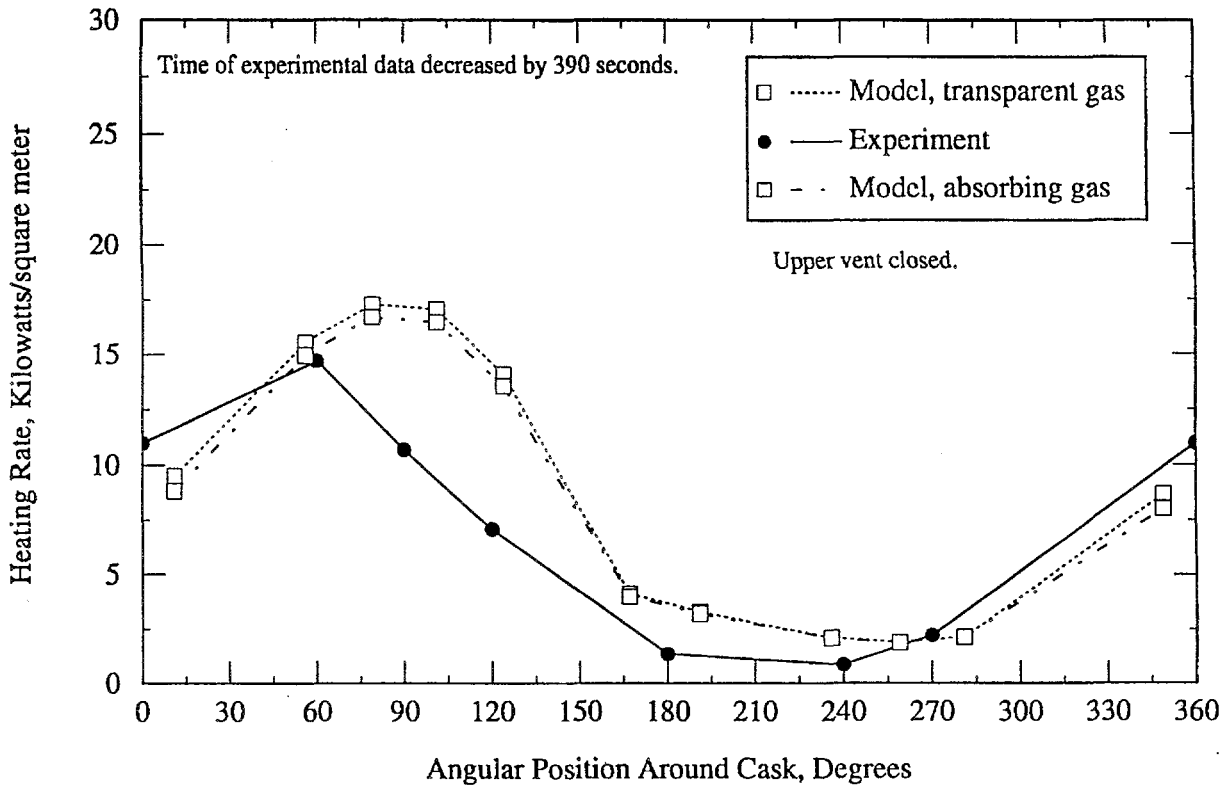

Figure 20. Model and experimental heat fluxes around calorimeter at 9 minutes.

These comparisons of temperature and heat flux have show that usable results can be obtained with rudimentary fire models. To achieve better agreement, more comprehensive fire models must be developed.

3.1.4 Color Fringe Plots

Figures 22, 23, and 24 are color-fringe plots of the ship-hold region near the fire at 300, 1200 and 1500 seconds, respectively. Between 300 and 1200 seconds, the King post (mast) and the bulkheads noticeably heat up. The fire has completely burned out at 1500 seconds, and only parts of the bulkheads and overhead still show some residual heat. The superimposed velocity vectors show the large convective currents generated by the fire.

Unlike the actual experimental calorimeter which had a steel plate at each end of the cylinder, the computer model of the calorimeter assumes insulated ends. Thus, the program calculates results as though the steel rim and the center insulation have a view of hot surroundings. Although this end has no direct view of the fire, thermal radiation reflected and radiated from the other surfaces of the hold cause the outer surface of the insulation to reach a higher temperature than the rim. This artifact can be seen in the color-fringe plots, but does not affect the quality of the temperature data for the circumference of the calorimeter where the comparisons with experimental results are made.

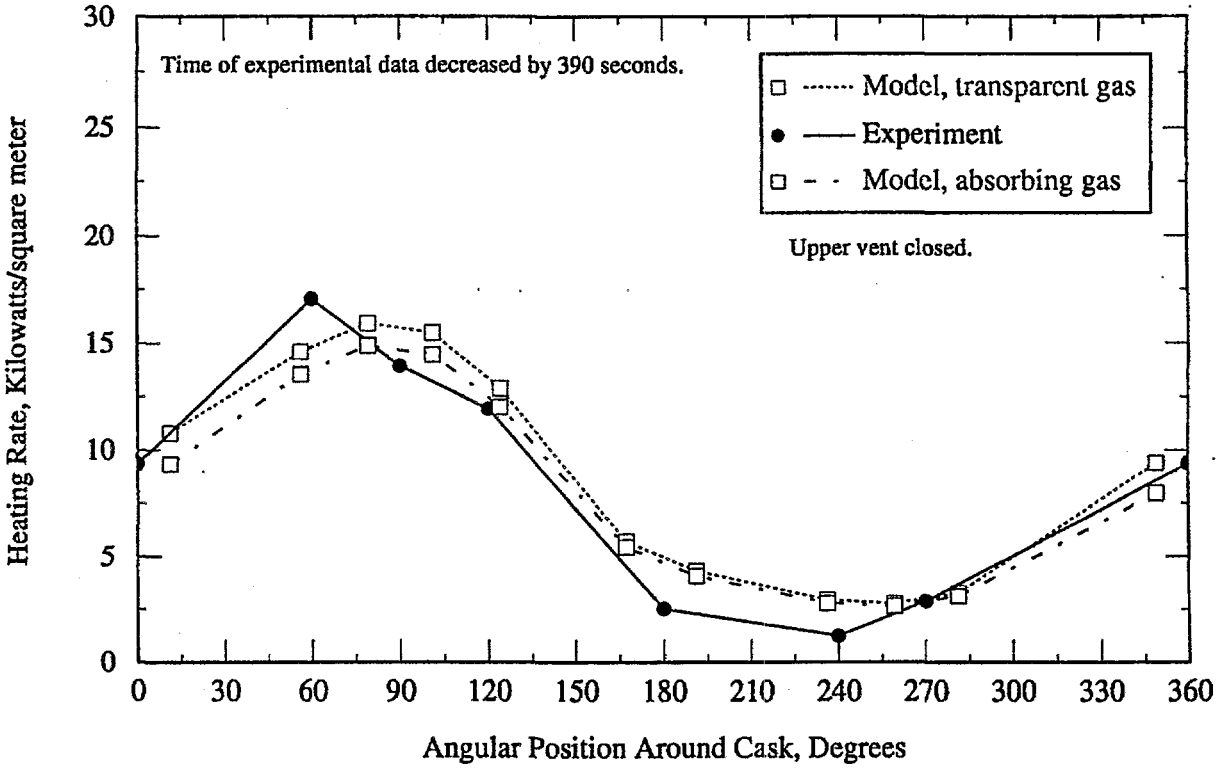

Figure 21. Model and experimental heat fluxes around calorimeter at 18 minutes.

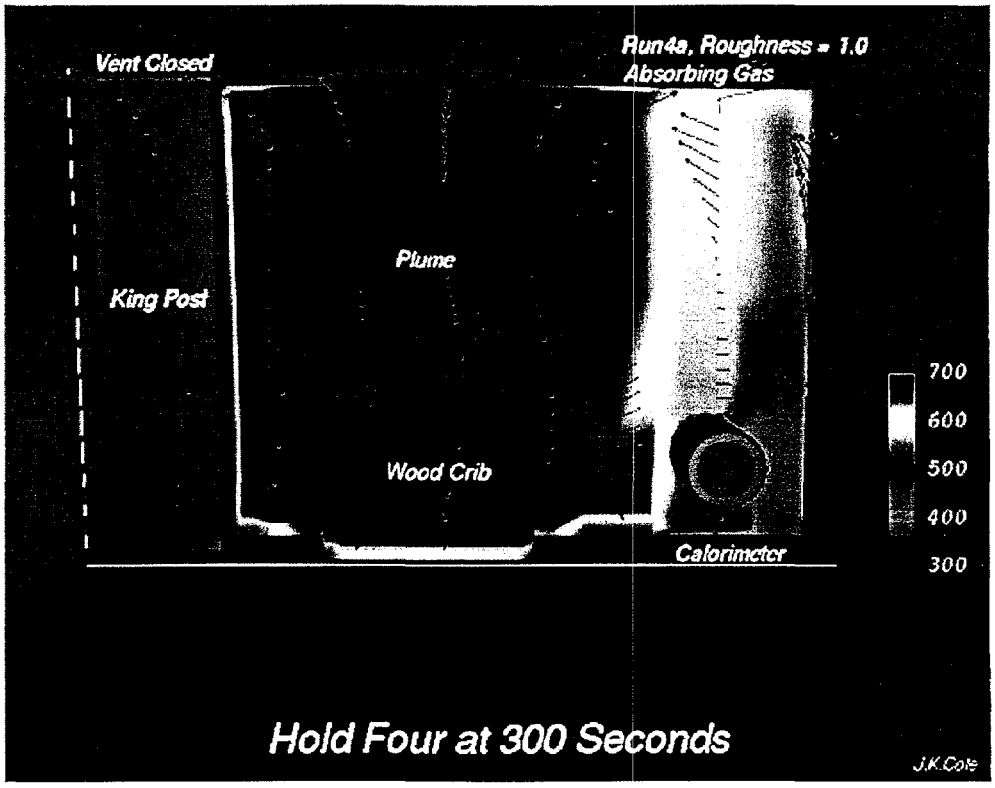

Figure 22. Surface temperatures and flow patterns after 5 minutes of crib fire.

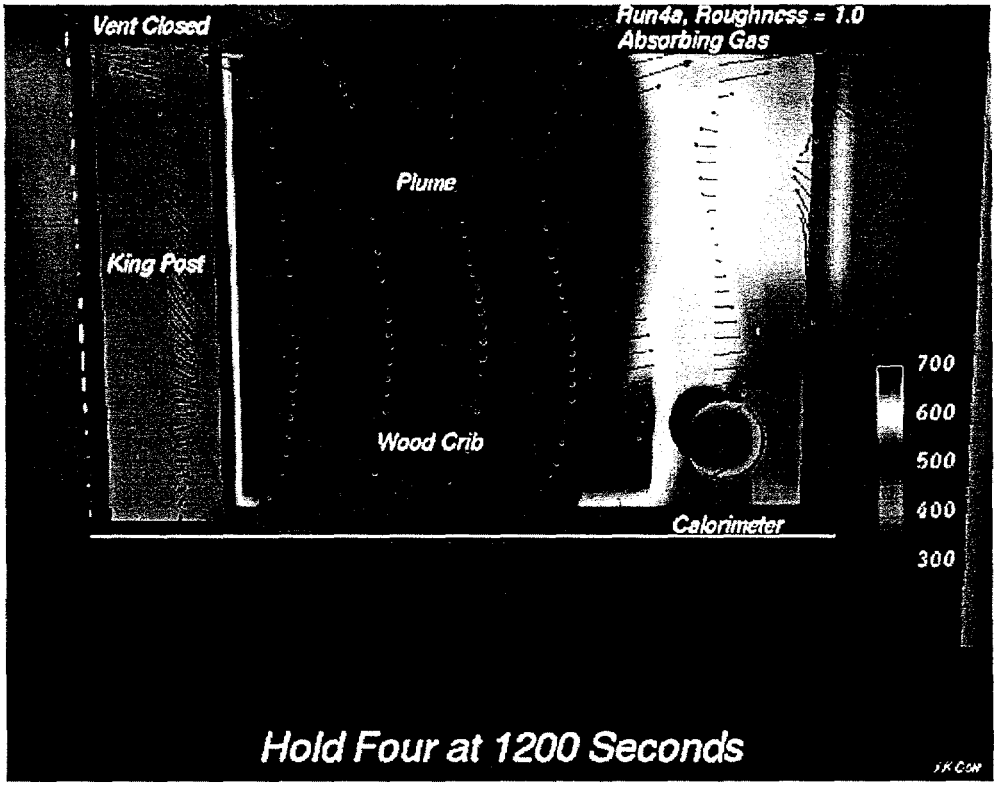

Figure 23. Surface temperatures and flow patterns after 20 minutes of wood crib fire.

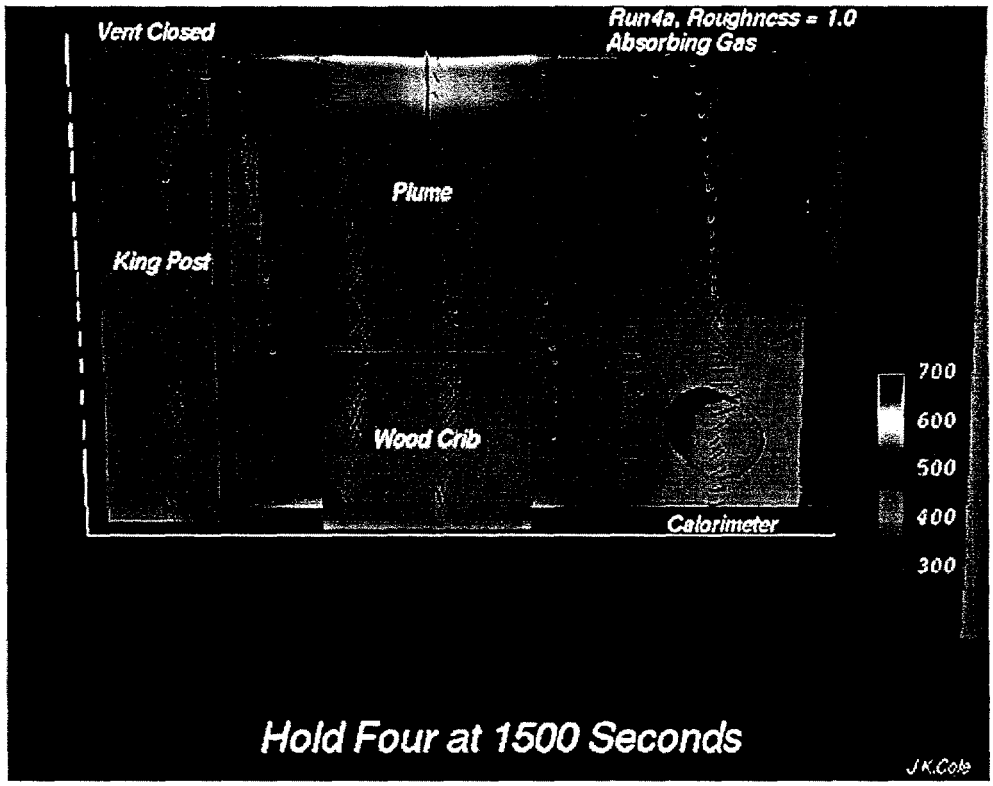

Figure 24. Surface temperatures and flow patterns at 25 minutes after extinguishment of wood crib fire.

3.2 Hold 5 Model Results

3.2.1 Convergence and Residuals

The software allows the user to base the convergence of the solution on several parameters. The convergence criterion in this analysis was based on enthalpy since the problem under analysis is buoyancy driven and energy transport is the major focus of the analysis. Enthalpy is closely related to temperature. For example, when a perfect gas model for air is used, enthalpy can be calculated from the product of the specific heat coefficient at constant pressure and air temperature. The convergence criteria for this analysis was set at 0.1% of the maximum boundary-condition enthalpy. Figures 25 and 26 are residual plots for the two-nozzle and four-nozzle Hold 5 calculation, respectively. Residuals are the sum of the absolute value of error in the computation domain. Thus, the residual plot is an indication of the convergence of the solution. As shown in Figures 25 and 26, the convergence criterion was met at each time step. The large jump in enthalpy residual that occurs at the 60-minute point in both plots is the result of a decrease in the hot-spot temperature at the end of the fire.

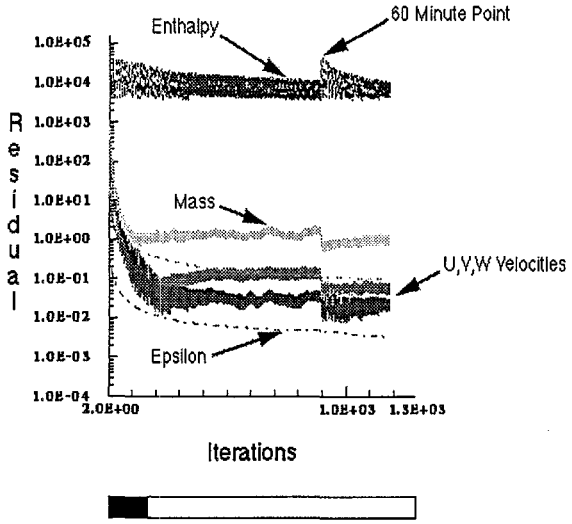

Figure 25. Two-nozzle calculation residual plot.

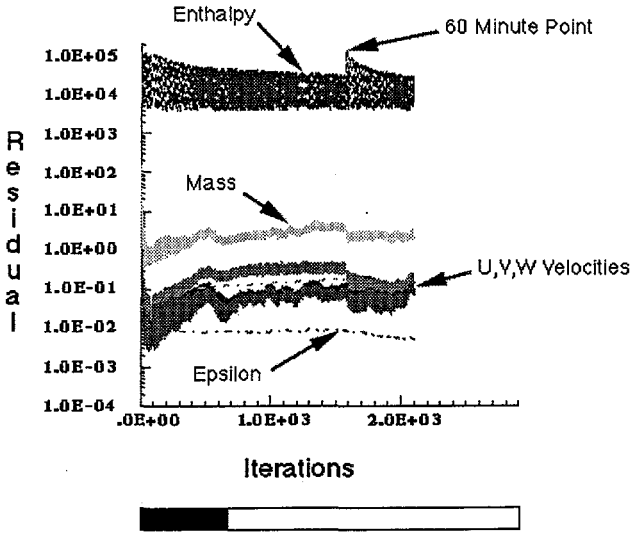

Figure 26. Four-nozzle calculation residual plot.

The maximum allowable number of iterations per time step is a user defined input; the purpose is to prevent a solution from iterating forever at a given time step. The black bar at the bottom of Figures 25 and 26 represents the ratio of actual iterations to maximum number of iterations. Since the bar outline is not full, this indicates that the solution is converging based on the enthalpy convergence criteria. Figures 25 and 26 indicate that there is a high degree of confidence that the solution is converging per time step and thus, that the overall convergence and solution accuracy is adequate.

A significant factor in convergence is the choice of time step. For this analysis, a 1 second time step was initially used. In

order to increase computational throughput, the time step was raised to 15 seconds. The residual plots of both time steps were examined, and temperatures from the analysis were compared. A close agreement in both temperature and the residual plots indicate that a time step of 15 seconds is acceptable.

3.2.2 Flow Patterns

Figures 27, 28, 29, and 30 present streamline plots of the engine-room fire. Streamline plots are zero-mass particle tracks accumulated during the simulation. The streamline plots are based on a plane seeding of the zero-mass particles. The seeding plane is parallel to the model plane-of-symmetry and passes through the midpoint of the calorimeter half.

Figures 27 and 28 show the flow patterns for the two-nozzle calculation at 30 and 60 minutes, respectively. The figures show the development of fluid flow around the furnace and a plume above the calorimeter. A large convection cell is forming in the aft section of the hold. The convection cell is quite apparent in Figure 28.

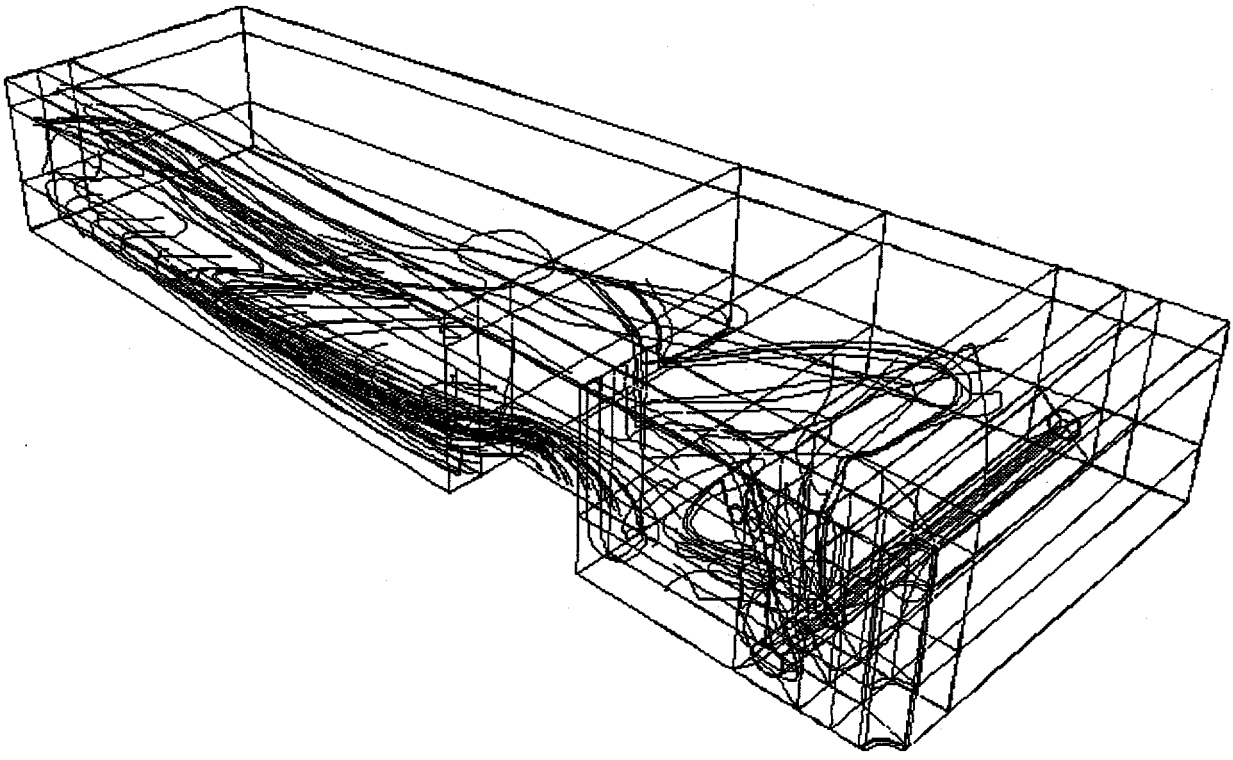

Figure 27. Two-nozzle flow pattern at 30 minutes.

Figures 29 and 30 show the flow patterns for the four-nozzle calculation at 30 and 60 minutes, respectively. As in the two-nozzle calculation, fluid flow is developing around the furnace, and a plume above the calorimeter also formed, although the plume is not as apparent in the four-nozzle calculation. The lower ambient temperature of the four-nozzle calculation may contribute to the less prominent plume above the calorimeter. A large convection cell in the rear section of the hold also formed during the four-nozzle calculation.

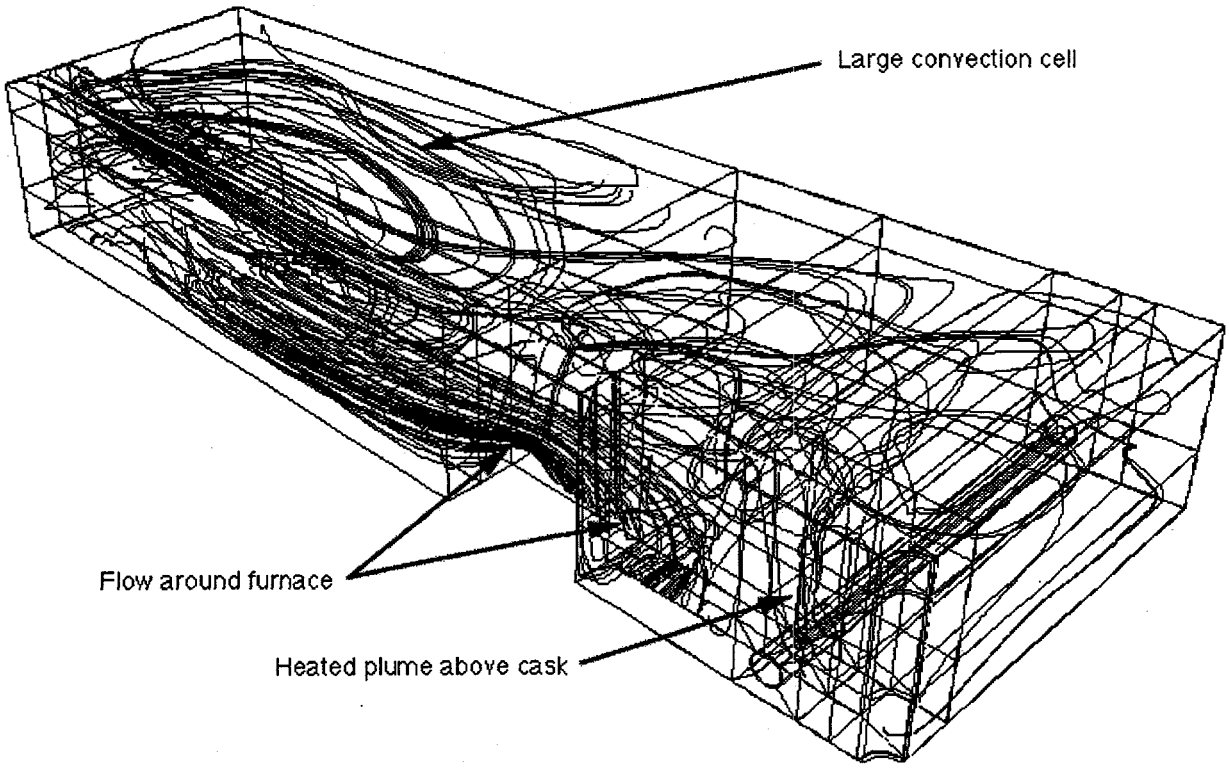

Figure 28. Two-nozzle flow pattern at 60 minutes.

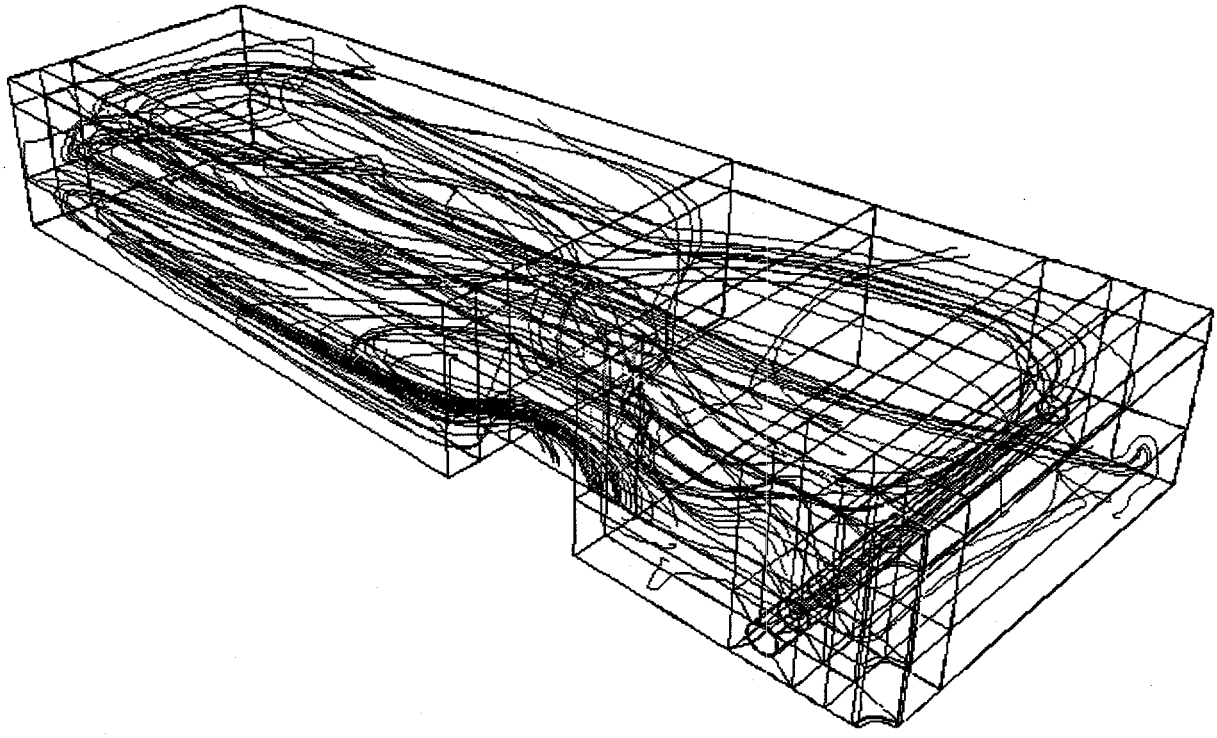

Figure 29. Four-nozzle flow pattern at 30 minutes.

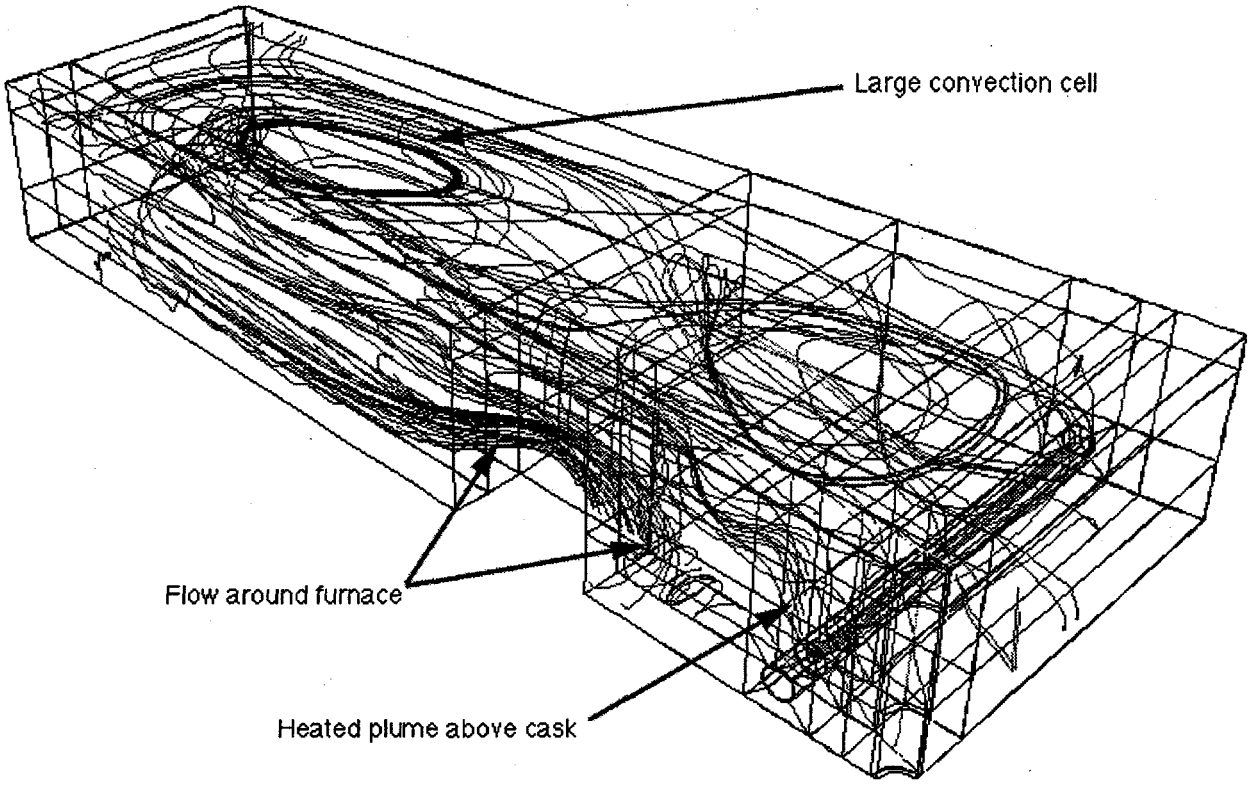

Figure 30. Four-nozzle flow pattern at 60 minutes.

The plots also show that the formation of the convection cell is a long-term event. The long formation time is an indicator of the relatively minor contribution of convection-heat transfer.

3.2.3 Surface Temperature Comparisons

The analytical and experimental data were compared at seven locations on the calorimeter. Three of the analytical temperature locations (60, 120 and 240 degrees from vertical) coincided with experimental thermocouple positions. The remaining four temperature comparisons (0, 90, 180 and 270 degrees from vertical) used the average analytical temperature from analytical temperature locations on either side of the experimental thermocouple location. The analytical temperature locations were 4.5 degrees on either side of the experimental thermocouple location. Figure 14 presents the experimental and calculated temperature locations used for data comparison.

Figure 31 is a time-temperature comparison, at 0, 60 and 90 degree locations on the calorimeter, for the two nozzle model calculation and experimental data. The calculated temperatures are lower than the experimental temperatures, but are still a reasonable estimation. The distribution of temperatures between the experimental data and the calculated data shows similar trends. The 60-degree location has the highest temperature for both the experimental and calculated data, while the 0-degree location has the lowest temperature for both the experimental and analytical data. The plot also shows that the peak temperature occurs at the same time for both sets of data. The peak temperature occurs at 62 minutes. The difference in temperature between the experimental

data and analytical calculations could be caused by differences in hot spot area, hot spot position, or flame temperature. or combinations of these three factors.

Figure 32 is a time-temperature plot at 120, 180, 240, and 270 degrees from vertical on the calorimeter for the two-nozzle model calculation. The peak temperature difference between the experimental and calculated temperatures is 2°C and occurs at 120 degrees from vertical on the calorimeter. The 120 degree location is where the peak temperature occurs for both the experimental data and the calculations. The peak temperature occurs at 65 minutes for both the experimental and calculations.

Figure 33 is a time-temperature comparison, at 0, 60 and 90 degrees from vertical on the calorimeter, for the four-nozzle model calculation and experimental data. The peak temperature difference between the experimental and calculated temperatures is 1°C and occurs at the 60 degree location on the calorimeter. The calculation temperatures encompass the experimental temperatures with the calculated temperatures at the 90 degree location lower that the experimental temperature data at that location. The temperature distribution indicates that either the hot-spot area or the hot-spot position or some combination of these differed from the experiment. The peak temperature occurs at the same 65-minute time for the calculated and experimental temperature data.

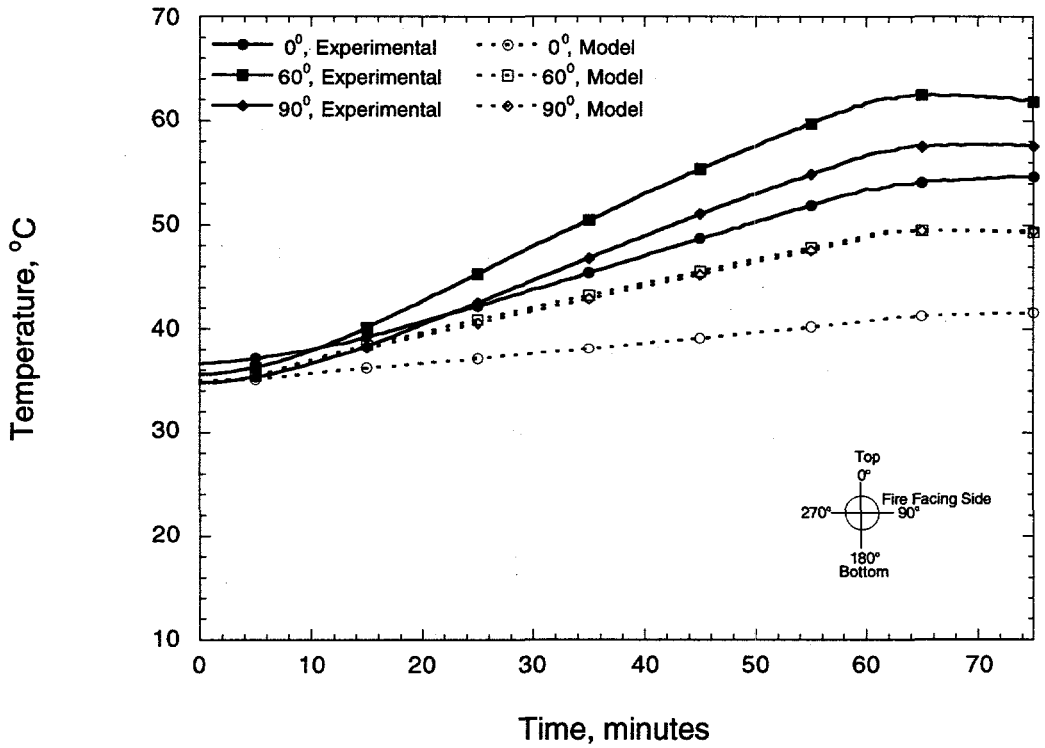

Figure 31. Two-nozzle temperature comparison at 0, 60 and 90 degrees.

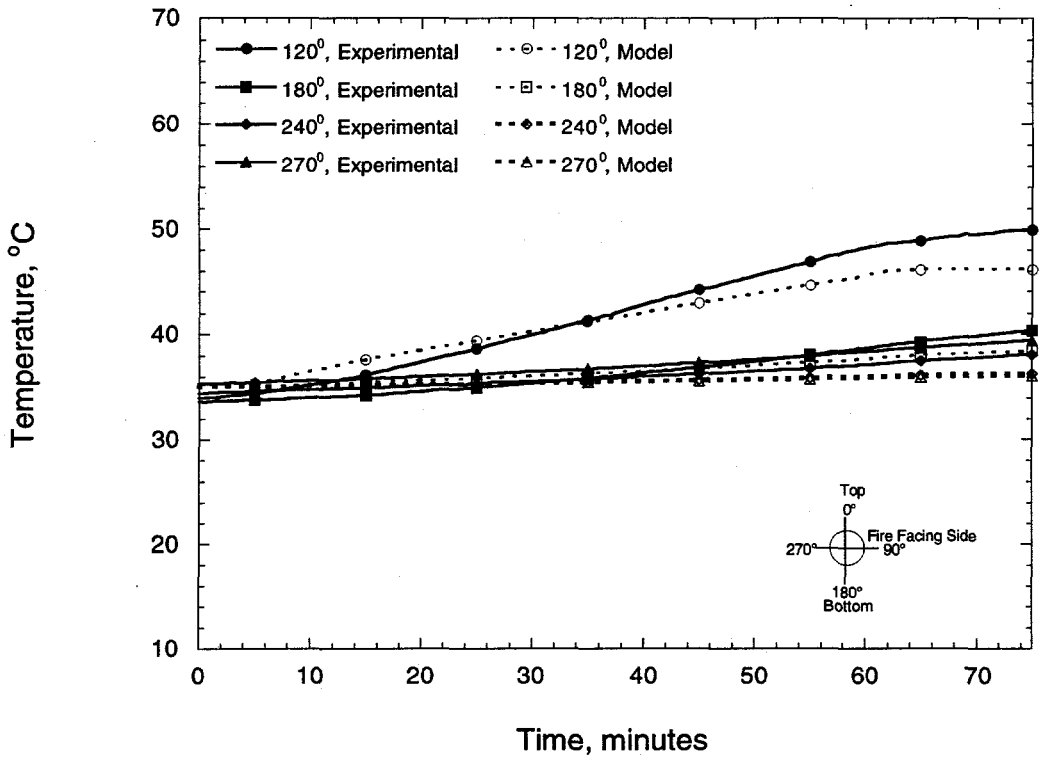

Figure 32. Two-nozzle temperature comparison for 128, 180, 240 and 270 degrees.

Figure 34 is a time-temperature plot at 120, 180, 240, and 270 degree locations on the calorimeter for the four-nozzle model calculation. The calculated temperatures are higher than the experimental data at the 120 degree calorimeter location. The remaining temperatures at 180, 240 and 270 degree locations on the calorimeter, agree within 2°C of the experimental values.

Figures 35 and 36 are circumferential temperature plots at 30 minutes for the two- and four-nozzle cases. Since 30 minutes is half way through the burning time, this time was chosen to represent a typical circumferential temperature distribution. The peak calculated temperature for the two-nozzle case, presented in Figure 35, is lower than the peak experimental temperature, but the temperature distribution is comparable. A shift in the maximum and minimum temperatures which is probably caused by differences between actual and simulated hot spot areas and positions.

The peak calculated temperature for the four-nozzle case, presented in Figure 36, is higher than the peak experimental temperature. The temperature distribution of the is similar for both calculated and experimental temperatures. Again, a shift in the location of the maximum and minimum temperature is observed between the two curves.

3.2.4 Heat Flux Comparisons

Figures 37, 38, 39 and 40 present calculated surface-heat-flux plots of the calorimeter. SODDIT [6] was used to calculate the surface heat fluxes. The same code and procedure was used to calculate surface heat fluxes from the experimental data.

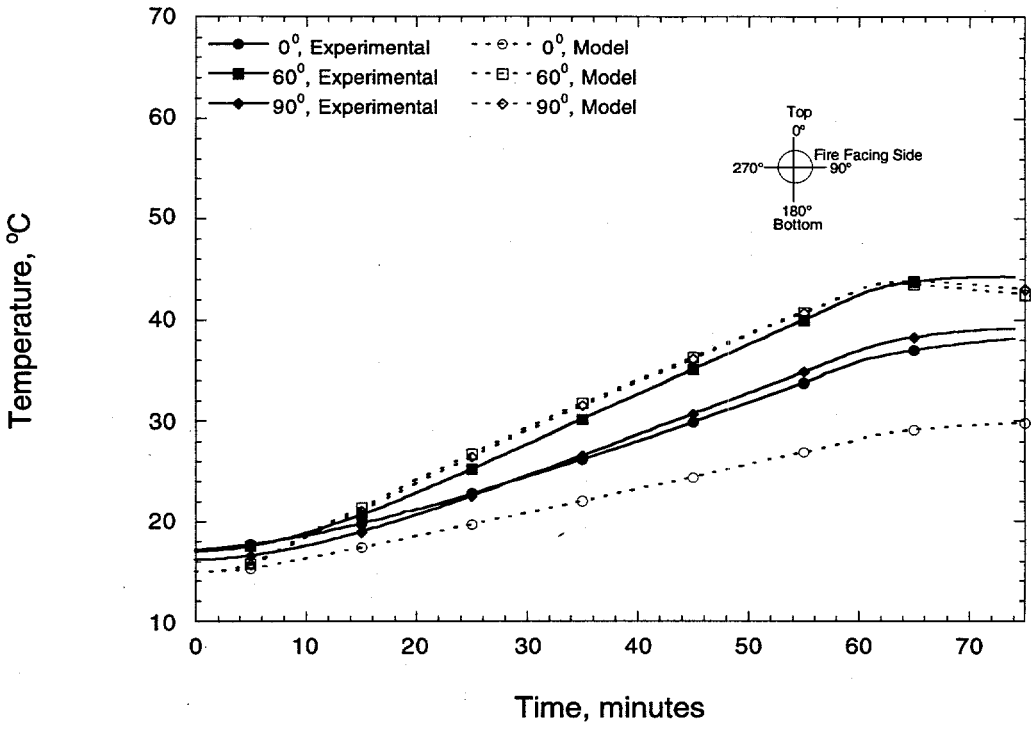

Figure 33. Four-nozzle temperature comparison at 0, 60 and 90 degrees.

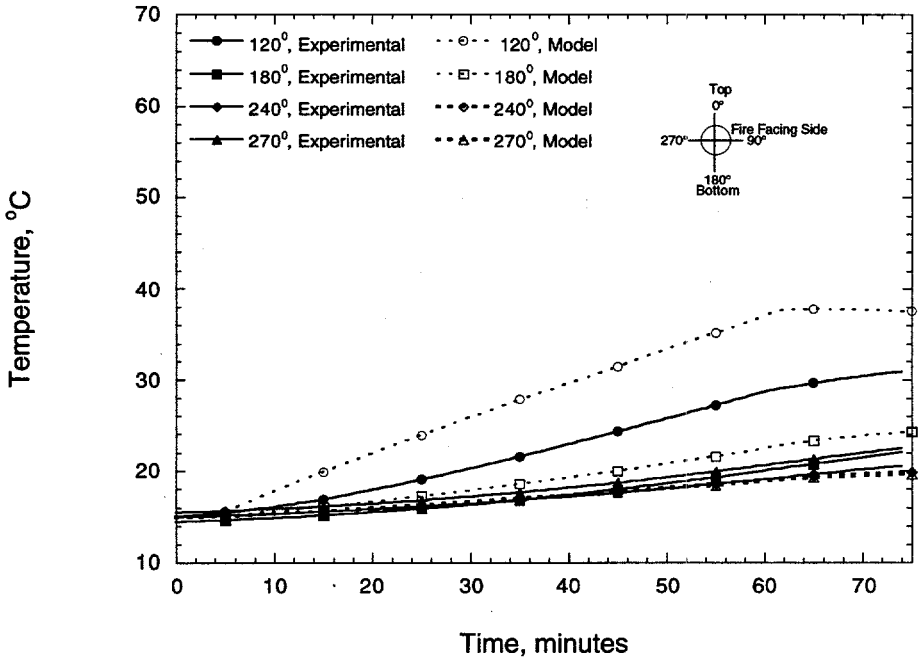

Figure 34. Four-nozzle temperature comparison for 120, 180, 240 and 270 degrees.

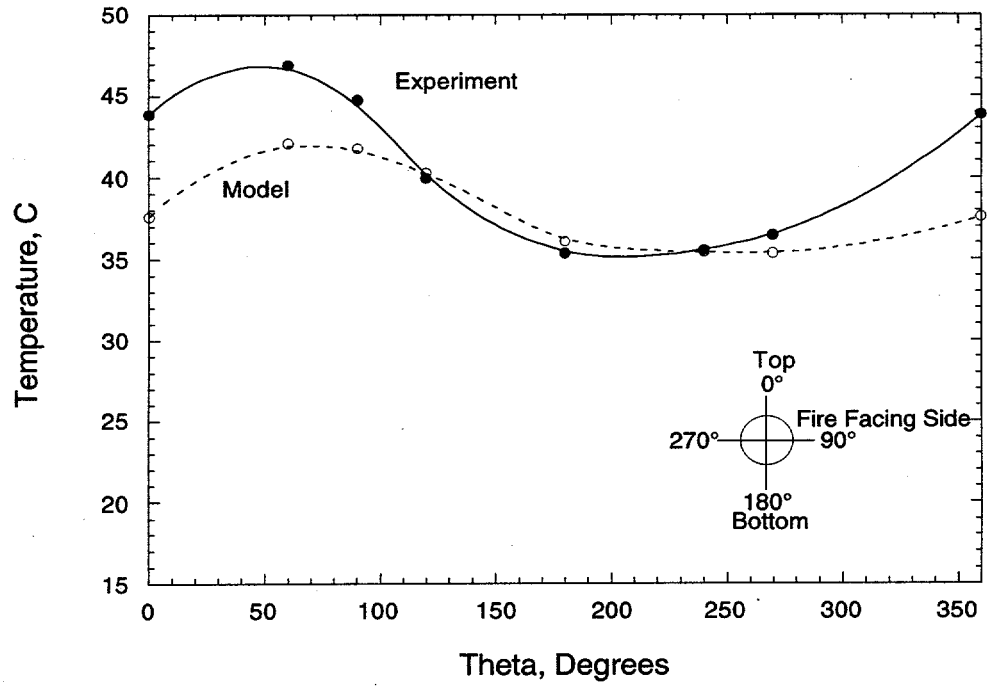

Figure 35. Two-nozzle circumferential temperature distribution at 30 minutes.

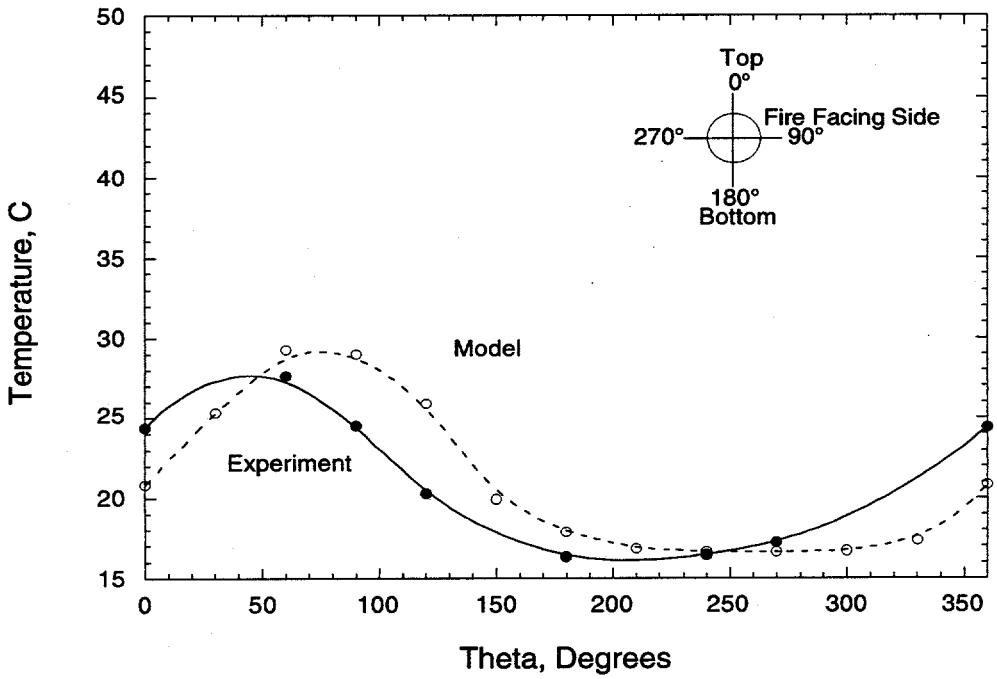

Figure 36. Four-nozzle circumferential temperature distribution at 30 minutes.

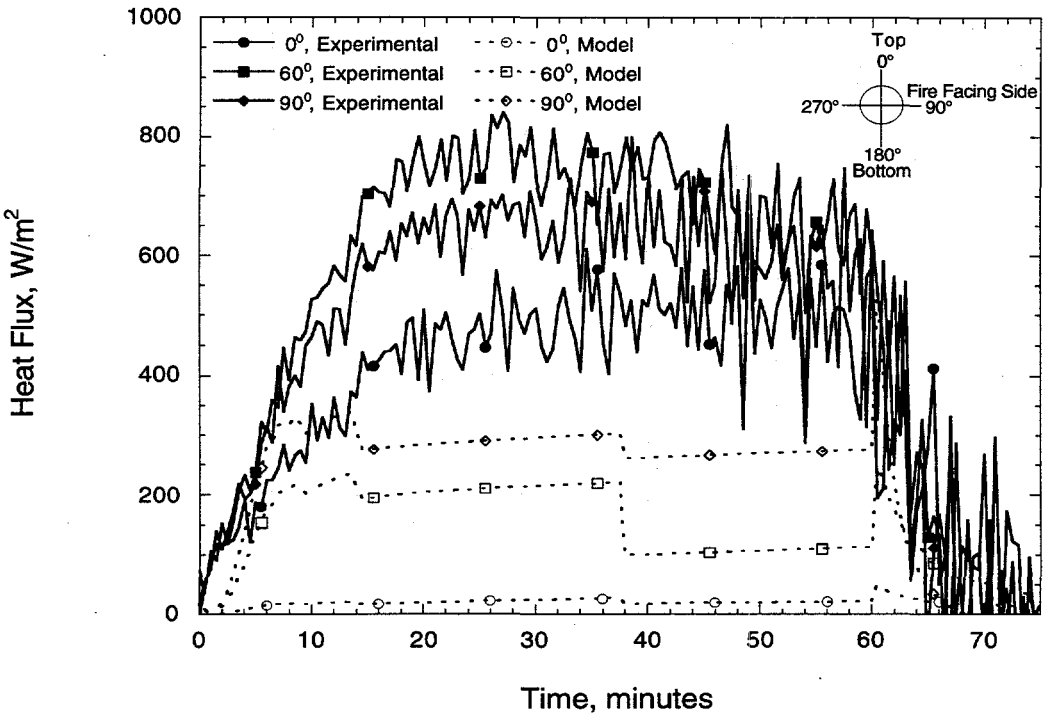

Figure 37. Two-nozzle heat flux comparison at 0, 60 and 90 degrees.

Figure 37 is the surface-heat-flux plot for the two-nozzle case. The calculated heat fluxes are of the same order-of-magnitude as the experimental data. Figure 38 is the surface-heat-flux plot of the two-nozzle case. Again, the heat fluxes are within the range of heat fluxes calculated from the experimental data.

Figures 39 and 40 are circumferential heat-flux plots at 30 minutes for the two-nozzle and four-nozzle cases, respectively. The heat fluxes are of the same order of magnitude as the experimental data. A shift in the maximum and minimum heat flux, similar to what was observed in the circumferential temperature plots is evident. The positional shift is probably a result of forward-bulkhead hot-spot area and position differences.

3.2.5 Radiation/Convection Heat Transfer Partitioning

The CFD model was used to estimate the partitioning of convection and conduction components of the overall heat-transfer mechanism and the importance of the radiative heat-transfer mechanism for heat transferred to the calorimeter. The partitioning was accomplished by removing buoyancy from the convection model and by the use of a small value of thermal conductivity for the air to minimize conduction. The calculations were made with the same Hold 5 computer model, boundary conditions and other factors such as time step.

Figure 41 is a comparison of the calorimeter surface temperatures with and without convection of, and conduction through, the air. The plot indicates that convection is a minor contributor to the heat transfer that occurs in this problem, since there is no appreciable difference between the two sets of temperature data. However, the plot also shows that convection occurs, and for other ship-fire problems or other locations in the hold, convection could be more significant. As seen in the

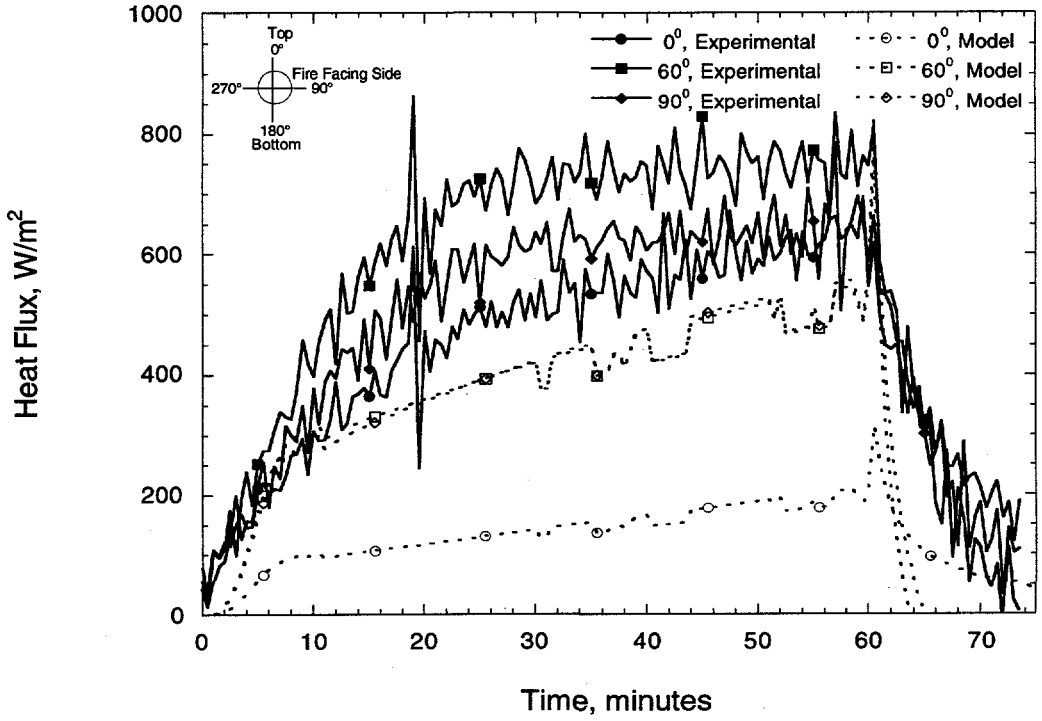

Figure 38. Four-nozzle heat flux comparison at 0, 60 and 90 degrees.

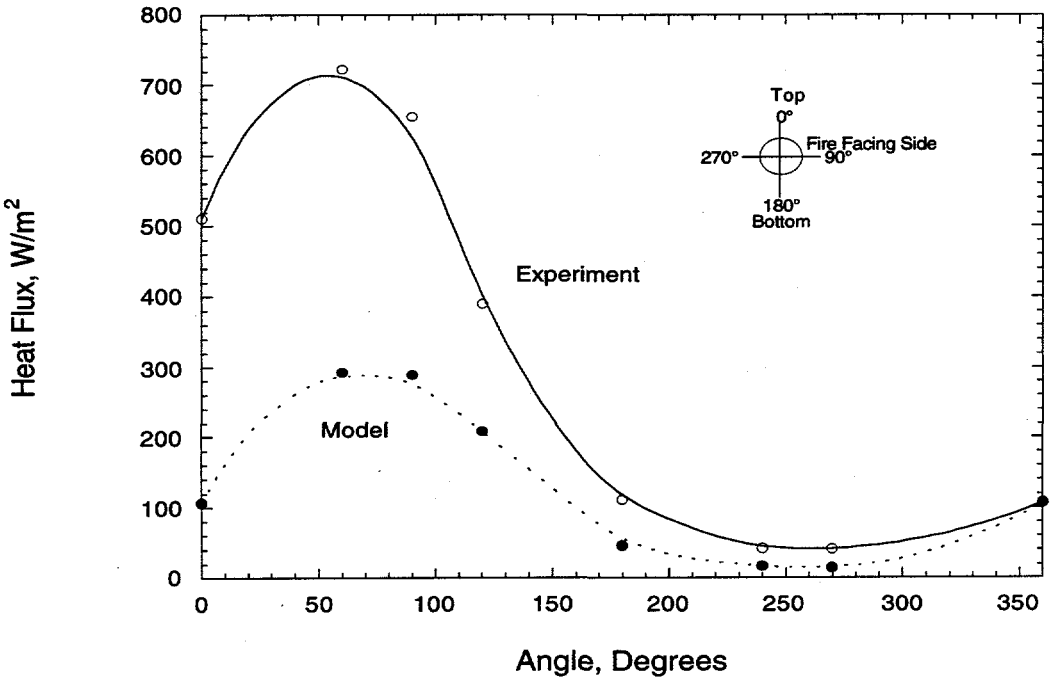

Figure 39. Two-nozzle circumferential heat flux distribution at 30 minutes.

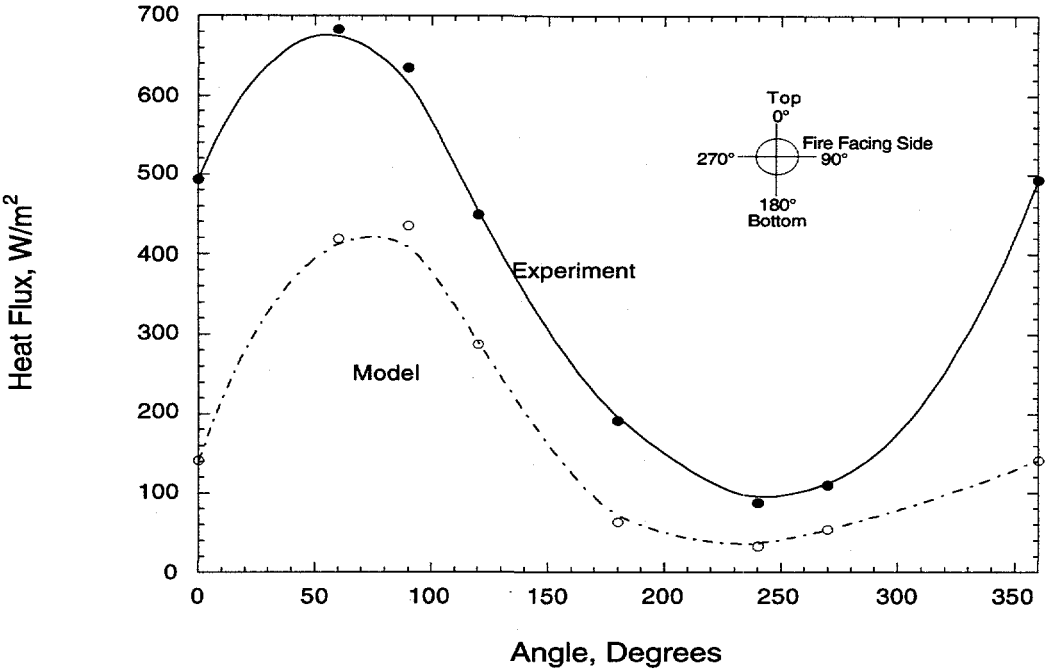

Figure 40. Four-nozzle circumferential heat flux distribution at 30 minutes.

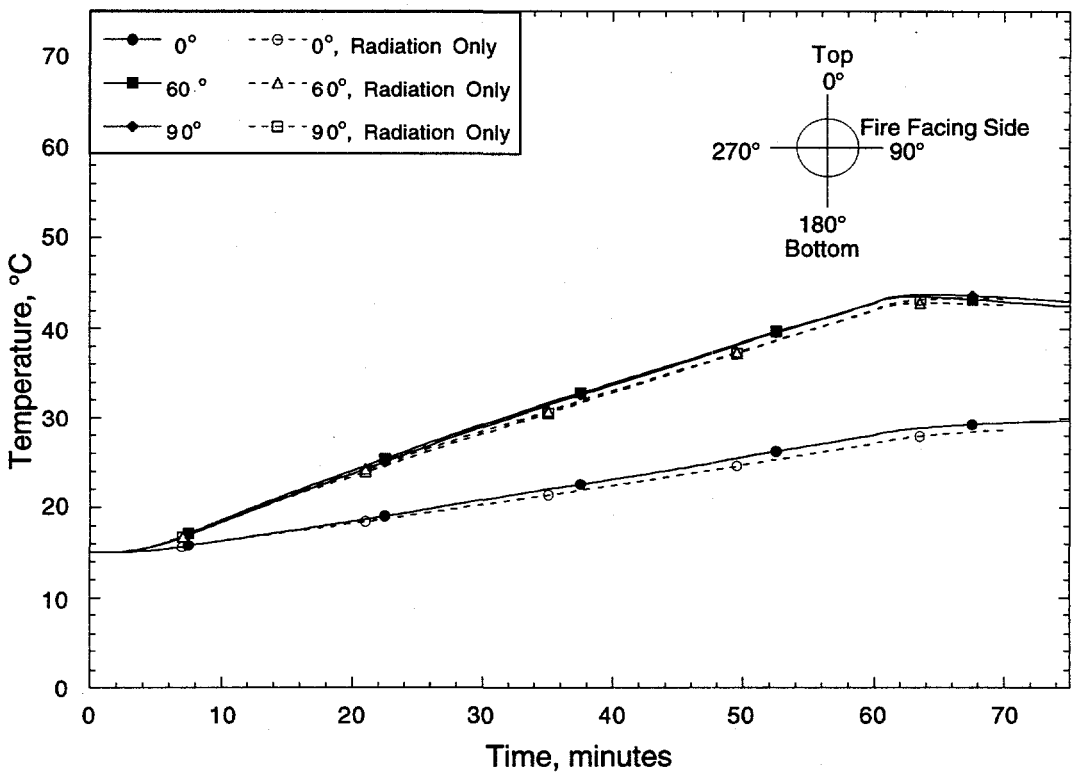

Figure 41. Comparison of the calorimeter surface temperature with and without convection of, and conduction through the fluid.

streamline plots, a large convection cell formed in the aft part of the hold. If the calorimeter were located in the aft part of the hold, convection could make a larger contribution to the overall heat transfer. Another location where convection contributes to the overall heat transfer mechanism is at just aft of the front bulkhead where the hot spots are. The convection driving potential is larger in this area due to the larger temperature difference between the air and heated surface.

3.2.6 Color Fringe Plot Results

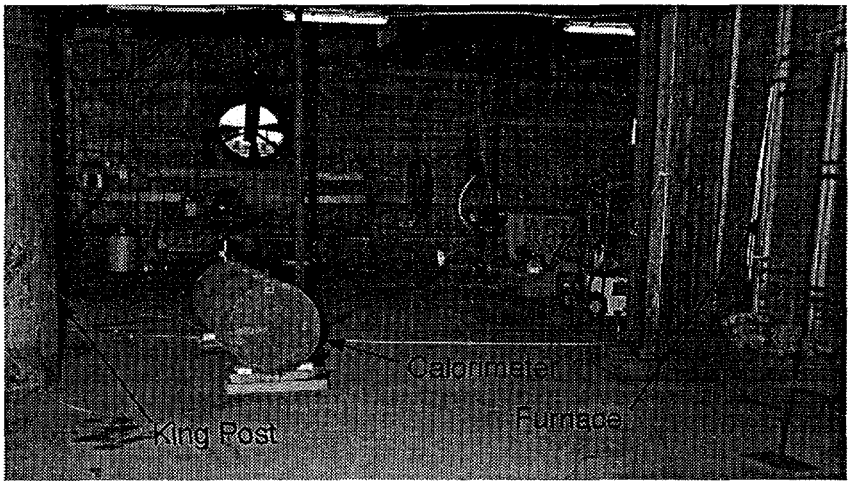

Figure 42. Hold 5 experimental configuration.

Figure 42 shows Hold 5 from about the same viewpoint as the color fringe plots. The features visible in the color fringe plots are also indicated in Figure 42. The primary features are the King post, the calorimeter, and the furnace.

Figure 43 presents a color fringe temperature plot and an air-flow vector plot of the two-nozzle case at 60 minutes. The forward bulkhead hot spot, corresponding to an engine-room fire in the adjacent hold, can be seen at the far left of the figure next to the King post. The temperature mapping displays the hottest region of the calorimeter, which is the cylindrical object near the middle of the figure. The white circular lines are locations of possible flow-recirculation cells and the arrow indicates the direction of flow. A recirculation cell occurs in front of the furnace near the overhead. The recirculation cell may cause some flow blockage over the top of the furnace, forcing the flow around the furnace, as shown in the streamline plots. There is also a recirculation cell in front of furnace near the deck. Part of the recirculation cell could cause the air flow observed beneath the calorimeter. A third recirculation cell occurs near the front bulkhead just above the midpoint between the deck and the overhead. Recirculation in this area would reduce the amount of convective heat transfer to the calorimeter. Also note that there is upward flow at the front bulkhead and above the calorimeter.

The arrows directly over the calorimeter show an upward flow of air. This upward flow was observed over the calorimeter, by using flow visualization techniques, in the experimental data. The temperature plots also reveal the plume that is formed above the calorimeter. The plume was caused by heating of the calorimeter by the engine-room fire and in turn heating the local air, near the calorimeter, which caused convective flow to occur. Another feature of the flow is the recirculation occurring under the calorimeter.

Figure 44 presents a color-fringe temperature plot and air-flow vector plot of the four-nozzle case at 60 minutes. The forward bulkhead hot spot can be seen at the far left of the figure next to the King post. A second hot spot exists further away from the King post. The temperature mapping displays the hottest region of the calorimeter, which, again, is the cylindrical object near the middle of the figure. Two of the recirculation cells that occurred in the two-nozzle case also occurred

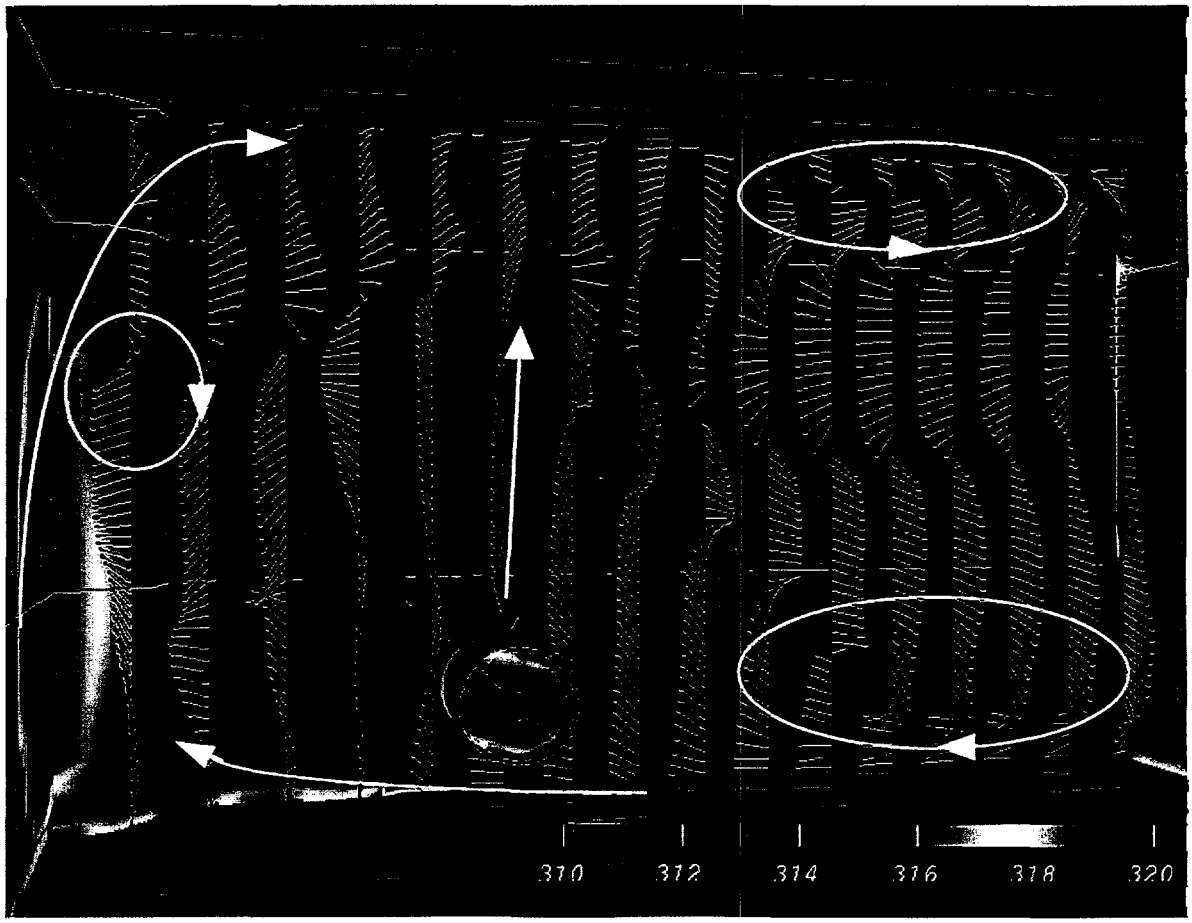

Figure 43. Two-nozzle temperature and velocity vector plot at 60 minutes.

in the four-nozzle case. The recirculation cell in front of the furnace near the overhead is larger than the corresponding recirculation cell in the two-nozzle case. The recirculation cell that was in front of the furnace and near the deck in the two-nozzle case has moved forward and has decreased in size. The recirculation cell that was near the front bulkhead in the two nozzle case is not present, and another recirculation cell has formed directly in front of the calorimeter and, the latter is smaller than the recirculation cell near the front bulkhead in the two-nozzle case.

As in the two-nozzle case, upward flow occurs near the front bulkhead and above the calorimeter. Flow also occurs under the calorimeter. Upward flow was also evident in the experimental data. A series of flow-visualization devices were constructed directly above the calorimeter. Review of videotape of Hold 5 taken during the tests show the upward flow from the flow visualization devices.

Additional color-fringe and flow vector-plots for the two-nozzle and four-nozzle cases are presented in Appendix B. In each image, the engine-room fire occurs to the left, the calorimeter is the cylinder in the middle, and the furnace is to the right. The arrows in each plot are vector plots of the flow direction and a bar scale at the bottom indicates temperature in kelvins.

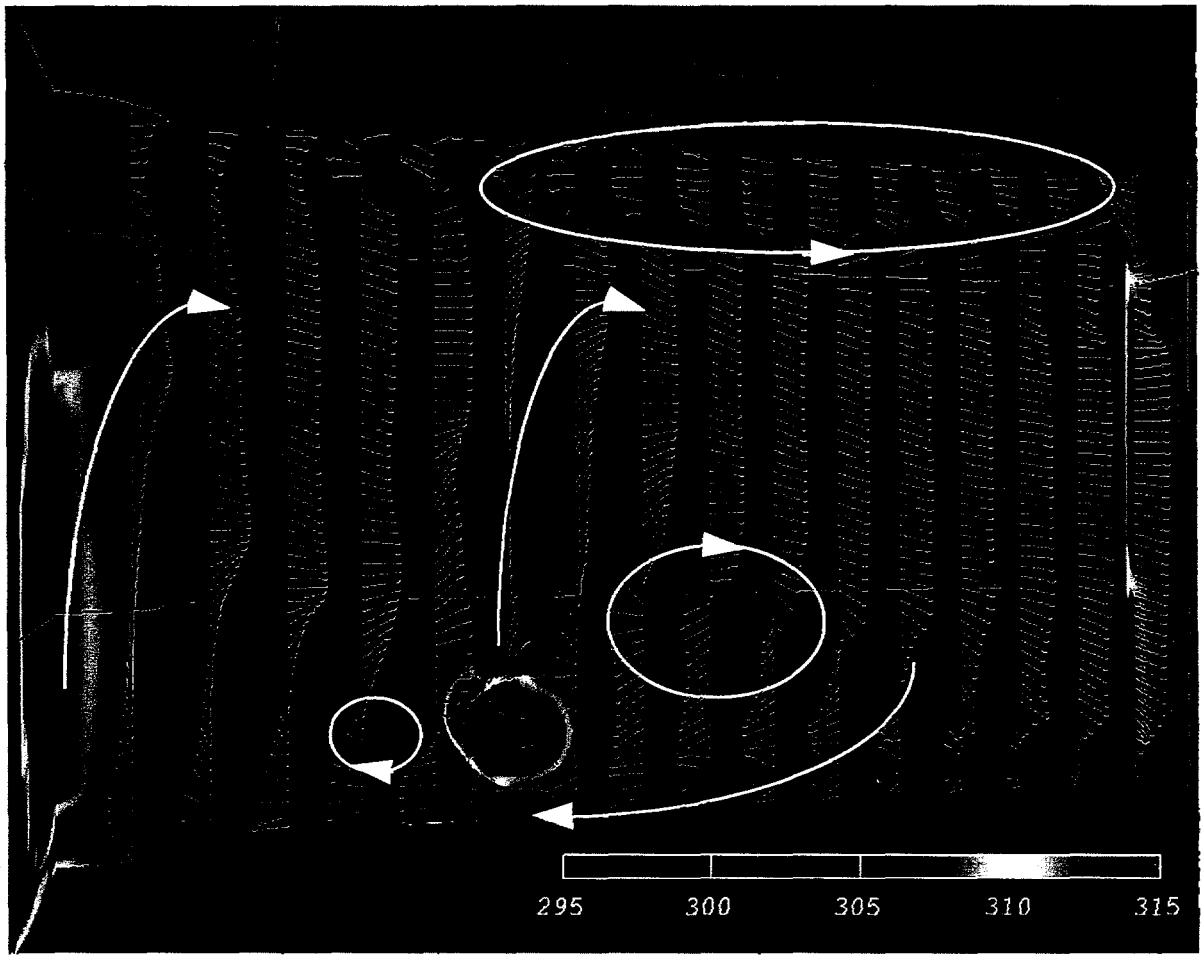

Figure 44. Four-nozzle temperature and velocity vector plot at 60 minutes.

4.0 CONCLUSIONS

The analyses described in this report demonstrate that models that accurately estimate a maritime fire environment for a radioactive material packaging can be developed from basic ship-hold geometry and a simplified fire heating source. Overall, package temperature estimates within 10-20° C are possible, and the locations and magnitudes of peak heat fluxes can also be successfully predicted. In addition, the calculated-temperature and heat-flux time responses are comparable to the experimental curves. A package design based on such simulations would be expected to survive similar accidents at sea.

A key finding is that radiative heat transfer dominates the hold-fire environment near the hot bulkhead. This was determined by effectively eliminating the convective heat transfer mechanism in the simulations, and then comparing the results to calculations that included convection. For the package locations studied, no significant difference in results was detected. This indicates that simpler models based only on radiative heat transfer and conduction could yield accurate predictions in the future. However, convection should not be ruled out entirely for every ship hold thermal analysis. There could be localized regions, for example away from the fire location or hot bulkhead, where convection could make a significant contribution to the heat-transfer process.

The simulations showed that the development of convection patterns in the hold was a relatively long-term process. Large convection cells did not develop in the aft end of Hold 5 until later in the one hour fire simulation. Smaller convection cells formed near the forward bulkhead on a much shorter time scale. The long time scale for formation of convections cells at the aft end of the hold is another indicator that convective-heat transfer does not dominate during the initial part of the fire.

The analyses also showed that effective flame temperatures in the range of 800 to 1000° C, when coupled with estimates of fire heat release, can give heat fluxes and temperatures typical of the measured fire environment for the simulated radioactive material package. The agreement obtained with three different-sized fire sources shows that scaling to larger fires should be successful.

This analysis demonstrated that flow patterns can be estimated with reasonable accuracy using a course mesh CFD ship-hold model. The simulation predicted the occurrence of flow patterns near the calorimeter similar to those observed during the experiment. In the simulation and experiment, there was an upward flow above the calorimeter. The flow pattern above the calorimeter was captured on video during the experiment by use of flow visualization devices. The simulation also predicted a heated fluid layer near the ceiling that increases in thickness as time passes. The increase in thickness of a heated fluid near the ceiling has been witnessed during experiments.

5.0 REFERENCES

1. "Study and Implementation Plan on Safety of Shipments of Plutonium by Sea," *Section 2904 of the Energy Policy Act of 1992,* U. S. Congress, Washington, DC, 1992.

2. J. A. Koski, J. G. Bobbe, M. A. Arviso, S. D. Wix, D. E. Beene, Jr., R. Byrd, and J. Graupmann, *Experimental Determination of the Shipboard Fire Environment for Simulated Radioactive Material Packages*, SAND-0506, Sandia National Laboratories, Albuquerque, NM, March 1997.

3. *CFX-F3D User Manual, Version 4.1*, AEA Technologies, Pittsburg, PA, October, 1995.

4. S. V. Patankar, *Numerical Heat Transfer and Fluid Flow*, McGraw-Hill Book Company, New York, 1980.

5. *Handbook of Geophysics and Space Environment,* USAF Geophysics Laboratory, 1985.

6. B. F. Blackwell, R. W. Douglass, and H. Wolf, *A User's Manual for the Sandia One-Dimensional Direct and Inverse Thermal (SODDIT) Code*, SAND85-2478, Sandia National Laboratories, May, 1987.

Appendix A

Additional Results from Hold 4 Wood Crib Fire Simulations

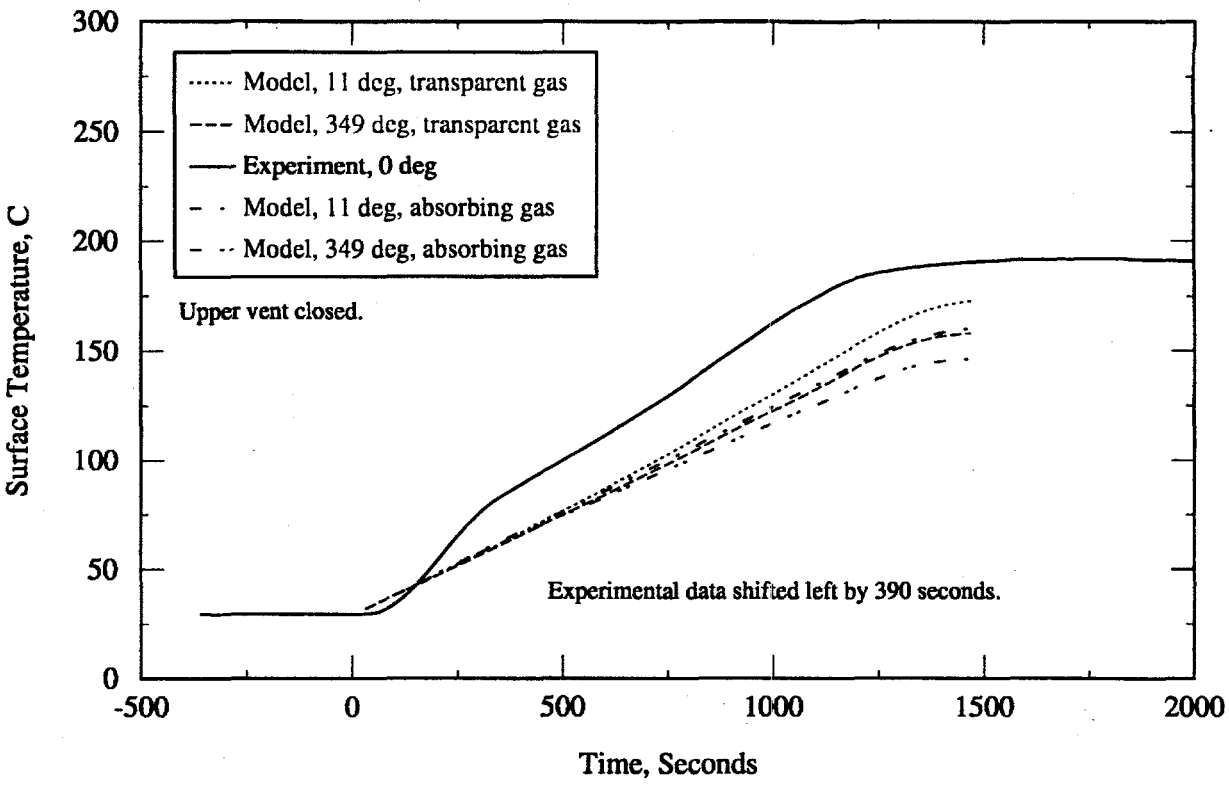

Figure A-1. Calormeter surface temperatures for model and experiment near 0 degrees.

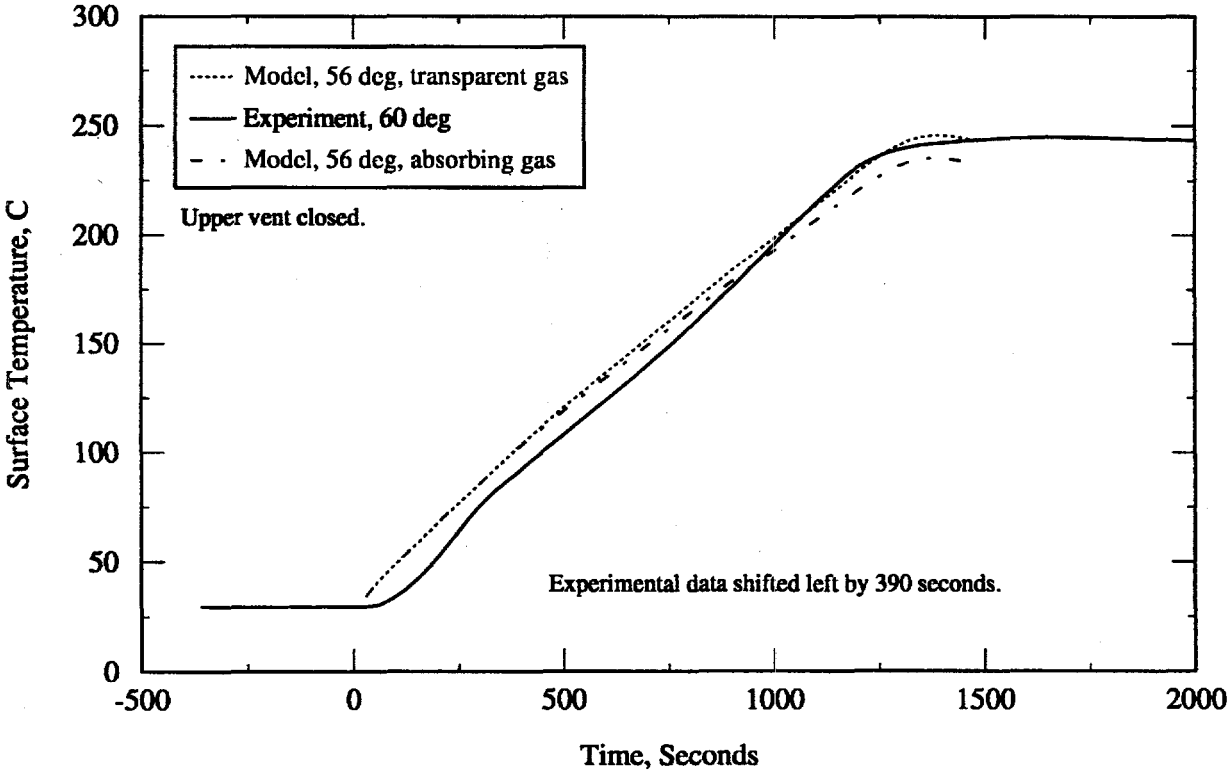

Figure A-2. Calorimeter surface temperatures for model and experiment near 60 degrees.

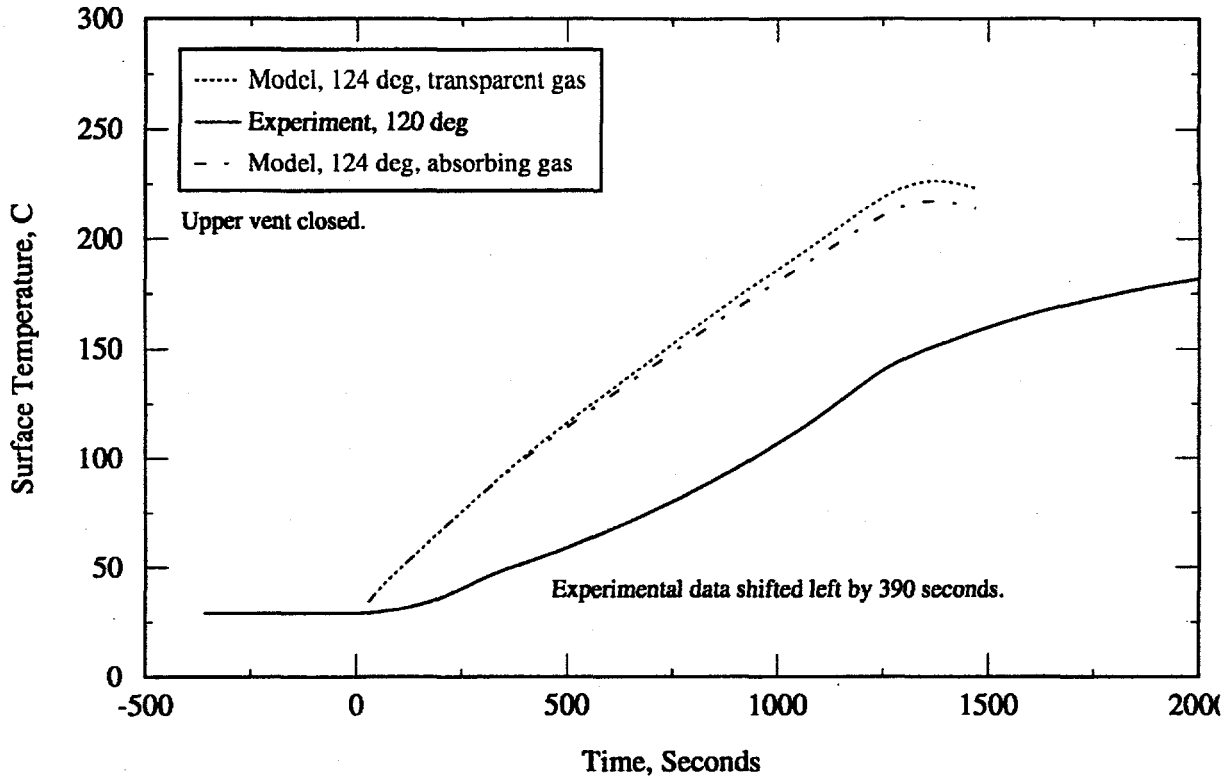

Figure A-3. Calorimeter surface temperatures for model and experiment near 120 degrees.

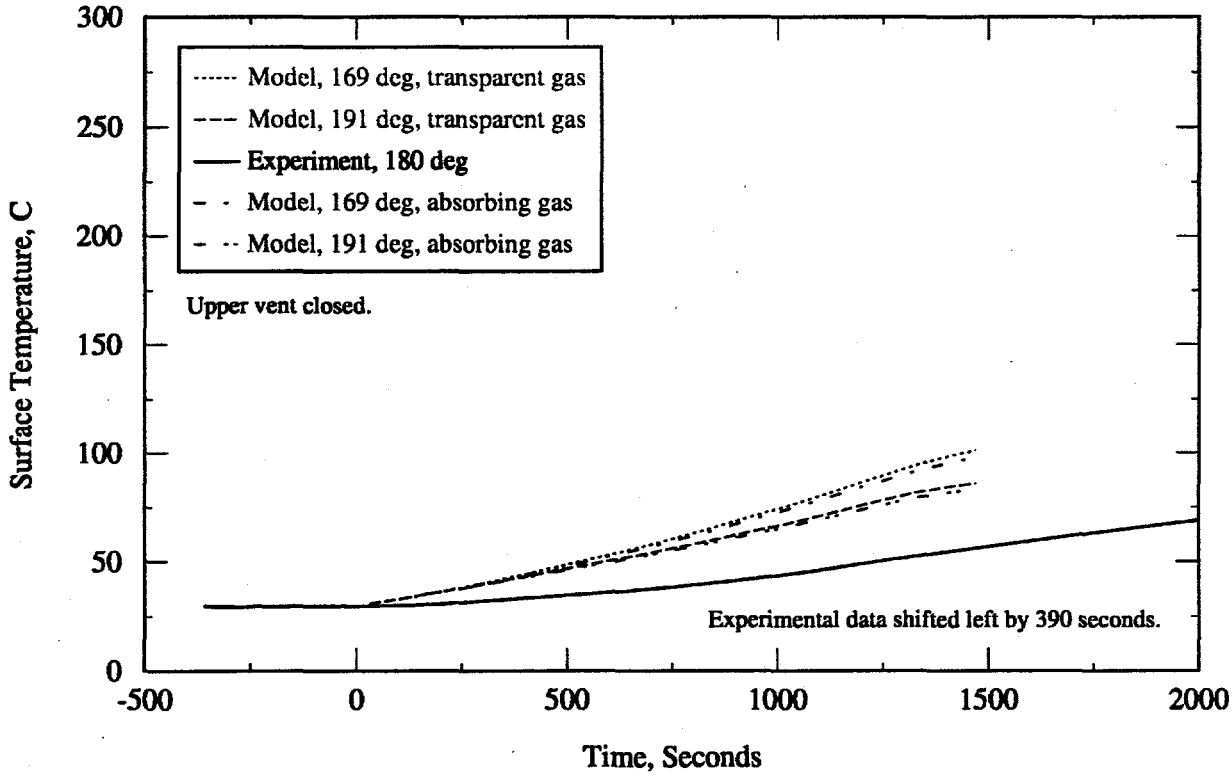

Figure A-4. Calorimeter surface temperatures for model and experiment near 180 degrees.

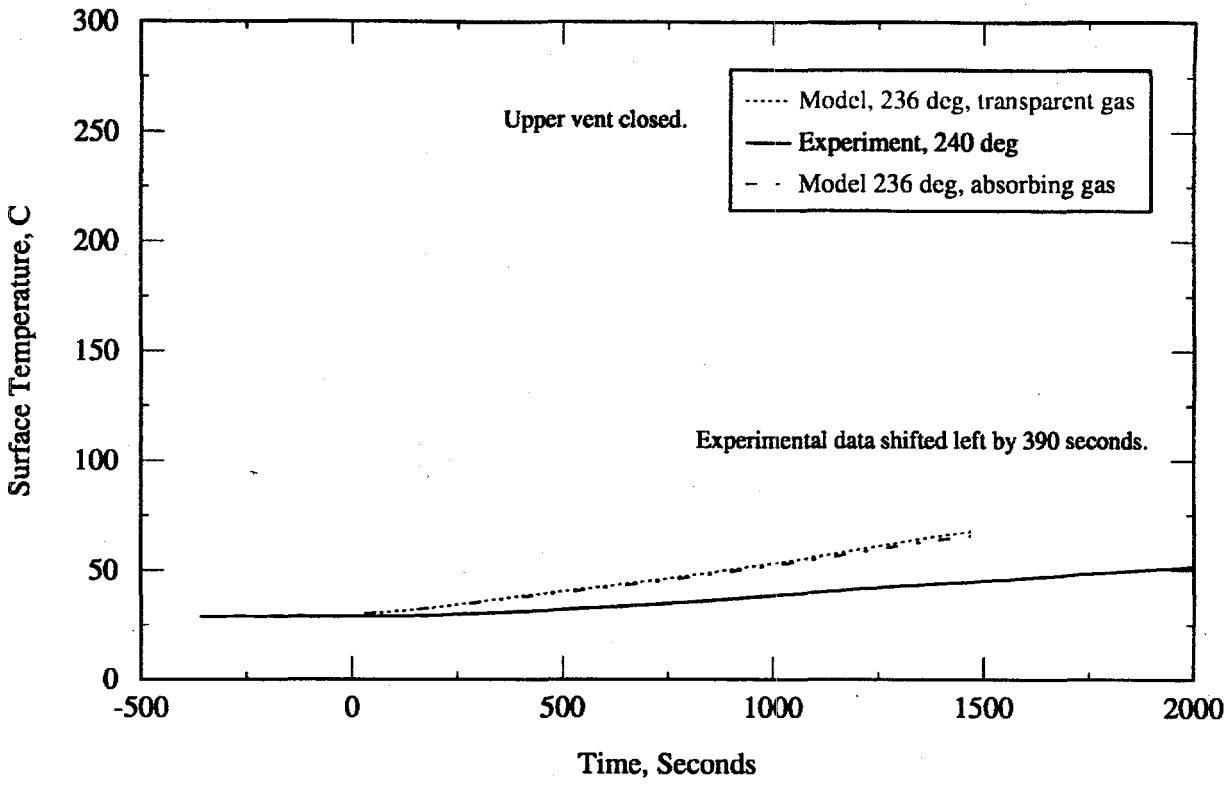

Figure A-5. Calorimeter surface temperatures for model and experiment near 240 degrees.

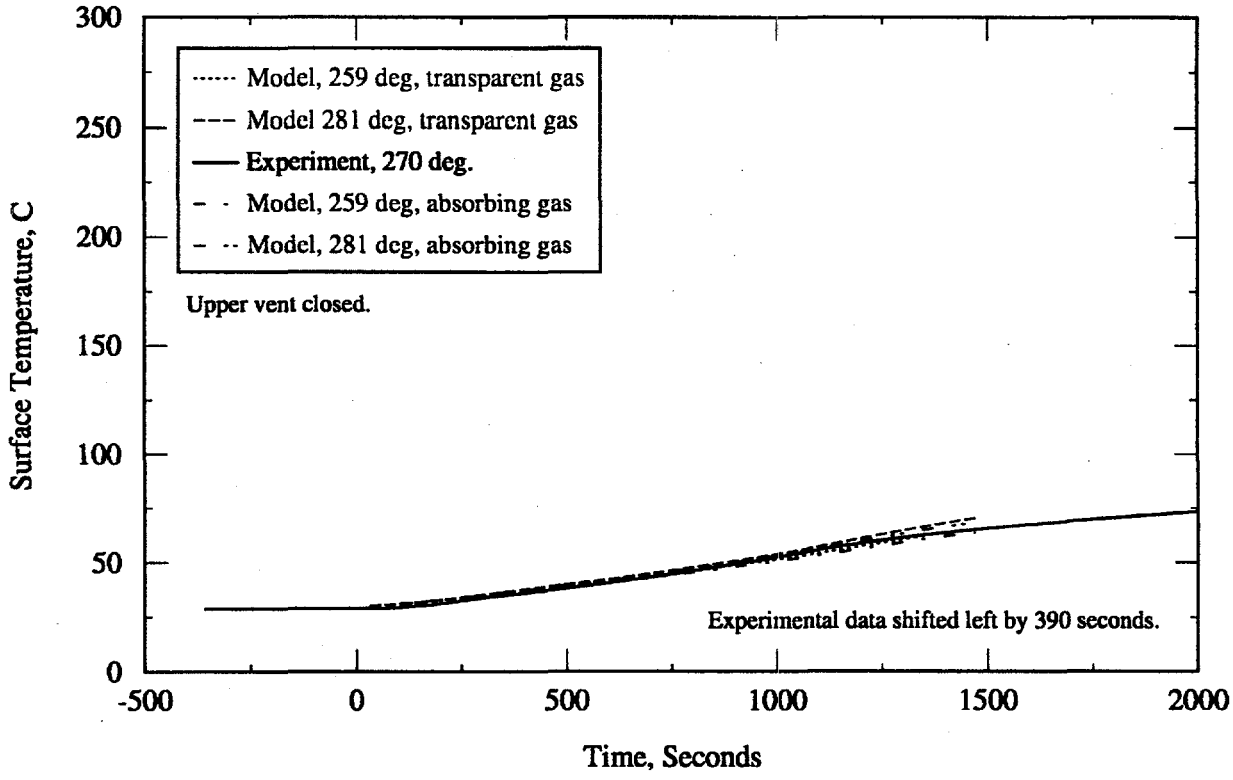

Figure A-6. Calorimeter surface temperatures for model and experiment near 270 degrees.

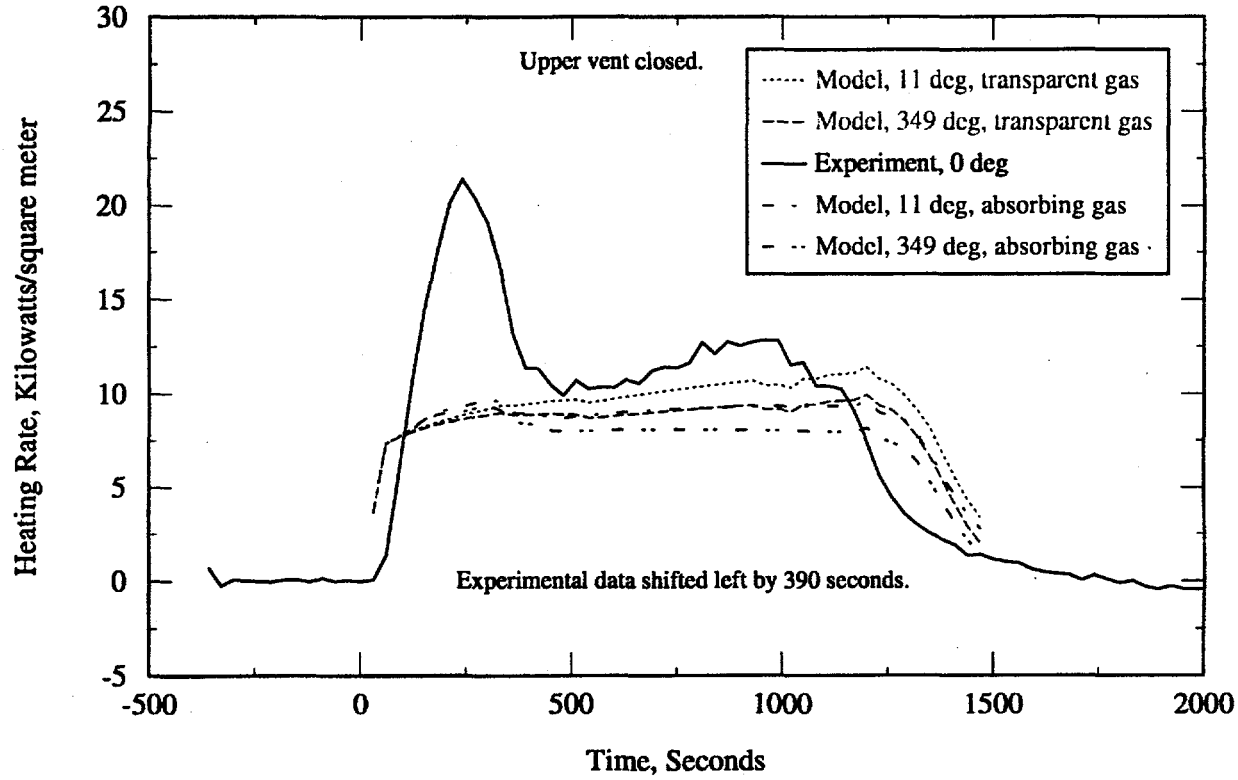

Figure A-7. Calorimeter heat flux for model and experiment near 0 degrees.

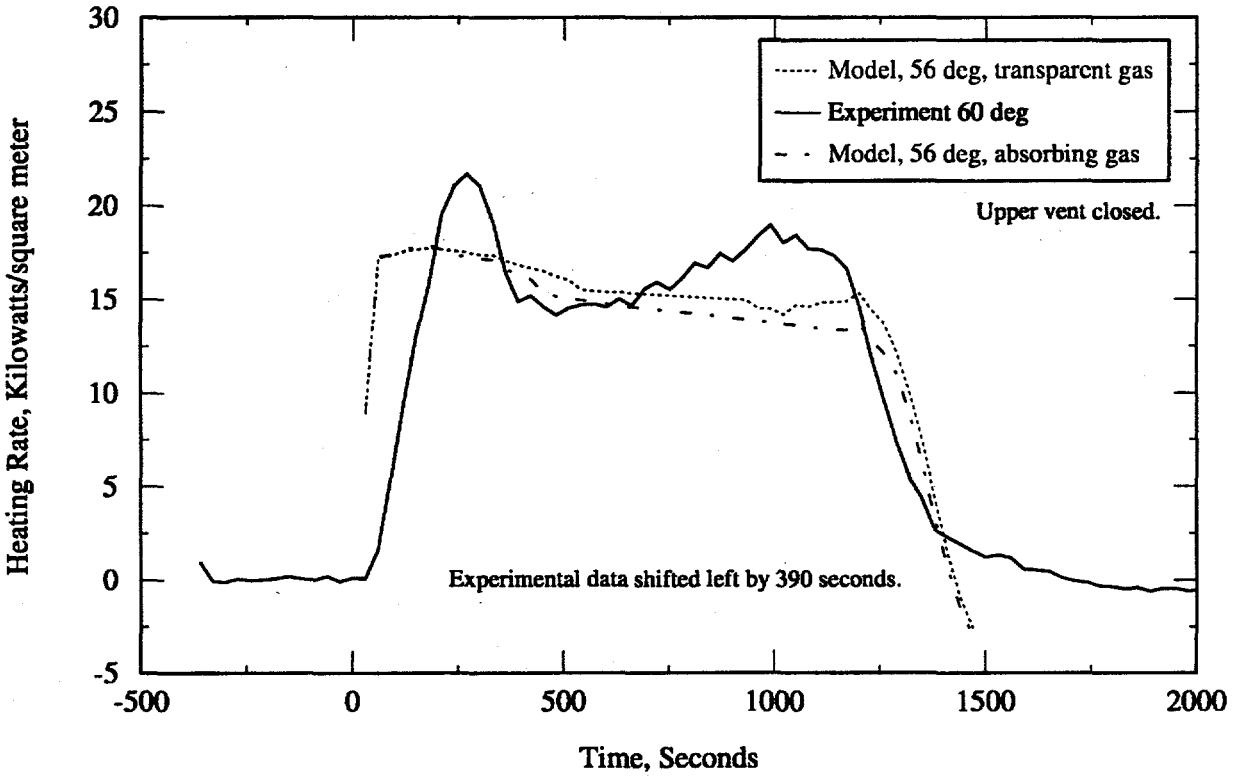

Figure A-8. Calorimeter heat flux for model and experiment near 60 degrees.

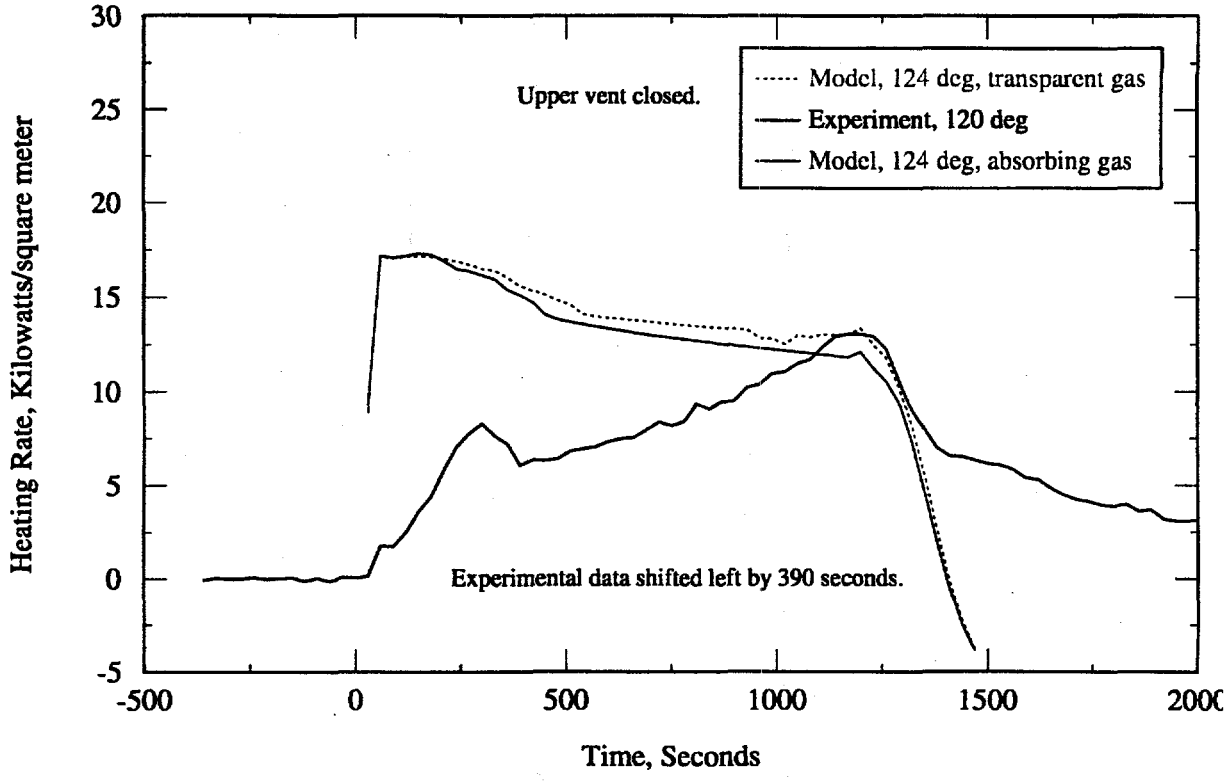

Figure A-9. Calorimeter heat flux for model and experiment near 120 degrees.

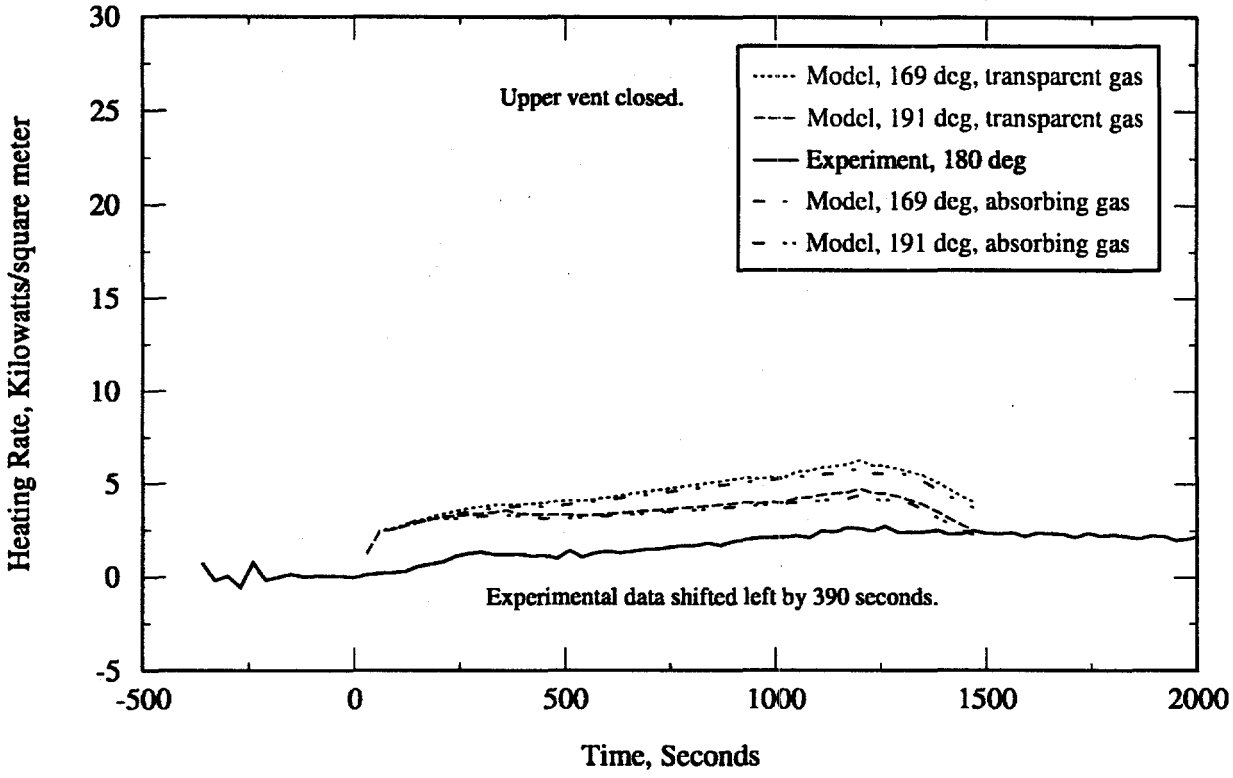

Figure A-10. Calorimeter heat flux for model and experiment near 180 degrees.

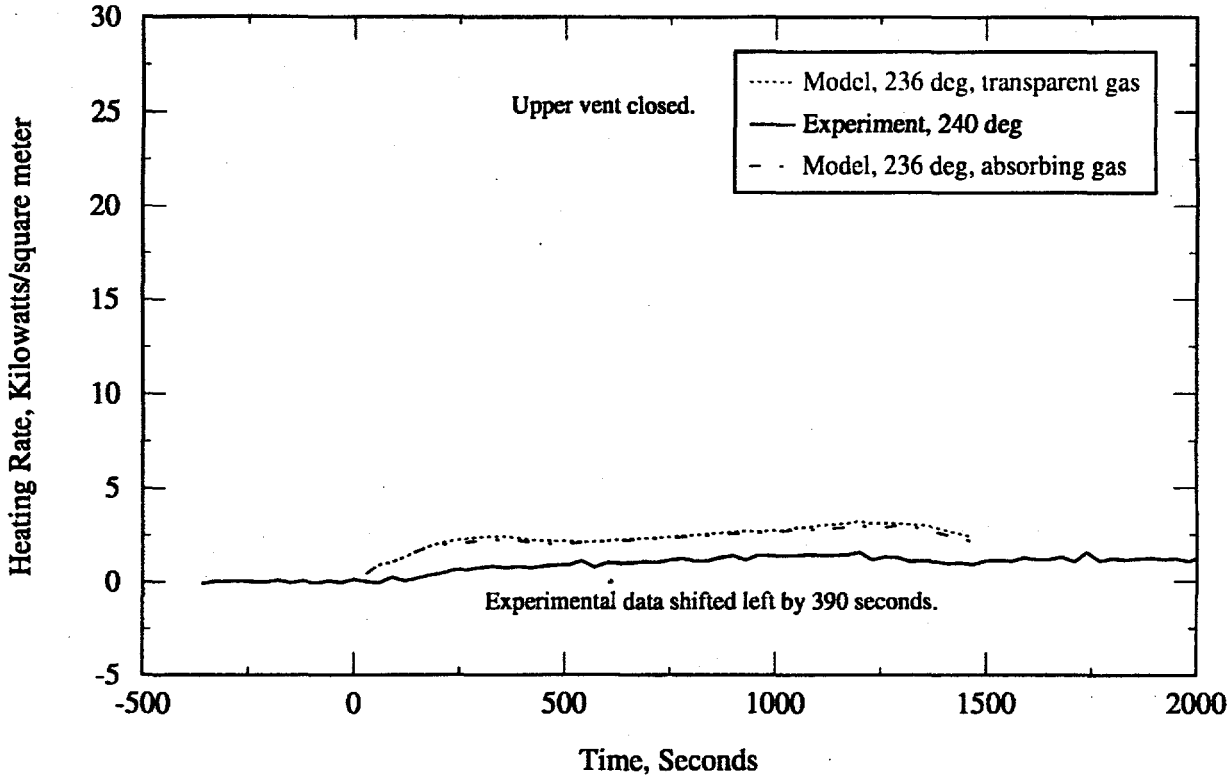

Figure A-11. Calorimeter heat flux for model and experiment near 240 degrees.

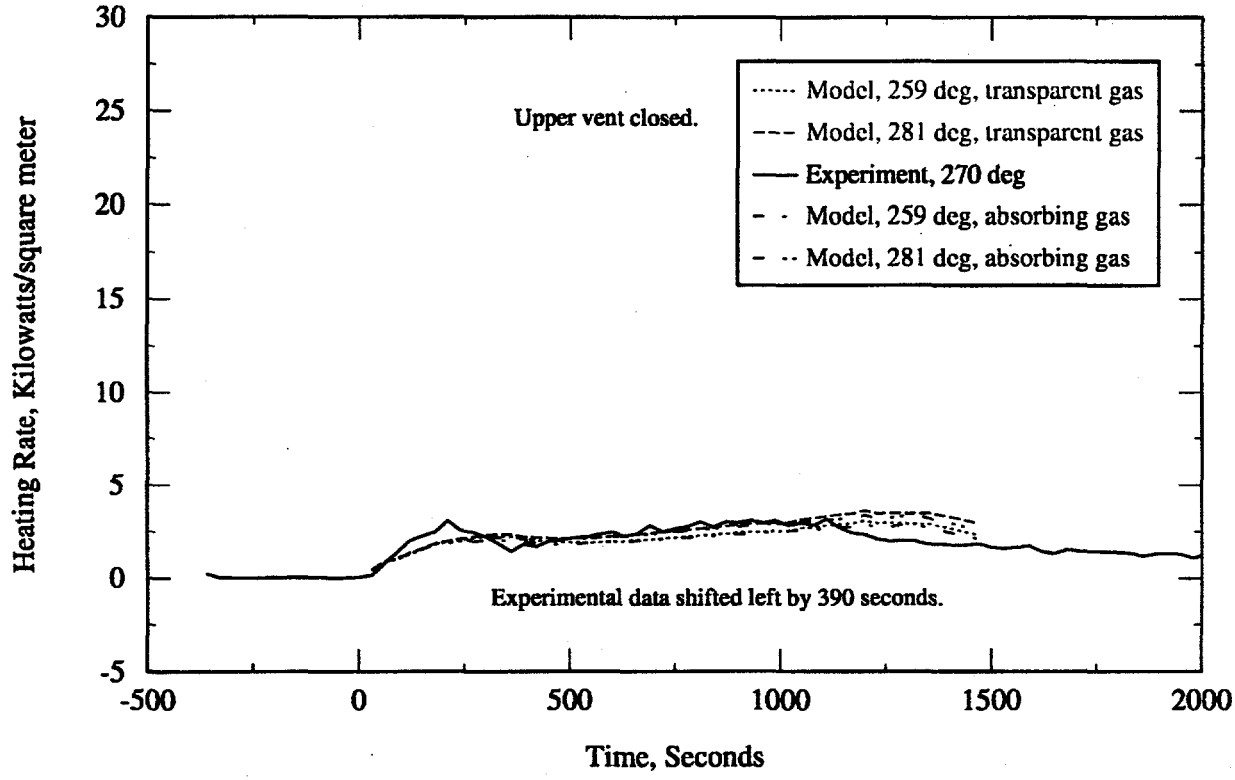

Figure A-12. Calorimeter heat flux for model and experiment near 270 degrees.

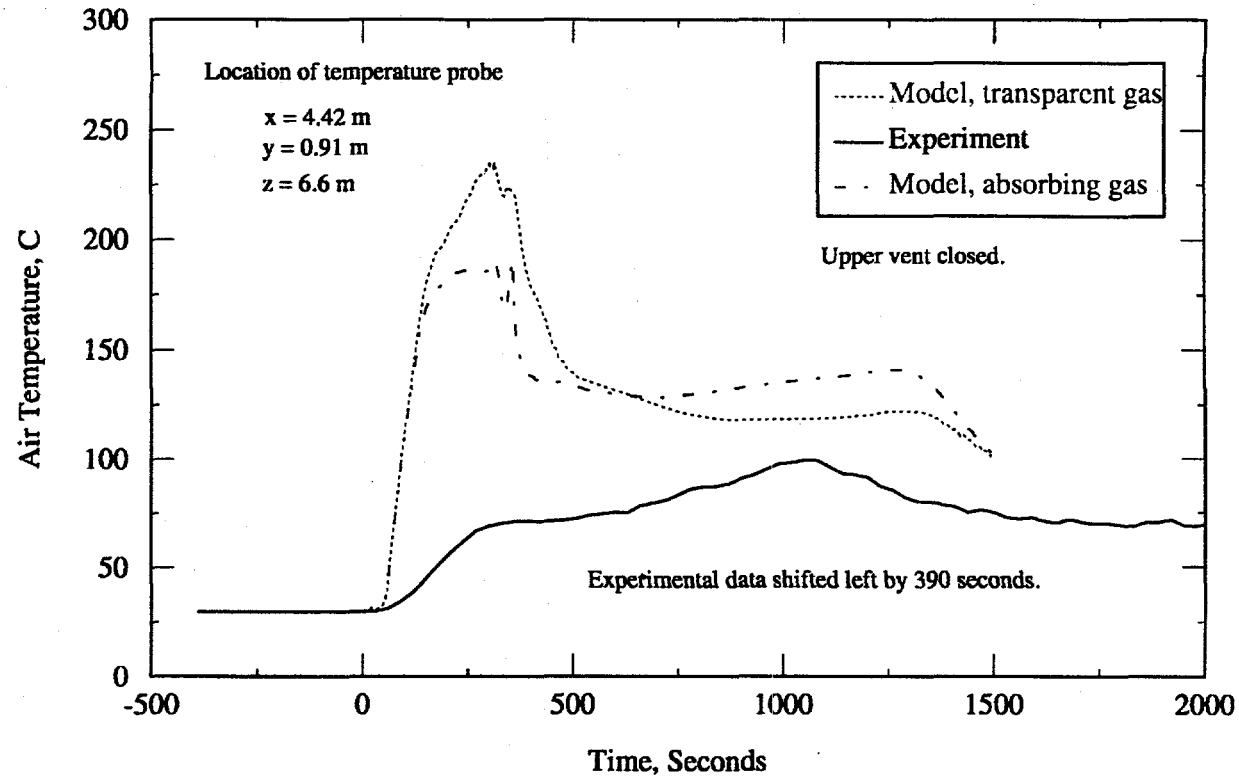

Figure A-13. Model and experiment air temperature 0.91 m above deck of Hold 4.

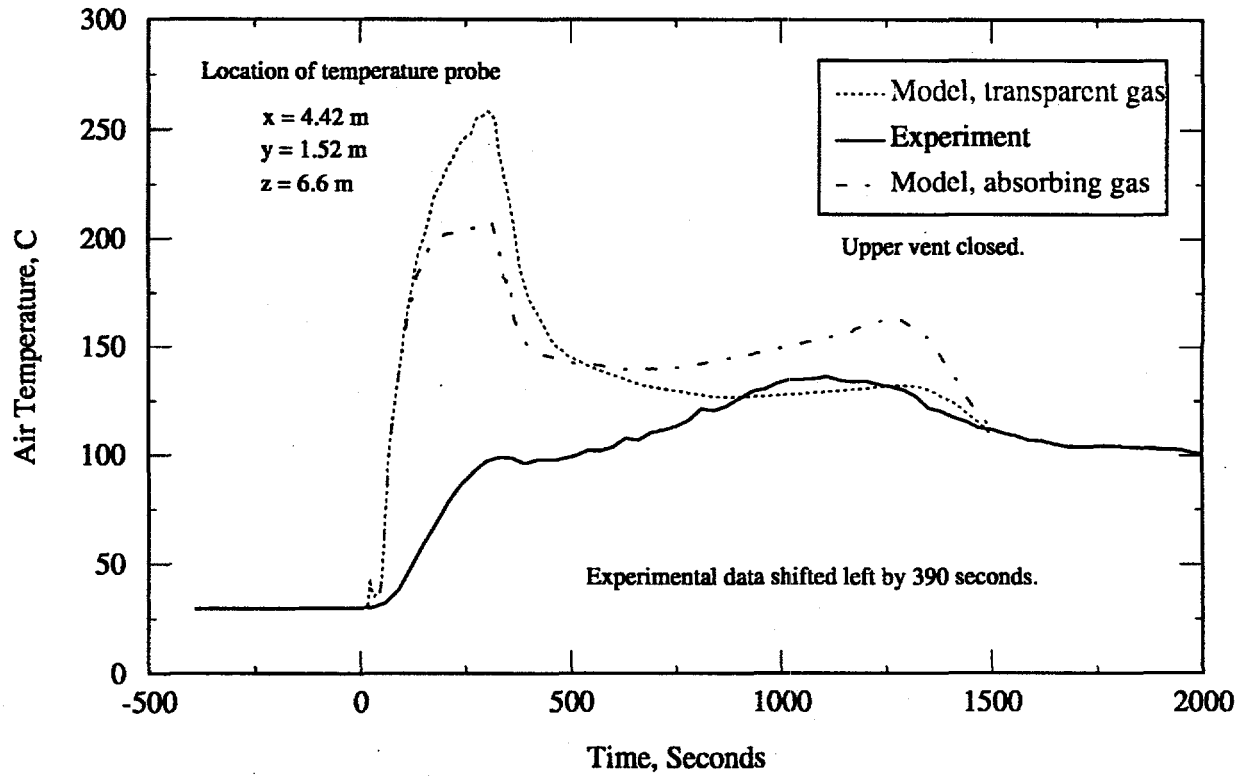

Figure A-14. Model and experiment air temperatures 1.52 m above deck of Hold 4.

Appendix B

Additional Results from Hold 5 Heptane Spray Fire Simulations

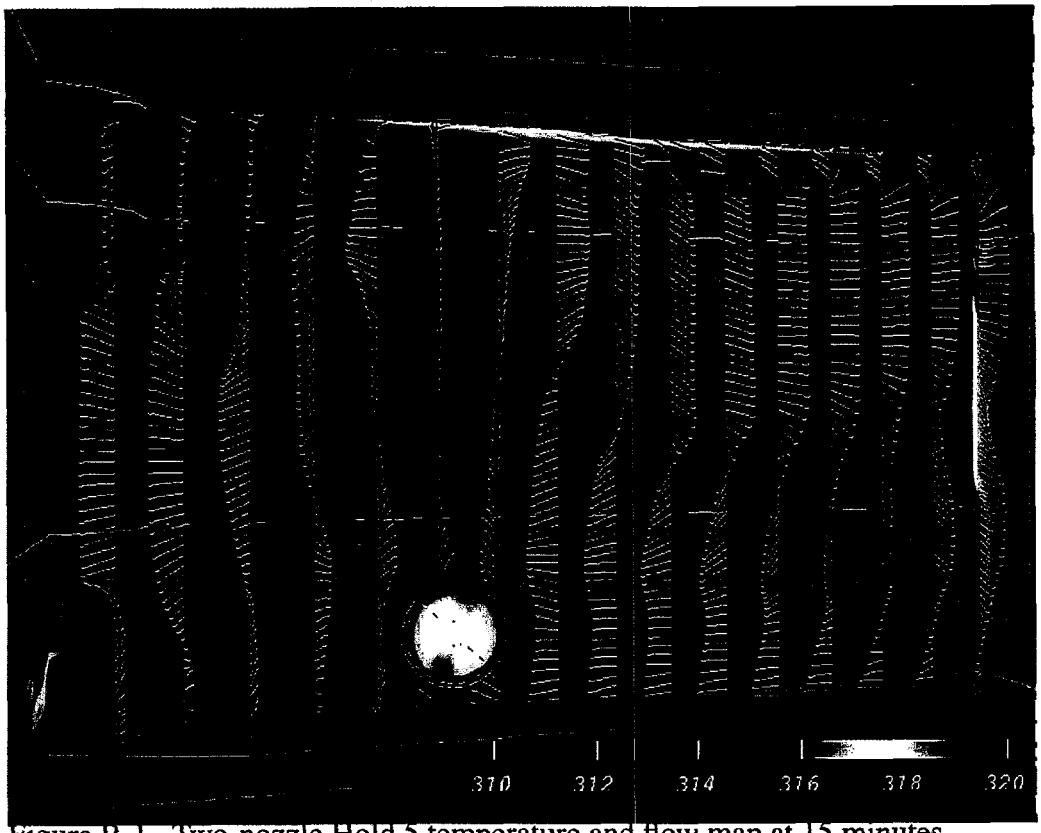

Figure B-1. Two-nozzle Hold 5 temperature and flow map at 15 minutes.

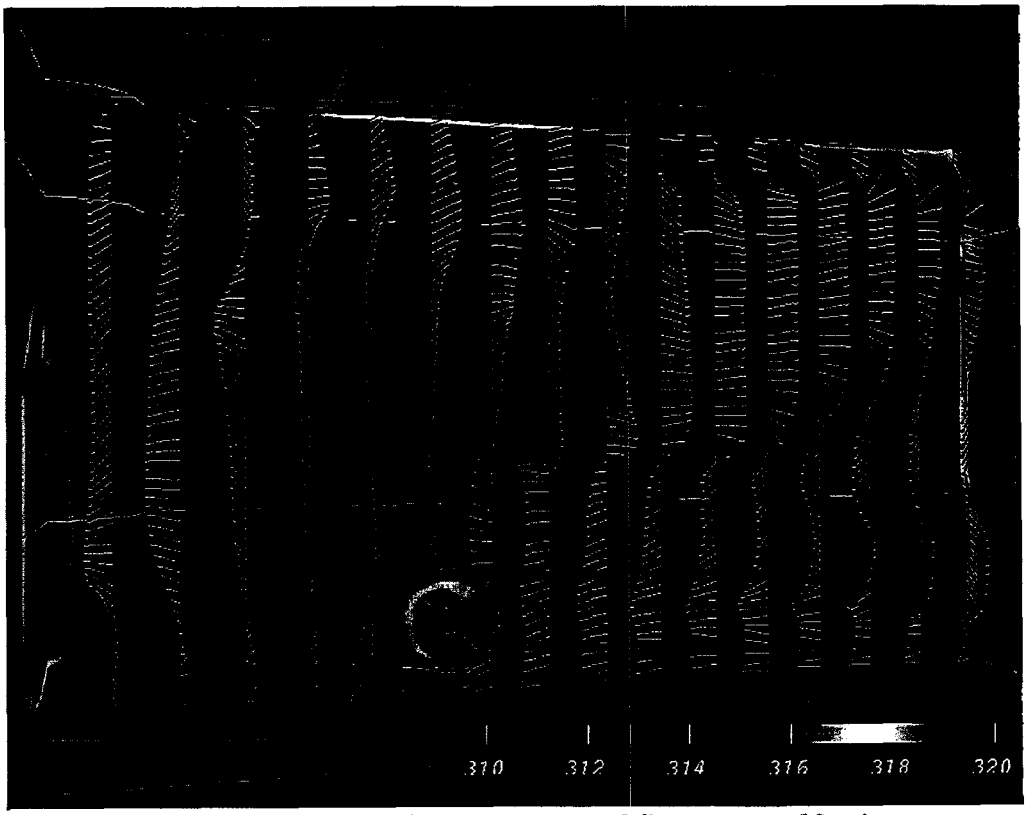

Figure B-2. Two-nozzle Hold 5 temperature and flow map at 30 minutes.

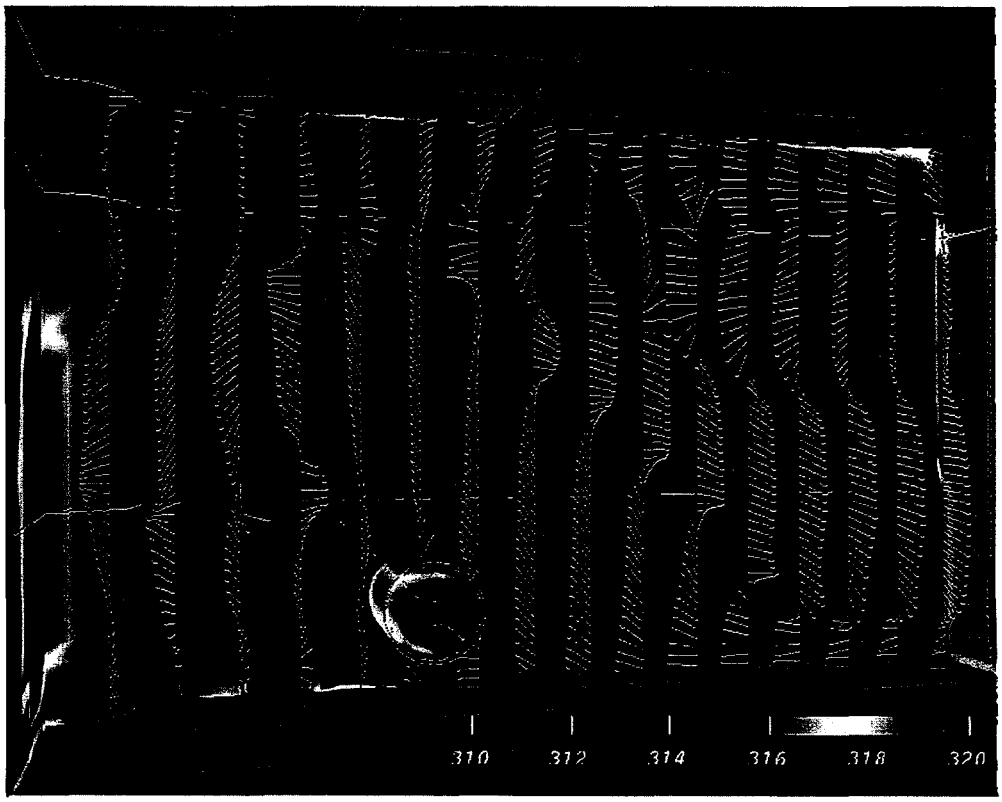

Figure B-3. Two-nozzle Hold 5 temperature and flow map at 45 minutes.

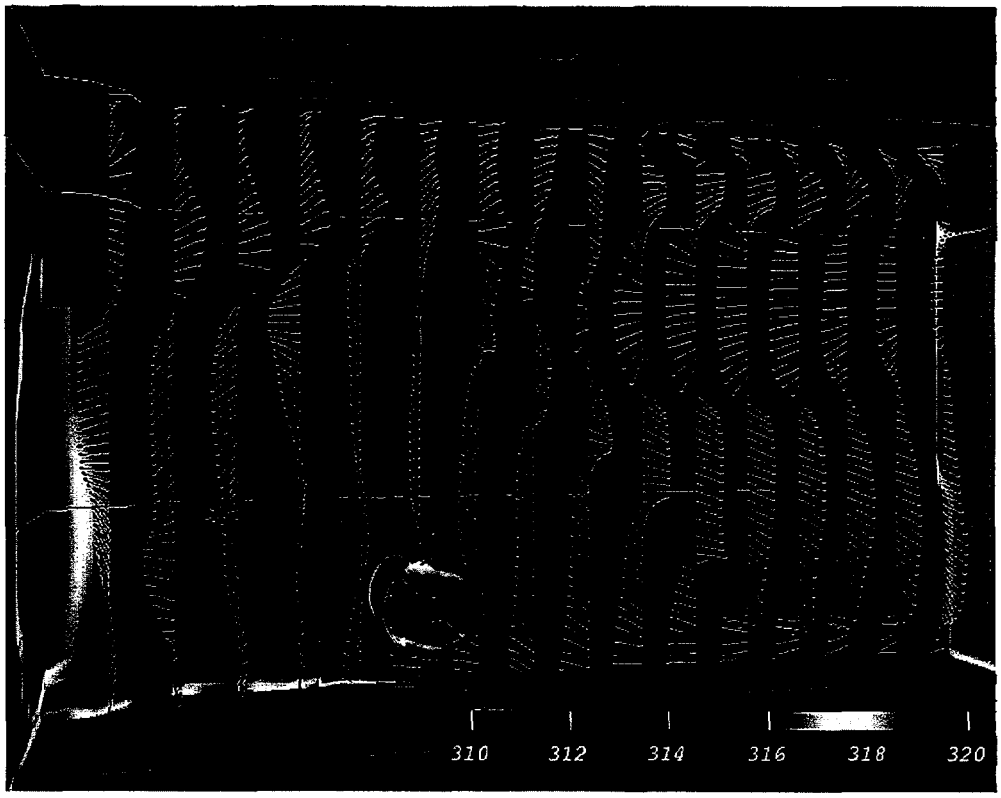

Figure B-4. Two-nozzle Hold 5 temperature and flow map at 60 minutes.

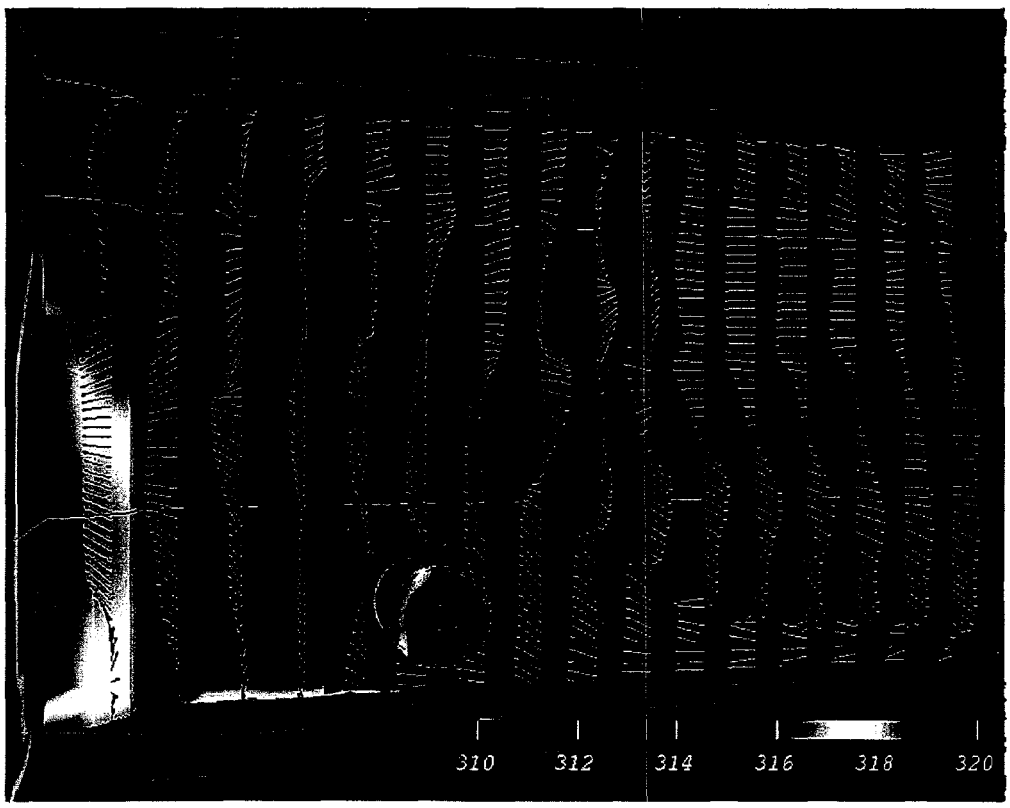

Figure B-5. Two-nozzle Hold 5 temperature and flow map at 75 minutes.

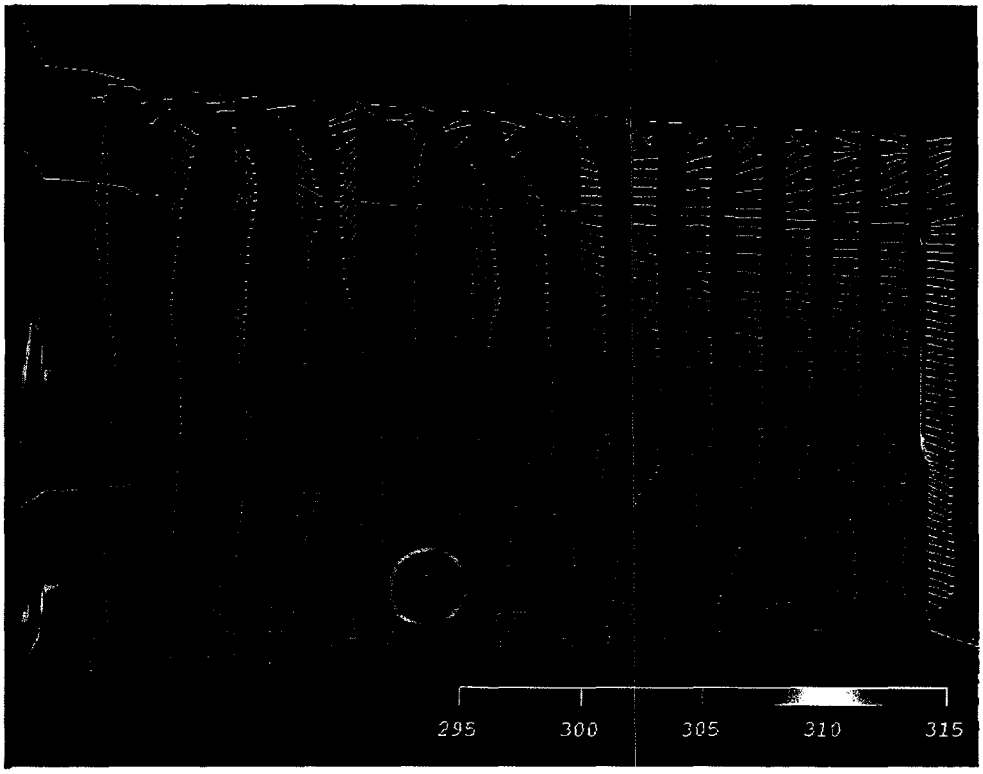

Figure B-6. Four -nozzle Hold 5 temperature and flow map at 15 minutes.

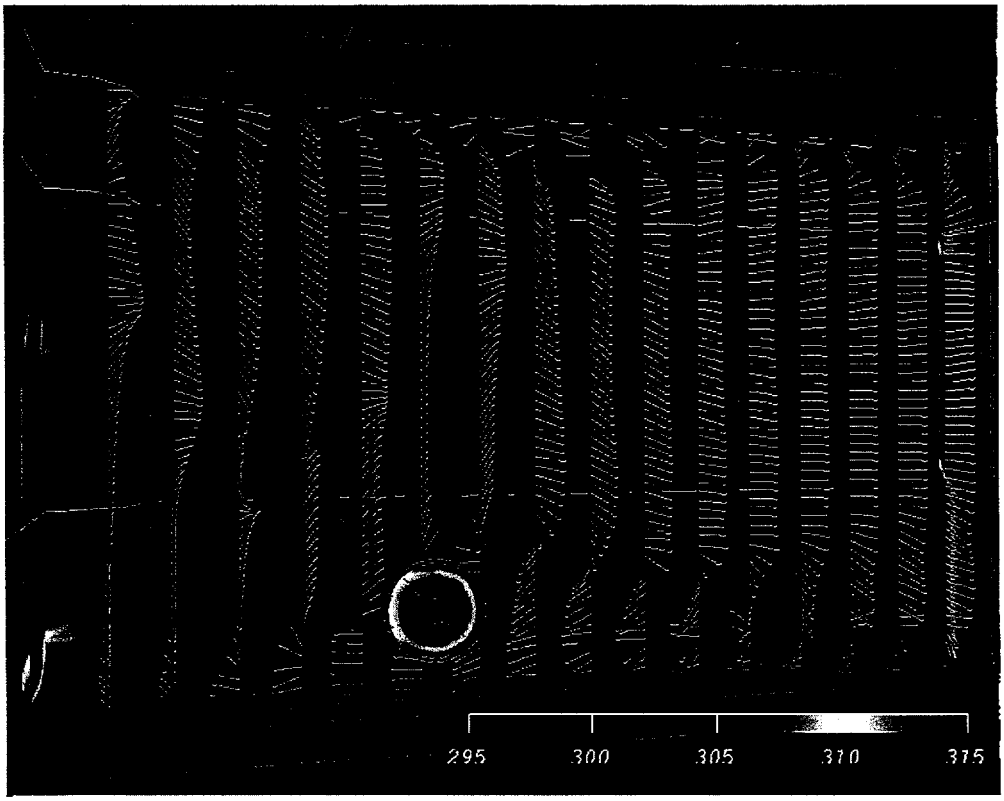

Figure B-7. Four-nozzle Hold 5 temperature and flow map at 30 minutes.

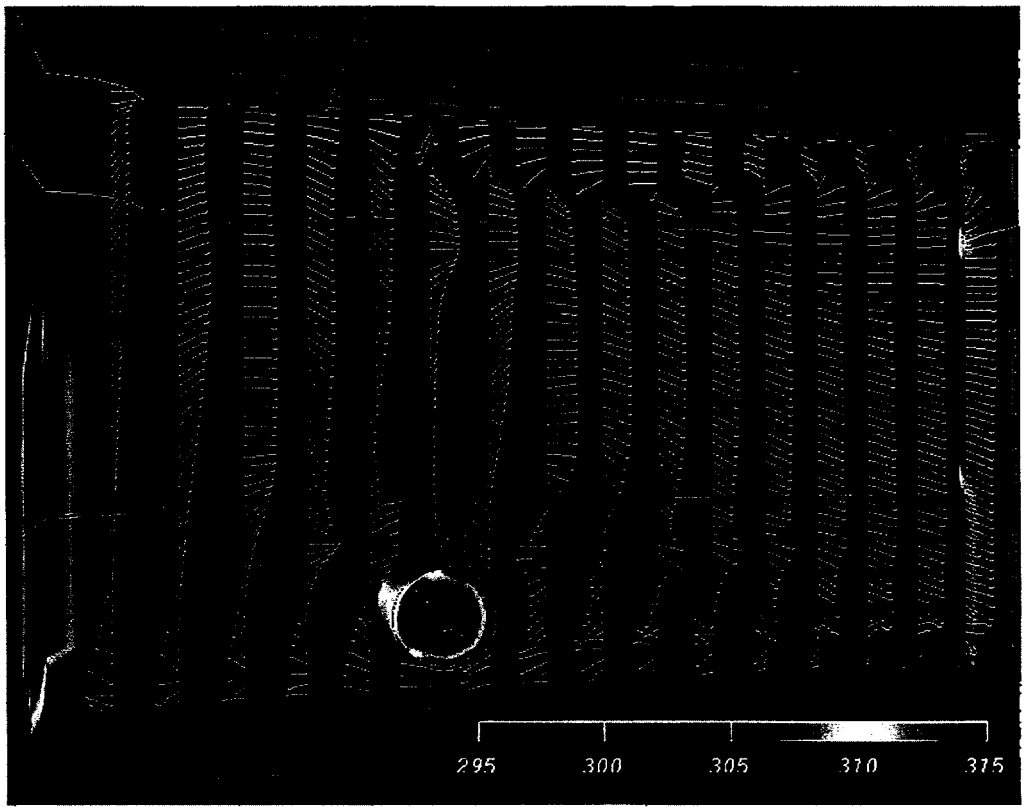

Figure B-8. Four-nozzle Hold 5 temperature and flow map at 45 minutes.

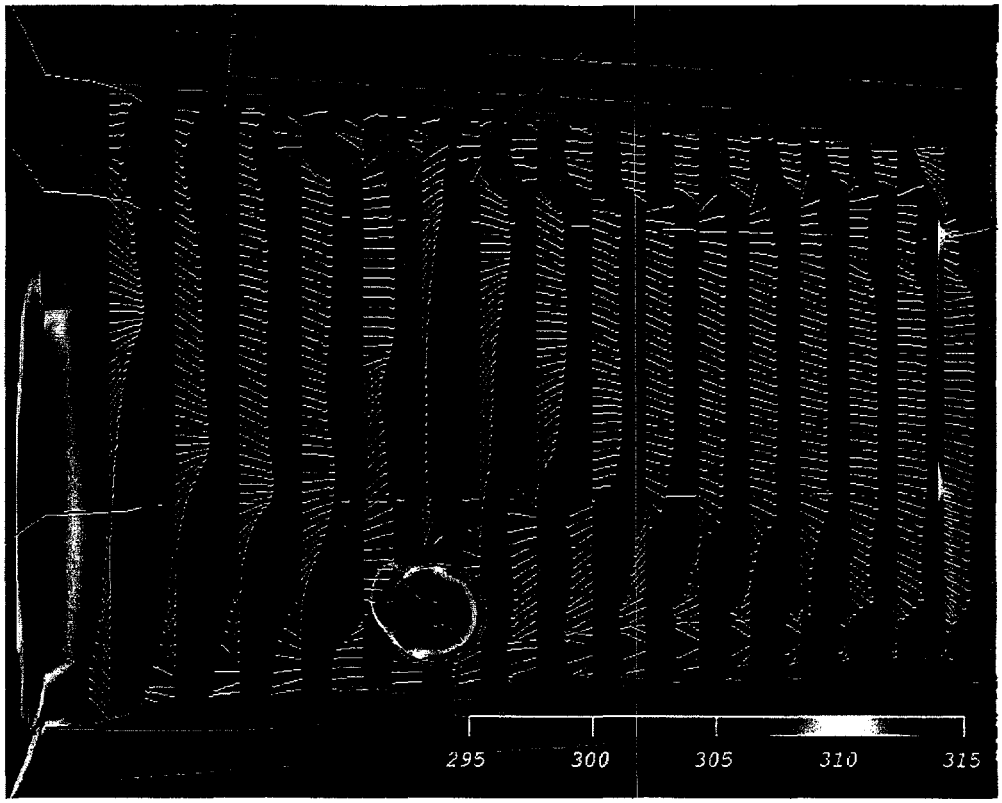

Figure B-9. Four-nozzle Hold 5 temperature and flow map at 60 minutes.

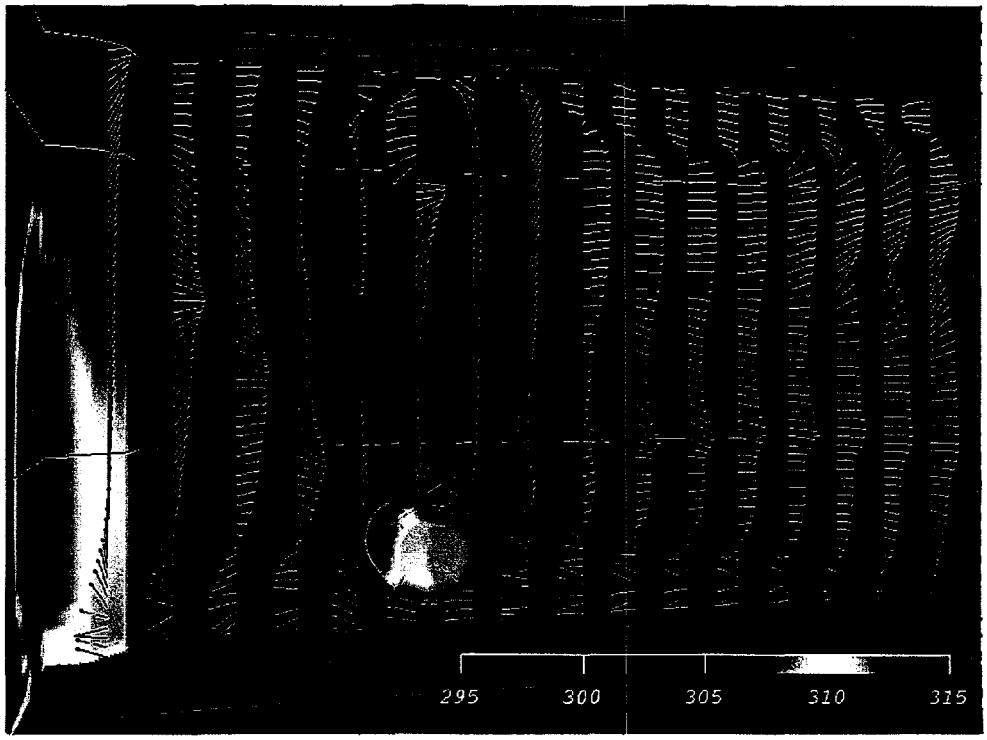

Figure B-10 Four-nozzle Hold 5 temperature and flow map at 75 minutes.

DISTRIBUTION

1 Mr. Ashok Kapoor
U.S. Department of Energy
Office of Transportation, Emergency Management, and Analytical Services
EM-70, Cloverleaf Building
19901 Germantown Road
Germantown, MD 2087-1290

3 U.S. Department of Energy
Office of Transportation, Emergency Management, and Analytical Services
EM-76, Cloverleaf Building
19901 Germantown Road
Germantown, MD 2087-1290

Attn: Mike Keane
Mike Carter
Rich Brancato

2 U.S. Department of Energy
Albuquerque Field Office
Mail Stop 1396
P.O. Box 5400
Albuquerque, NM 87185-1396

Attn: P. Grace
P. Dickman

5 Mr. D. E. Beene, Jr.
U.S.C.G. R & D Center
1082 Shennecossett Road
Groton, CT 06340-6096

1 CWO4 R. W. Byrd
U.S.C.G. Fire & Safety Test Det.
Bldg. S-108 MAIC
Mobile, AL 36615-1384

1 Mr. J. Graupmann
U.S.C.G. Fire & Safety Test Det.
Bldg. S-108 MAIC
Mobile, AL 36615-1384

1 Mr. E. Pfersich
Commandant G-MSO-3
2100 2nd Street SW
Washington, DC 20593

1 Mr. William Lake
U.S. Department of Energy
RW-431
Forrestal Building
1000 Independence Avenue SW
Washington, DC 20585

1 Mr. F. Armingaud
60-68 Av. du General Leclerc
B. P. No. 6
F-92265 Fontenay-aux-Roses, Cedex
France

1 Mr. B. Desnoyers
COGEMA
Service des Transports
B. P. No. 4
F-78141 Velizy Villacoublay Cedex
France

1 Richard Rawl
Wagramerstasse 5
P.O. 100
A-1400 Vienna, Austria

1 Mr. T. Schneider
Route du Panorama
F-92263 Fontenay-aux-Roses Cedex
France

1 Mr. F. Lange
Gesellshaft fur Anlagen- und Reatorsicherheit GmbH
Schwertnerstrass 1
D-506667 Cologne
Germany

1 Mr. K. Shibata
Nucear Material Control Division
San-Kai Doh Bldg.
9-13, 1-chome, Akasaka
Minato-ku
Tokyo
Japan

1 Ms. A-M. Ericsson
AMC Konsult AB
Kammakargatan 6
S-111 40 Stockholm
Sweden

1 Mr. R. Cheshire
Transport Division
British Nuclear Fuels plc
Fleming House
Risley, Warrington
Cheshire, WA3 6AS
United Kingdom

1 Mr. M. Hussain
British Nuclear Transport Limited
Risley, Warrington
Cheshire WA3 6AS
United Kingdom

1 Mr. Clive Young
Department of Transport
Room P2/023E
2 Marsham Street
London SW1P 3EB
United Kingdom

1 Ron Pope
MS 6495
Oak Ridge National Laboratory
P.O. Box 2008
Oak Ridge, TN 37831-6495

1 Mr. N. Watabe
Nuclear Fuel Cycle Department
Central Reseach Institute of Electric
Power Industry
1646 Abiko-shi, Chiba-ken 270-11
Japan

1 Mr. Rod Fisk
Edlow International Co.
1666 Connecticut Ave. Suite 500
Washington, DC 20009

1 Mr. Robert Heid
ECO
1356 Cape St. Claire Rd.
Annapolis, MD 21401-5216

1	MS 0715	R. E. Luna, 6610
10	MS 0715	TTC Library, 6610
1	MS 0716	C. Olson, 6643
1	MS 0716	P. E. McConnell, 6643
1	MS 0717	G. F. Hohnstreiter, 6642
1	MS 0717	D. G. Ammerman, 6642
10	MS 0717	J. A. Koski, 6642
1	MS 0717	M. Arviso, 6642
1	MS 0717	J. G. Bobbe, 6642
1	MS 0718	J. L. Sprung, 6641
1	MS 0717	J. D. Pierce, 6642
1	MS 0717	J. K. Rader, 6642
1	MS 0718	H. R. Yoshimura, 6641
1	MS 0525	S. D. Wix, 1252
1	MS 0724	J. B. Woodard, 6000
1	MS 0726	J. K. Rice, 6600
5	MS 0899	Technical Library, 4916
1	MS 9018	Central Tech Files, 8940
2	MS 0619	Review & Approval Desk, 12690 for DOE/OSTI